EXPERIMENTAL INVESTIGATION OF BULK FLAME QUENCHING IN A DIRECT-INJECTION SPARK IGNITION ENGINE

by

TYSON E. STRAND

A thesis submitted in partial fulfillment of
the requirements for a degree of

MASTER OF SCIENCE
(MECHANICAL ENGINEERING)

at the

UNIVERSITY OF WISCONSIN – MADISON

2001

Abstract

The following thesis describes planar laser-induced fluorescence (PLIF) experiments that investigate bulk flame quenching in the lean periphery of a stratified fuel cloud during light-load operation of a direct-injection spark-ignition (DISI) engine. PLIF of both 3-pentanone doped into the fuel (iso-octane) and OH present naturally in the combustion products were imaged on an intensified CCD camera. The OH images show the progression of the flame front and the expansion of the product zone. The 3-pentanone images provide visualization of the progression of the flame front through the consumption of fuel, as well as allowing quantification of the local equivalence ratio in the stratified, unburned mixture.

Under stratified operating conditions, using an overall equivalence ratio of Φ = 0.3 and an engine speed of 600 rpm, quenching of the flame in the lean periphery of the fuel cloud was observed. The combustion product zone (OH fluorescence) showed a period of rapid growth shortly after ignition. The flame front propagation stopped before the edge of the piston bowl, and the product zone ceased expansion. Images of the fuel region (3-pentanone fluorescence) demonstrate the consumption of the fuel, the propagation and stalling of the flame front, and a region of unburned fuel present long after the end of heat release (as late as 70° ATDC). Advancing the combustion phasing by varying the injection and ignition timings within a window of acceptable combustion characteristics was not sufficient to alleviate quenching. However, quenching was alleviated when the air intake pressure was reduced to 69 kPa while the mass of injected

fuel was held constant. The cause for this behavior is believed to be a combination of increased homogeneity of the fuel cloud and higher end gas temperatures, which decreases the lean flammability limit of the fuel.

For my wife, Anna,

whose love and support

have endured

For our daughters,

Madeline and Adrienne

For my mother

For my father

Acknowledgments

I would first like to acknowledge the support of Jaal Ghandhi, whose motivation, encouragement, insight, and broad range of knowledge have made this project a pleasure to endure.

The support of the Department of Energy, through Sandia National Laboratories, is gratefully acknowledged.

Table of Contents

Abstract . . . . . **i**

Acknowledgments. . . . . . **ii**

List of Figures . . . . . **ix**

List of Tables . . . . . **xvi**

1 Introduction **1**

1.1 Introduction **1**

1.2 Goals and objectives **2**

1.3 Outline and overview **3**

2 Literature Review **5**

2.1 DISI engines **5**

2.1.1 Motivation for DISI research 5

2.1.2 DISI fundamentals 5

2.1.3 Historical development of the DISI engine 7

2.1.4 Problems with stratified combustion 9

2.1.5 Hydrocarbon emissions:
Piston wetting -vs- Bulk flame quenching 11

2.1.6 Bulk flame quenching of the flame at the lean periphery 14

2.2 Planar laser-induced fluorescence 15

2.2.1 LIF of OH 16

2.2.2 LIF of 3-pentanone 17

2.2.3 Planar laser-induced fluorescence in DISI engines 18

3 Experimental setup 20

3.1 Optically accessible engine 21

3.2 Laser system and optical assembly 24

3.3 Imaging system 27

3.4 Image correction procedure 29

4 Flame structure visualization 35

4.1 Introduction 35

4.2 Conditions 35

4.3 Flame structure visualization 37

4.3.1 High load flame structure 37

4.3.2 Light load pre-combustion mixture distribution 41

4.3.3 Light load flame structure 44

4.4 Discussion 46

4.5 Conclusions 57

5 Bulk quenching of the flame 59

5.1 Introduction 59

5.2 Conditions 59

5.3 Bulk quenching 62

5.3.1 Bulk flame quenching – existence 62

5.3.2 Bulk flame quenching – effect of combustion phasing 69

5.3.3 Bulk flame quenching – effect of intake throttling 71

5.4 Discussion 78

5.5 Conclusions 80

6 Conclusions 83

Appendix A Fractal concepts 86

A.1 Introduction 86

A.2 Background 86

A.2.1 Fractal fundamentals 86

A.2.2 Literature review 92

A.3 Fractal analysis 94

A.3.1 Validation of the method of calculating D 94

A.3.2 Flame structure analysis 103

A.4 Conclusions 106

References 107

List of Figures

Chapter 1

Chapter 2

Chapter 3

Figure 3.1 . . . . Layout of the experimental setup, showing the relationship between the three primary components and the path of the laser. 23

Figure 3.2 . . . . (a) Layout of the single cylinder DISI engine used in the study, showing the general layout and optical access. (b) Orientation of the injector, piston bowl, spark plug, and intake and exhaust valves. 24

Figure 3.3 . . . . Orientation of the laser sheet relative to the cylinder liner, piston cup, spark plug, and injector. The counter-clockwise swirl direction is illustrated by the arrow. 28

Figure 3.4 . . . . Illustration of the image correction process: Top row, 3-pentanone correction: raw image (left) followed by the background and flatfield corrected

image, bottom row, OH correction: raw image (left) followed by the filtered image.. 34

Chapter 4

Figure 4.1 . . . . Engine map test results illustrating the IMEP and COV as functions of injection timing and spark timing for 600 rpm and 1200 rpm at an equivalence ratio of ϕ=0.3. The locations of the cases in Table 1 are represented by the circle: the Baseline (B), Advanced (A), Advanced Injection (AI), and Retarded (R) cases. 38

Figure 4.2 . . . . Representative single-shot PLIF images for Φ=0.7 operating at 600 rpm and 1200 rpm. θ_1 = 25°, θ_2 = 35°. All images were taken on different engine cycles, within five CA degrees of the reported angle. 39

Figure 4.3 . . . . Representative 3-pentanone fluorescence images taken at spark time for the cases listed in Table 1.. 42

Figure 4.4 . . . . Contour plots of equivalence ratios for ϕ=0.3 (a) 600 rpm (top) and (b) 1200 rpm (bottom). 43

Figure 4.5 . . . . Representative single-shot PLIF images for stratified combustion at engine speeds of 600 rpm and 1200 rpm at Φ=0.3. Pictures were taken at 18° after ignition for the top row, 25° after ignition for the second row, and 35° after ignition for the bottom row. All images were taken on different engine cycles. 45

Figure 4.6 . . . . 3-pentanone intensity profile for premixed injection (Φ=0.7), 15 degrees after spark, operating at 1200 rpm.. 47

Figure 4.7 . . . . 3-pentanone intensity profile for direct injection (Φ=0.7), EOI at 180° BTDC, 15 degrees after spark, operating at 1200 rpm.. 48

Figure 4.8 . . . . OH intensity profile for sratified combustion (Φ=0.3), 20 degrees after spark, operating at 1200 rpm.. 48

Figure 4.9 . . . . 3-pentanone intensity profile for stratified combustion (Φ=0.3) of the baseline case in Table 1, image taken 20 degrees after spark, operating at 600 rpm.. 48

Figure 4.10 . . . . Location of the test boxes for the statistical analysis of the fuel distribution. 50

Figure 4.11 . . . . Histograms of box averages. Solid line = downstream box, dashed line = upstream box, for 600 rpm (13a) and 1200 rpm (13b).. 53

Figure 4.12 . . . . Histograms of box standard deviations. Solid line = downstream box, dashed line = upstream box, for 600 rpm (14a) and 1200 rpm (14b).. 54

Figure 4.13 . . . . Comparison of crank angle delay between ignition and 0.7 bar cylinder pressure against the average equivalence ratio within the box for Φ=0.7, EOI at 180° BTDC. The inset in the Right Box plot indicates the region where the premixed combustion occurred. 56

Chapter 5

Figure 5.1 . . . . Images of flame luminosity at various crank angles. 3-pentanone fluorescence shown in solid circles, flame luminosity is uncircled. At left, Images obtained with laser operating, showing both 3-pentanone fluorescence and

flame luminosity, at right, images obtained without the laser operating, showing only flame luminosity. 61

Figure 5.2 . . . . Left, mean experimental pressure trace of the baseline operating condition EOI at 48° BTDC and ignition at 15° BTDC. Right, log(P) vs log(v) plot of the same pressure data. 62

Figure 5.3 . . . . 3-pentanone images at various crank angles for P_{in} = 14.3 psi, operating at 600 rpm and Φ=0.3, EOI at 48° BTDC, ignition at 15° BTDC. (a) Picure at 5° ATDC, (b) Picure at 10° ATDC, , (c) Picure at 40° ATDC, (d) Picure at 60° ATDC. 64

Figure 5.4 . . . . OH images at various crank angles for P_{in} = 14.3 psi, operating at 600 rpm and Φ=0.3, EOI at 48° BTDC, ignition at 15° BTDC. (a) Picure at 5° BTDC, (b) Picure at 5° ATDC, (c) Picure at 10° ATDC, (d) Picure at 15° ATDC. 65

Figure 5.5 . . . . 3-pentanone fluorescence showing the unburned fuel region after the quenching event. The image was taken at 40° ATDC. The solid white circle shows the outline of the piston bowl. The signal in the dashed white circle is flame luminosity that was not removed in the correction process. The arrow indicates the location of the intensity profile shown at left. The equivalence ratio of the unburned periphery is between 0.2 and 0.4. 67

Figure 5.6 . . . . Log(P)-log(V) plots and the associated images showing the unburned fuel. The picture timing (40° ATDC) is shown by the line across the expansion stroke. Clearly all heat release has ended by this time. 68

Figure 5.7 . . . . Effect of varying injection conditions on lean quenching operating at 600 rpm and Φ=0.3. All images were taken at 25° ATDC. (a) end of injection (EOI) at 60° BTDC, ignition at 20° BTDC, (b) EOI at 48° BTDC, ignition at 15° BTDC, (c) EOI at 48° BTDC, ignition at 20° BTDC, (d) EOI at 48° BTDC, ignition at 25° BTDC.. 72

Figure 5.8 . . . . Effect of varying intake pressure, P_{in}, on lean quenching, operating at 600 rpm and Φ=0.3, EOI at 48° BTDC, ignition at 15° BTDC. All images were taken at 10° ATDC. (a) P_{in}=10 psi, (b) P_{in}=12 psi, (c) P_{in}=14.3 psi, (d) P_{in}=16 psi.. 73

Figure 5.9 . . . . 3-pentanone images at various crank angles for P_{in} = 10 psi, operating at 600 rpm and Φ=0.3, EOI at 48° BTDC, ignition at 15° BTDC. (a) Picure at 5° BTDC, (b) Picure at 5° ATDC, , (c) Picure at 10° ATDC, (d) Picure at 25° ATDC.. 76

Figure 5.10 . . . . OH images at various crank angles for P_{in} = 10 psi, operating at 600 rpm and Φ=0.3, EOI at 48° BTDC, ignition at 15° BTDC. (a) Picure at 5° BTDC, (b) Picure at top dead center, (c) Picure at 7° ATDC, (d) Picure at 20° ATDC.. 77

Figure 5.11 . . . . Temperature history calculated assuming isentropic compression using the experimentally obtained pressure trace for intake pressures of 99 kPa (dashed) and 69 kPa (solid). 80

Chapter 6

Appendix A

Figure A.1 . . . . Map of the northern coast of Norway. Notice the roughness of the coastline, making an estimate of its length difficult. 89

Figure A.2 . . . . Graph of $H^s(A)$ vs s. The location at which $H^s(A)$ jumps from infinity to zero is at s = D_H.. 90

Figure A.3 . . . . From Mantzaras, 1989 [58]. Images of engine flames taken at Φ = 1.0, engine speed increases from the top to the bottom of the figure.. 93

Figure A.4 . . . . From Gulder, 2000 [59]. Images of turbulent jet flames, the turbulence intensity increases from left to right.. 93

Figure A.5 . . . . The results of Gulder et al. showing the calculated fractal dimension of objects of known properties using the circle method and the caliper (yardstick) method. The predicted fractal dimension of the slope of the log(length) vs log(scale) plot is $m = 1 - D_s$. (top) the Quadric Koch Curve with D_s = 1.5, (bottom) variant of the QKC with D_s = ... 95

Figure A.6 . . . . (a) 8-segment Quadric Koch Curve, which has known fractal dimension $D_s = D_H = 1.5$. (b) Results for the calculated fractal dimension Ds using the box method. The upper line is the exact solution with a slope of 1.5, the lower line is a best fit to the data. 101

Figure A.7 . . . . (a) Variation of the Quadric Koch Curve having known fractal dimension $D_s = D_H = 1.465$. (b) Results of the calculation of the fractal dimension Ds using various window sizes on the flame front. An increased widow size increases the number of start points on each image, and therefore results in a larger averaging population. 102

Figure A.8 . . . . Demonstration of the OH image processing for the calculation of the fractal dimension. (a) The raw data image, (b) the scaled image, and (c) the outline of the flame front. 103

Figure A.9 . . . . Calculation of the (similarity) fractal dimension Ds for a premixed engine flame operating at 600 rpm. The result of the log-log plot shows a value of Ds = 1.25. 105

Figure A.10 . . . . Calculation of the (similarity) fractal dimension Ds for a premixed engine flame operating at 1200 rpm. The result of the log-log plot shows a value of Ds = 1.27. 105

List of Tables

Chapter 1

Chapter 2

Chapter 3

Table 3.1 . . . . Description of the optical components of Figure 3.1.. 22

Table 3.2 . . . . Engine data for the DISI engine used in this study.. 22

Chapter 4

Table 4.1 . . . . Stratified running conditions examined for Φ=0.3: End of injection (EOI) and ignition (ign) timing in crank angle degrees BTDC.. 37

Chapter 5

Chapter 6

Appendix A

1 Introduction

1.1 Introduction

The concept of direct injection of the fuel in a spark-ignition (DISI) engine has received continued interest for several decades because of the potential benefits it offers. These benefits include the reduction of pumping losses and increased thermal efficiency due to an increased compression ratio and the overall lean operation of the engine. The combination of these benefits results in a significantly improved fuel economy when compared with current port fuel injected (PFI) engines.

The primary technical difficulty that has inhibited the wide-scale implementation of DISI engines is the high level of pollutant emissions. Of particular concern are the emissions of unburned hydrocarbons and NOx under lean, stratified operating conditions. It is the former that is addressed in this study. Several possible mechanisms contribute to the emission of unburned hydrocarbons. Bulk quenching of the flame in the lean periphery of the stratified fuel cloud is often cited as a possible contributor. Although several experimental and computational studies suggest that quenching occurs and is a relevant mechanism, no direct observation of the quenching event or measurement of its effect on the presence of post-combustion hydrocarbons has been presented in the literature.

Combustion control in a DISI engine is achieved through the timing and duration of the fuel spray and its subsequent interaction with the in-cylinder flowfield and geometry. The goal of the control scheme is to have a combustible mixture at the spark

plug when the spark occurs. For high loads, operation similar to a premixed-charge engine is achieved by injecting the fuel early to allow thorough mixing and, therefore, a nearly homogeneous charge throughout the cylinder at the time of ignition. To achieve unthrottled operation at light loads, the DISI engine operates using stratified combustion. Under this mode of operation, the cylinder contents are overall lean, but the stratified fuel cloud near the spark location at ignition time is ideally slightly rich to aid ignition. It is operation in this stratified mode that is both the most problematic, in terms of controlling emissions, and the most efficient when compared to modern PFI engines.

1.2 Goals and objectives

The primary purpose of this investigation is to provide an answer to the straightforward question of whether bulk quenching of the fuel cloud at the lean periphery occurs during typical light load operation in a DISI engine. As will be described in Chapter 2, several previous studies argue for the existence and even prevalence of bulk flame quenching as a hydrocarbon emission mechanism in DISI engines. These studies utilized indirect measures and observations such as exhaust gas sampling, computational simulations, and in-cylinder gas sampling to arrive at these conclusions. To the knowledge of this author, no direct observation of bulk quenching has been reported in the literature. To this end, the primary goal of this study is to provide direct evidence for the presence of unburned fuel at the periphery of the stratified cloud after flame propagation during light-load operation in a DISI engine. This will be accomplished through the use of planar laser-induced fluorescence (PLIF) experiments in an optically accessible DISI engine. Fluorescence from OH is used to track the

progression of combustion by monitoring the formation of products. Unburned fuel is visualized and quantified via the fluorescence of 3-pentanone doped in the iso-octane fuel.

Factors influencing the bulk flame quenching process will also be investigated. Included in these are engine operating conditions such as injection timing and ignition timing, which dictate the level of stratification and location of the combusting fuel cloud. Variations in the air intake pressure will also be investigated with respect to their effect on bulk quenching. Lower air intake pressures lead to more rapid mixing, due to lower cylinder gas densities, and to higher equivalence ratios for a given mass of fuel injected.

The previously described goals of this study are largely qualitative in nature. In addition to these, the equivalence ratio of the unburned fuel after combustion will be quantified. The calibration and equivalence ratio quantification method is described and implemented in Chapter 4. Application of this method under the conditions present in-cylinder late in the combustion cycle, when quenching is likely to occur, is more problematic, as described in Chapter 5.

1.3 Outline and overview

This thesis is organized as follows. Chapter 2 presents a review of relevant literature. This consists of an overview of direct-injection spark-ignition engine research, with emphasis on the hydrocarbon emission mechanisms pertinent to this study, as well as a summary of planar laser-induced fluorescence research of importance to the current investigation. Chapter 3 describes the experimental setup used in this study, consisting of the three primary components 1) the DISI engine, 2) the lasers/optical assembly, and 3)

the imaging system. Also addressed in Chapter 3 is the image correction procedure used. Chapter 4 summarizes the results of flame structure visualization experiments. Chapter 5 presents results obtained pertaining to the bulk quenching of the flame at the lean periphery of the fuel cloud. Chapter 6 provides concluding remarks. An additional direction of research pursued was a fractal analysis of the flame structure, which is presented in Appendix A.

2 Literature Review

2.1 DISI Engines

2.1.1 Motivation for DISI research

The concept of a direct-injection spark-ignition (DISI) engine that combines the high thermal efficiency and fuel economy of a diesel with the starting and driving characteristics of a homogeneously charged (premixed) spark-ignition engine has received nearly continuous study since the advent of the internal combustion engine. Prolific production of the DISI engine, however, has been hampered by several problems, such as an inability to control emissions of unburned hydrocarbons at light loads, emissions of NOx, as well as the reliable generation of an ignitable mixture. In spite of such technical obstacles, Mitsubishi, Nissan, and Toyota have all produced DISI engines for the Japanese market, and the Mitsubishi engine has been approved for sale in Europe. The primary motivation for continued development of DISI technology is the practical realization of fuel savings of up to 40% over modern premixed spark-ignition engines which have been reported under light load operating conditions.

2.1.2 DISI fundamentals

By utilizing direct-injection one seeks to exploit gains in efficiency resulting from higher compression ratios and increased specific heats [22]. Conventional homogenously charged engines operate at a stoichiometric fuel-air mixture due to restrictions imposed

by the use of three-way catalysts necessary to meet emission standards [6]. In addition to incurring throttling losses under light load conditions, such operation limits the maximum compression ratio in order to avoid engine knock. Under light loads, the DISI engine operates in a stratified mode with minimal throttling losses and lean mixtures (increased specific heat ratios), and, therefore, improved thermal efficiency [22]. Also, during stratified operation combustion occurs in isolated regions within the cylinder, reducing the contact between burnt gases and cylinder surfaces and thus leading to lower heat losses [45].

Essential to performance of the DISI engine are control and understanding of the distribution of fuel within the cylinder at the time of ignition. This requires familiarity with both the fuel spray characteristics and its interaction with the cylinder flowfield and piston surface between the times of injection and spark. In examining fuel distribution effects, it is often useful to divide DISI operating conditions into two categories, homogeneous and stratified modes corresponding to heavy and light load operation respectively.

During homogenous operation, the DISI engine attempts to function in a manner similar to modern premixed engines. The fuel is injected early to allow for thorough mixing with air in the cylinder. At the time of spark the mixture is close to homogenous throughout the cylinder, analogous to a premixed charge. Response to varying load is achieved through modification of the mass flows of both fuel and air during the injection and intake. Ideally, under heavy loads and homogeneous operating conditions, performance of the DISI engine should be the same as for a premixed engine.

Under light load conditions, the strategy of a direct-injection system is to utilize the interaction between the fuel spray, cylinder flowfield, and cylinder geometry to place an ignitable fuel cloud capable of producing the desired energy release at the spark plug location at the time of ignition [22]. The mixture within the cylinder is overall lean, but the stratified fuel cloud should be near stoichiometric to slightly rich by the time it moves past the spark for ignition. Placement of the fuel cloud is controlled via injection timing, injection duration, swirl and tumble of the spray, and impingement on the piston surface [17].

Although stratified operation has the potential to yield significant gains in fuel economy for the reasons previously described, these gains remain largely unrealized due primarily to emission-related issues [17] [20]. Of particular concern are the emissions of NOx [17], unburned hydrocarbons [2] [21], and soot [42]. Excessive soot can be generated as a result of insufficient mixing when the fuel distribution near the spark plug is overly rich at the time of ignition [42]. Increased NOx production is caused by local combustion at equivalence ratios near stoichiometric and typically requires after treatment of the combustion products to provide acceptable emission levels [17]. Unburned hydrocarbon emissions have several possible sources that will be discussed in greater detail in Section 2.1.5, although it is largely accepted that piston wetting by the fuel spray and quenching of the flame at the lean periphery of the fuel cloud are major contributors [20].

2.1.3 Historical development of the DISI engine

The earliest realizations of a direct-injection engine date back to the mid 19th century. The vertical Hugon engine operated without compression by igniting a locally rich mixture in an overall lean chamber volume [22]. In 1876 Otto introduced a compression engine renowned for its quiet operation that operated using stratified concepts [22]. DISI research has received continued but moderate attention until experiencing a resurgence of interest in the 60's and 70's as a result of fuel economy and (ironically) emission concerns [22].

The Ford PROCO and Texaco TCCS are among several DISI engines that were developed in the late 50's and studied extensively for several decades [4] [22]. Insight provided by these studies has guided subsequent development but is not necessarily indicative of the focus of current DISI research. This is largely a result of advances in spray technology relating to atomization and repeatability and the advent of electronic control. Many of these early systems relied upon ignition of the spray very close to the injector [22], but large cycle-to-cycle variability due to injector characteristics and in-cylinder turbulence led to reliability problems.

The class of modern DISI engines considered here operate essentially as follows. Ideally, a well-controlled spray with a high degree of atomization is injected. The injection angle is chosen to promote swirl and/or interaction of the fuel spray with the piston surface [1]. Utilizing swirl, intake-induced tumble, or piston rebound, the fuel cloud is directed toward the spark plug location. In order to allow for complete vaporization and adequate development of the fuel cloud, distances from the injector to the spark location are significantly larger than earlier DISI engines. This has drastically reduced the occurrence of unburned hydrocarbon emissions resulting from large fuel

droplets passing through the combustion zone, subsequently evaporating, and moving out with the exhaust gases [20]. Many problems remain, however, in controlling hydrocarbon emissions and therefore utilizing the full potential of stratified combustion.

2.1.4 Problems with stratified combustion

At loads above about 40 - 60%, the DISI engine must be operated in a homogeneous mode to provide the necessary power output [17]. Such operation is analogous to combustion in a port-fuel injection (PFI) engine, ideally resulting in identical fuel efficiency. At lighter loads, however, implementation of stratified combustion has the potential to yield improved fuel economy as described previously. As mentioned, the primary difficulties relate to pollutant emissions, including unburned hydrocarbons, NOx, and soot. This sub-section briefly addresses these emission problems, while the following sub-sections will focus on the hydrocarbon emission mechanisms, particularly lean quenching of the fuel cloud, relevant to the current investigation.

Formation and emission of NOx inhibit the implementation of DISI technology for several reasons. The primary two are difficulty in meeting emission standards and an increase in fuel consumption [17]. NOx formation occurs naturally at the temperatures and time scales of essentially all internal combustion engines. In modern PFI engines, NOx formation of premixed, stoichiometric combustion is controlled through the use of 3-way catalysts [6] as well as through exhaust gas re-circulation (EGR) [17]. Similar NOx controls are available for DISI combustion using homogeneous, near stoichiometric combustion.

At lighter loads, however, an alternate NOx control strategy must be employed. Catalysts used for premixed, stoichiometric combustion are not effective at reducing NOx emissions for the off-stoichiometric combustion present under stratified and lean (homogeneous) operating conditions [6]. EGR is still effective for lean, homogeneous combustion, but fails to sufficiently control NOx emissions during stratified combustion [17]. One possible method for NOx reduction is the use of after-treatment [17], although this can be an expensive process.

Soot formation occurs during stratified combustion when locally rich regions of fuel burn. Other than avoiding excessively rich combustion mixtures, the primary defense against soot emission is effective after-treatment.

Several researchers have investigated possible mechanisms for the emission of unburned hydrocarbons [3] [18] [21] [24] [26]. The discussion of Casarella & Ghandhi, 1998 [20] summarizes ten emission mechanisms described throughout the literature. Several of these mechanisms are well understood and can be effectively remedied through appropriate design measures, while others require continued investigation to develop effective treatments.

The hydrocarbon emission mechanisms identified in [20] that can be largely obviated through appropriate design include: large droplets from the fuel spray, short-circuiting of unburned fuel, crevice/injector sac volume, burn phasing/burn rate, and cylinder deposits/oil films. Results of Drake et al, 1996 [21] suggest that fuel trapped in the injection crevice (along with quenching of the fuel cloud) represents a primary source of hydrocarbon emissions. Advances in injection technology (spray atomization, design, repeatability) have led to significant reductions in injector related emissions. Improved

injection quality has also allowed control of hydrocarbon emissions that result from large droplets passing through the combustion zone and subsequently evaporating [20] [22] by providing a fuel spray with a high degree of atomization. Development of improved design and injection strategies have significantly reduced emissions resulting from burn phasing/burn rate issues and short-circuiting of unburned fuel, although the latter can still be problematic for some two-stroke systems. Cylinder deposits and oil films that adsorb hydrocarbons during combustion and subsequently release them as emissions remain a mechanism of concern. Possible remedies are design modifications to reduce soot production in the cylinder and oil interaction.

2.1.5 Hydrocarbon emissions: Piston wetting –vs- Bulk flame quenching

Among the remaining emission mechanisms identified in [20] are over-mixing of the fuel spray, poor combustion quality, piston wall wetting, burning zone A/F ratio, and prior cycle interactions. Excluding piston wetting, the remaining five emission mechanisms are all closely related. For example, an excessively over-mixed spray leads to poor combustion quality, low and relatively homogeneous A/F ratio distributions, and may increase the frequency of misfires, which negatively influences subsequent engine cycles. These five mechanisms are consolidated into essentially two ‘mechanisms’, bulk quenching of the flame at the lean periphery of the fuel cloud and injection/combustion timing issues. The latter is a catch all classification that includes hydrocarbon emission mechanisms that must be obviated through fuel distribution controls such as injection timing, cylinder pressure at the time of injection, and the ignition timing, as well as through the use of flowfield and geometric controls previously described. The following

discussion will be limited to the two mechanisms, piston wall wetting and bulk quenching.

Interaction of the fuel spray and the piston and bowl surfaces is a necessity of stratified DISI combustion. This interaction leads to the deposition of a liquid fuel film. The fuel film is isolated from the main combustion event due to the stratified nature of the fuel cloud, subsequently evaporates, and exits with the exhaust gases. Computational models utilizing multi-dimensional simulations of a hollow cone spray impinging on a flat topped piston under typical injection conditions demonstrate that up to 8 - 10% of the total injected fuel is present as a liquid film at the time of ignition [17].

Bulk quenching of the fuel cloud occurs during stratified combustion when steep gradients in the local equivalence ratios are present due to the lack of mixing time. Presumably, a stoichiometric to slightly rich mixture is present at the spark plug location at the time of ignition. As combustion is initiated via the ignition event, the flame kernel grows, expanding outward away from the spark plug location. The advancing flame front consumes fuel as it progresses through the cylinder. Since the overall equivalence ratio within the cylinder is lean during stratified combustion, as the flame burns outward it eventually enters a region of excess air. At some point, the local equivalence ratio in this region becomes too lean to support the flame propagation and the flame quenches.

Numerous studies have investigated the relative importance of these two mechanisms on total unburned hydrocarbon emissions [4] [5] [18] [21] [24] [27]. Frank and Heywood [18] examined the influence of piston temperature on total hydrocarbon emissions. Their results showed no significant changes in the level of emissions as the piston temperature was varied, leading them to conclude that piston wetting was not a

prevalent emission mechanism. Drake et al. [21] used laser-induced fluorescence (LIF) experiments combined with exhaust hydrocarbon sampling and found that misfires, partial burns, and fuel trapped in the injector nozzle-exit crevices were the primary hydrocarbon emission mechanisms, not piston-wall wetting. Fansler et al. [27] reported similar results. Ingham et al. [4] used a sampling probe in the piston bowl to measure the post combustion hydrocarbon content in the cylinder. While some of the unburned fuel was attributed to quenching near the walls, significant production of fuel from the bowl surface was observed, indicating the presence of an evaporating fuel film [4]. Hudak and Ghandhi [5] obtained similar results using gas composition measurements at the exhaust port. About half of the total unburned hydrocarbon emissions resulted from fuel film evaporation after the opening of the exhaust port [5]. Stanglmaier et al. [24] used an injection probe located behind the spark plug to examine the effects of cylinder wall wetting by varying the location and timing of the wetting event. It was concluded [24] that wall wetting was a major contributor to unburned hydrocarbon emissions, but due to the contrived nature of the experimental setup, these conclusions cannot be extended to actual DISI engines.

As demonstrated, significant conflict exists as to the relative roles of these mechanisms on the overall unburned hydrocarbon emissions. One problem with attempting to determine the primary or dominant emission mechanisms is the large variability in DISI engine design and operation. As pointed out in [24], many of the studies that observed wall wetting to have no significant effect on hydrocarbon emissions were conducted on older style DISI engines, which ignited the fuel cloud very close to the injector during the injection event. Although there are exceptions to this observation

(notably [4]), the general conclusion, that the design and operation of the particular DISI engine being studied are major factors influencing the relative contribution of piston wall-wetting and bulk quenching of the flame to the total unburned hydrocarbon emissions, seems valid.

For the engine configuration used in this study, piston wetting is assumed to be a significant source of hydrocarbon emissions. Besides piston wetting, quenching of the fuel cloud and misfires/partial burns are also considered as possible contributors. Misfired and poorly burned cycles have been documented but their roles in overall hydrocarbon emissions have not been examined. Piston wetting and quenching will be considered as sources of unburned hydrocarbons for the typical engine cycle of the DISI engine used in these experiments. It is the possible role of lean quenching that is investigated in this study.

2.1.6 Bulk flame quenching of the flame at the lean periphery

The primary questions relating to bulk quenching of the flame in the lean periphery of the fuel cloud involve the extent to which it contributes to the overall emission of unburned hydrocarbons (as described in Section 2.1.5) and the influence of the conditions in-cylinder on the quenching phenomena. This section will focus on the latter. It is generally accepted that during stratified combustion quenching does occur at the lean periphery of the fuel cloud. The fate of the unburned hydrocarbons has been considered by several investigators [2] [17] [22] . Of particular concern are the in-cylinder conditions that influence post-combustion oxidation of left over fuel.

Giovanetti et al. [2], assuming a homogeneous distribution of the unburned fuel and an Arrhenius form for the chemical ignition delay correlation, characterized the likelihood of post-combustion oxidation by an ‘elapsed fraction of ignition delay’. Accounting for the cumulative effects of varying temperatures and pressures in the cylinder, post-combustion mixtures that exceeded an elapsed fraction of ignition delay of unity underwent spontaneous ignition [2]. Results showed the following general trends [2]. Unburned hydrocarbons are unlikely to undergo secondary burn-up at light loads, while at heavy loads secondary burn-up is likely. Promotion of post-combustion oxidation at light loads requires higher cylinder pressures and temperatures.

Other researchers have focused on a minimum temperature necessary to instigate post-combustion oxidation of the left over fuel [17]. All three studies used iso-ocatane as fuel in a DISI engine (simulated or experimental) and report a minimum temperature for secondary burn-up in the range of 1150 K to 1500 K. The wide range of temperatures likely results at least partly from variations in the heat transfer properties of the respective engines.

2.2 Planar laser-induced fluorescence

Laser-induced fluorescence (LIF) has become a common diagnostic tool for visualizing reacting and non-reacting flows. The fundamental physical principles governing LIF have long been known. A thorough review of the subject is given in [13], upon which the following discussion is loosely based. LIF experiments utilize photons of known energy (i.e. laser light of known wavelength) to excite a target species of known absorption/emission spectrum from a low energy quantum mechanical state to a higher

energy quantum state. Transfer of the energy among nearby states is followed by the return to the (near) ground state and the associated spontaneous emission of a photon. The laser light illuminates an area of interest, and the distribution of the target species is determined by collecting and imaging the emitted photons.

Quantification of local target species concentrations and number densities requires a more detailed examination of LIF. Based upon the power of the laser used for excitation, the fluorescence is said to be in either the saturated or linear (unsaturated) regime. In the linear fluorescence regime, the combined effects of laser energy density, pulse duration, and repetition rate are small enough such that the re-population of the lower energy laser-coupled state is sufficiently fast that steady state assumptions are valid, and the fluorescence energy density is directly proportional to the local target species number density. In the saturated regime, however, the lower energy state becomes depleted during the LIF process, affecting the rates of absorption and emission and leading to a non-linear relationship between the fluorescence energy and the local concentration.

2.2.1 LIF of OH

Extensive research exists on the photo-physical properties of OH due to its natural presence as a combustion product and its excitation at UV wavelengths conveniently accessible on many laser systems. A detailed description of the OH spectrum in the UV range is given by Dieke and Crosswhite [10]. The OH spectrum consists of discrete rotational, vibrational, and electronic energy states [10] [30], analogous to the simple Bohr model. Even in the linear fluorescence regime, quantification of local OH

concentrations is difficult in practice due to the complex relationship between the fluorescence energy density and temperature, pressure, quenching, and attenuation effects.

Several models have been proposed to represent the excitation dynamics of OH [32] [70] [71] [72] [30]. Essentially, these models attempt to simplify the system of linear differential equations by consolidating the energy levels. Typically, 2, 4, and 5 level models are used to represent OH, where the transition rates between the various energy levels due to quenching, laser-induced stimulation, laser-induced emission, spontaneous emission, and collisional/rotational relaxation as well as the dependence of these rates on temperature and pressure, remain the subject of ongoing research.

This study uses OH fluorescence only as a qualitative indicator of the presence of burned gases. As such, subsequent discussion of OH fluorescence will focus on PLIF of OH as a visualization tool.

2.2.2 LIF of 3-pentanone

For the current discussion, 3-pentanone and acetone will be referred to together as the ketones, because they are very similar spectrally [8] and a wide body of literature exists on acetone fluorescence. Where appropriate differences between them will be addressed. The ketones and OH differ significantly in their photo-physical properties. The ketones do not absorb photons in discrete energy bands but rather absorb in a continuous spectrum in the UV range from about 250 nm to 300 nm [37] and then undergo a rapid intersystem crossing. The corresponding emission spectrum occurs in the visible range at approximately 400 nm to 550 nm [37]. This non-radiative relaxation,

combined with the simplified spectral dynamics of the ketones (compared to OH), facilitates the quantification of local number densities or temperature [9] [31] [36].

In order to quantify the ketone fluorescence, the temperature and pressure dependencies must be accounted for. Thurber et al. [31] provide a detailed examination of the relationship between the fluorescence energy and temperature for numerous wavelengths. Results show that for an excitation wavelength of about 282 nm the temperature dependence of the fluorescence signal is very small, remaining quite flat from about 300 K to 800 K [31]. Similar experiments have been performed to examine the pressure effects [39], but the correction scheme presented in Chapter 3 obviates the need for quantifying the pressure dependence.

2.2.3 Planar laser-induced fluorescence in DISI engines

PLIF techniques have been applied much more extensively to diesel and typical PFI engines than to DISI engines. Most of the available PLIF studies of DISI engines have focused on the visualization [21] [29] [50] and quantification [28] of the distribution of fuel. Fansler et al. [29] and Drake et al. [21] utilized fluorescence of unknown components of gasoline to visualize the fuel distribution during injection [21] [29] as well as later, near the ignition time [29]. Tabata et al. [50] used acetone and naphthalene dopants to obtain fuel distribution images over a wider range of times, from the injection through the early times of combustion. Resulting images provide visualization and demonstrate the consumption of the fuel.

Fujikawa et al. [28] quantified the local fuel concentrations in a DISI engine using acetone dopant and accounting approximately for the temperature and pressure effects on

the fluorescence intensity. Aside from errors incurred by temperature and pressure dependence assumptions, there are problems with the correction method used that affect the validity of the quantification of the local equivalence ratio, namely the use of an arbitrary and undefined correction factor to account for window fouling and laser power fluctuations and averaging the data images over 16 engine cycles to reduce cycle-to-cycle variations and spatial fluctuations in the laser sheet [28].

3 Experimental setup

The experimental setup utilized for this study consisted of three fundamental components, the optically accessible DISI engine and related hardware, the laser system and optical assembly, and the fluorescence collection system (intensified CCD camera, lenses, and filters). Figure 3.1 illustrates the basic layout of these components. They will be discussed in more detail in the following sections. The lasers and associated optics were used to produce a sheet of monochromatic light, which illuminated a plane of interest within the cylinder of the DISI engine. Laser-induced fluorescence of the cylinder gases emitted perpendicular to the sheet was reflected out of the engine, filtered, and then collected with the camera. Fluorescence images of both unburned gases (via 3-pentanone doped into the fuel) and burned gases (via the hydroxyl radical OH present naturally in the combustion products) have been obtained.

This chapter describes briefly the three components of the experimental system mentioned above. Sections 3.1, 3.2, and 3.3 describe the optically accessible DISI engine, the laser system and optical assembly, and the imaging system, respectively. Section 3.4 describes the image correction and calibration procedure used to quantify local equivalence ratios from the 3-pentanone fluorescence images.

3.1 Optically accessible engine

The single-cylinder, four-stroke, optically accessible DISI engine utilized in these experiments is illustrated in Figure 3.2a, and the specifications are listed in Table 3.2. The engine had a 9.24 cm bore, a 7.62 cm stroke length, and a 9.8:1 compression ratio, although blowby past the piston rings caused a slight loss of mass and therefore a small reduction in the actual compression of the cylinder gases. The engine combustion chamber featured a flat top piston with an off-center re-entrant piston bowl. This chamber was designed for swirl-affected wall-guided operation. Swirl was achieved through the design of the intake runner, which was oriented approximately tangent to the piston bowl producing counter-clockwise swirl when viewed from above. A Chrysler high-pressure-swirl injector operating at a fuel rail pressure of 5.2 MPa was directed tangentially into the cylinder bowl in the swirl direction at an angle of 70 degrees relative to the piston crown (20° from the piston normal direction) [7], Figure 3.2b.

The tangentially oriented fuel spray from the injector was used to prepare the fuel mixture distribution for both the early injection case, with an end of injection (EOI) at 180 degrees before top dead center (BTDC), and the late injection stratified case, with EOI occurring between 40 and 65 degrees BTDC. Under stratified operating conditions the combination of spray rebound from the bowl surface and intake-generated swirl convected the fuel cloud to the spark plug location.

The fuel used for this study was a mixture of 5% 3-pentanone and 95% isooctane by volume. Since the boiling points of these liquids are nearly identical (99°C and 102°C

respectively), fractional distillation did not influence the evaporation process and local 3-pentanone concentrations were directly proportional to local fuel concentrations.

Number	Description
1	Collimating lens and Pellin-Brocca prism
2	Pellin-Brocca prism
3	Coverging spherical lens (f = 1m)
4	Reflecting prisms
5	Reflecting prism
6	Diverging cylindrical lens (f = -25 mm)

Table 3.1. Description of the optical components of Figure 3.1.

Optically accessible, single cylinder, four stroke DISI engine data		
Bore	[mm]	92.4
Stroke	[mm]	76.2
Compression ratio		9.8
Connecting rod length	[mm]	145.2
Squish ratio		0.27
Bowl diameter	[mm]	48
Bowl depth	[mm]	10

Table 3.2. Engine data for the DISI engine used in this study.

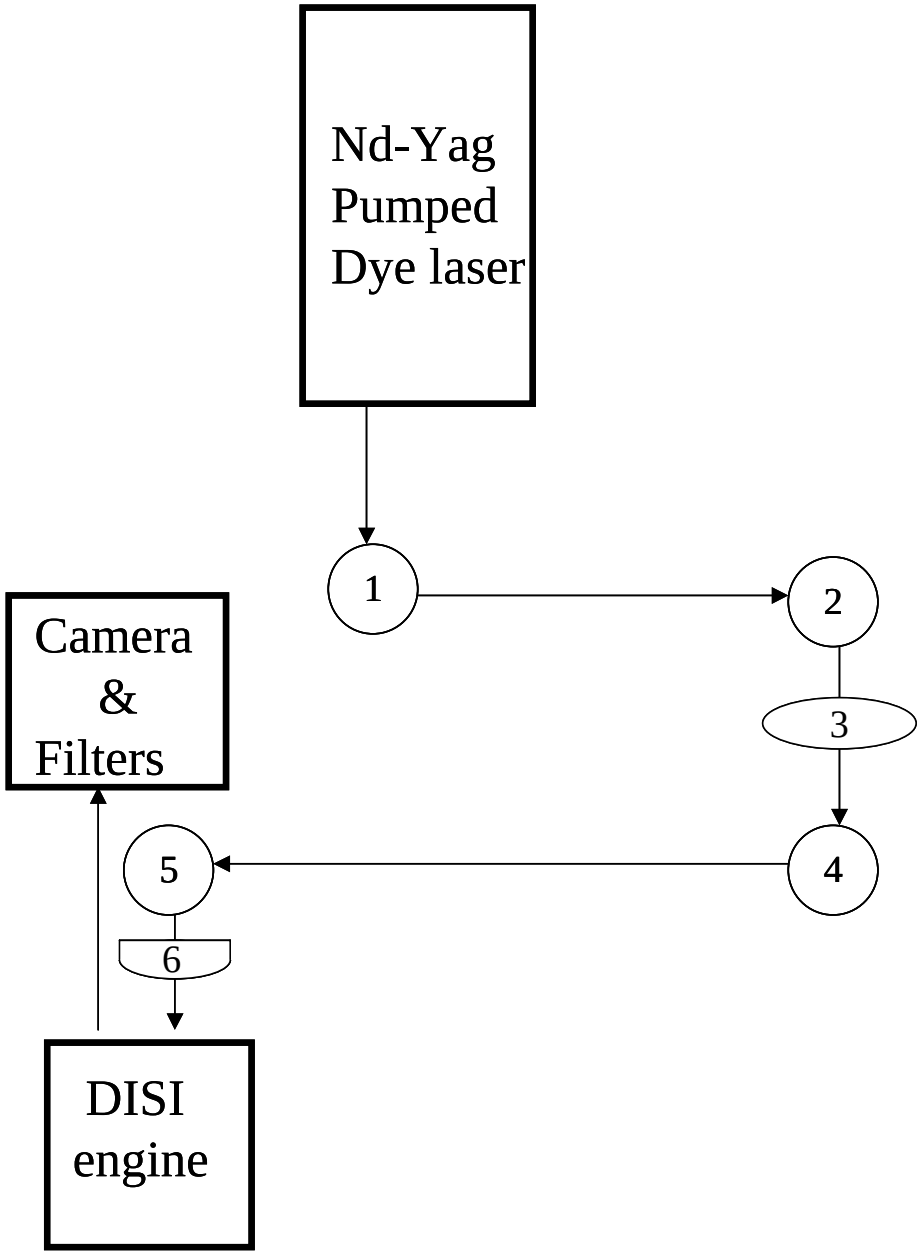

Figure 3.1. Layout of the experimental setup, showing the relationship between the three primary components and the path of the laser.

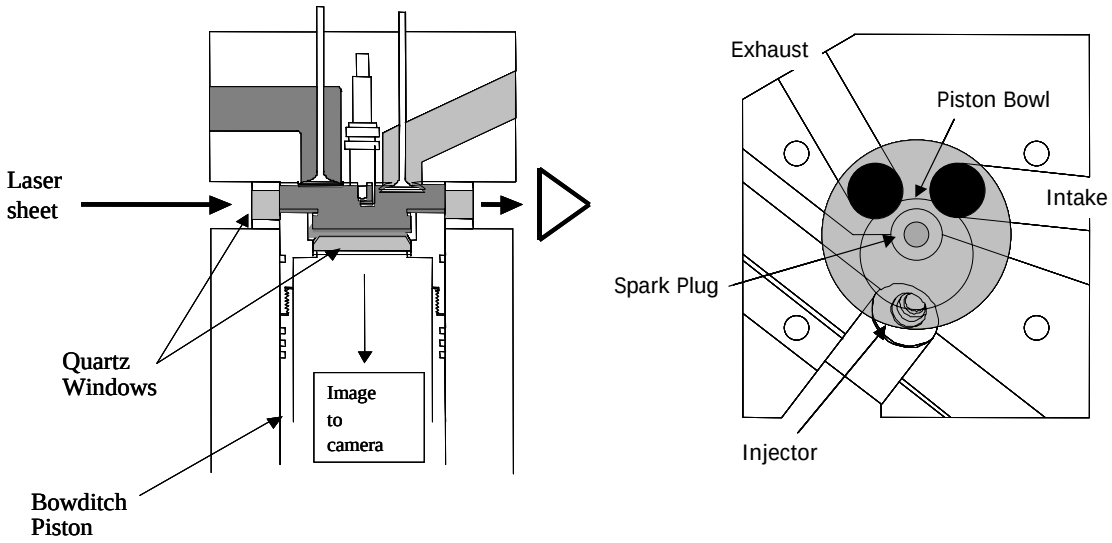

Figure 3.2. (a) Layout of the single cylinder DISI engine used in the study, showing the general layout and optical access. (b) Orientation of the injector, piston bowl, spark plug, and intake and exhaust valves.

3.2 Laser system and optical assembly

A Neodynium: Ytrium Aluminum Garnet (Nd:YAG) laser with an output of 1064 nm was frequency doubled to produce a beam of wavelength 532 nm. The 532 nm beam was separated from the other ND:YAG harmonics and passed downward into a tunable dye laser. Fluorescent dye and an adjustable grating allow the output wavelength to be tuned within a 0.5 nm range. The fluorescent dye used throughout this study was Rhodamine 6G, chosen to provide the output wavelength as described below. Lasing of the dye by the 532 nm pump beam occurred in two separate cuvettes within the dye laser, the pre-amplifier/oscillator cuvette and the final amplifier cuvette. The dye concentration in the pre-amplifier/oscillator was 0.12 g/L and the concentration in the final amplifier

was 0.04 g/L. For this study, an output wavelength of 567.85 nm was used. The optical assembly is shown in Figure 3.1. The ND:YAG laser sat above the dye laser on a custom-designed welded steel stand, and is not shown in the diagram.

The output of the dye laser was frequency doubled to 283.92 nm (1 in Figure 3.1). Two Pellin-Brocca prisms were used to separate the UV beam from the host 567.85 beam (1 and 2). The UV light then passed through a series of reflecting optics (2 and 4) and a spherical lens (3) of focal length 1 m placed 1 m upstream of the cylinder. The large focal length led to a sheet of relatively constant thickness, approximately 200 μm, across the imaging area. Periodically, an additional cylindrical lens (f = 10 cm) was used (not pictured in Figure 3.1). This lens was placed between (4) and (5) about 25 cm downstream of the spherical lens (3) to provide both increased divergence of the laser sheet and reduced laser intensities at the optics (5) and (6). After passing through a final reflecting prism (5), the expanding sheet went through a negative cylindrical lens (f = -25 mm), which greatly increased the angle of divergence for maximum illumination area (6). The sheet width at the entrance was limited to the window size, which varied between 24 mm and 18 mm, depending on the height of the laser sheet. The sheet-forming optics were developed throughout the course of this study. Continued refinement led to variations in the sheet size and divergence angle. The described system represents the final configuration and is the method used for most of the images presented.

The UV excitation wavelength of λ_e = 283.92 nm was chosen to minimize the temperature dependence of the 3-pentanone fluorescence signal [8,9]. The 3-pentanone fluorescence was also free of quenching effects due to a rapid intersystem crossing that

depletes the excited singlet state. The 3-pentanone emission is from 400 to 600 nm. The lack of quenching and temperature dependence of the fluorescence allowed the quantification of local fuel concentrations. OH fluorescence was generated using the same excitation wavelength (λ_e = 283.92 nm) pumping the (1,0) line of the A←X transition [10-12]. Redistribution among nearby rotational and vibrational energy levels caused a red shift of the emitted radiation, which was collected in the approximate range of 290 nm to 310 nm. The power of the UV beam was generally maintained between 10.5 mJ/pulse and 13 mJ/pulse, which was sufficient to induce strong fluorescence in both the 3-pentanone and OH.

The laser sheet entered and exited the combustion chamber through quartz windows located in a spacer ring just below the cylinder head. The quartz windows were 17 mm thick in the direction parallel to the laser propagation. The planar window surface perpendicular to the laser propagation direction provided an approximately elliptical area for the laser sheet to enter, with major radius 24 mm in the horizontal plane and minor radius 14 mm in the vertical plane. This area limited the dimensions of the laser sheet upon entry into the engine. The thickness of the laser sheet (vertical direction) was about 200 μm. The width of the sheet (horizontal direction) was matched approximately to the window size, depending on the height of the laser sheet, in order to maximize the amount of laser energy entering the engine cylinder.

As the piston moved to top dead center (TDC), it covered all except the top 2 mm of the quartz window. It was therefore necessary to adjust the height of the laser sheet depending on the crank angle (CA) at which the images were to be obtained. Table 3.1

shows the maximum sheet width, height of the piston top above the bottom of the window, and the distance of the laser sheet from the spark gap, for various CA. For crank angles further than about 8 degrees from TDC, the sheet was centered in the window to maximize the field of view in the cylinder.

The laser sheet illuminated a plane parallel to the piston crown near the axial location of the spark plug gap. The laser sheet continued to diverge as it traversed the piston bowl. The width of the sheet in the viewing area within the cylinder depended not only on the sheet width at entry into the engine but also on the divergence angle of the laser sheet. Due to continued modifications of the sheet forming optics throughout the course of these experiments, the divergence angle was not constant. The sheet width was generally between 20 mm and 30 mm at the center of the imaging location.

Within the volume illuminated by the laser sheet, both OH and 3-pentanone molecules absorbed photons at the excitation wavelength. The induced fluorescence of each species (at the wavelengths described above) was emitted in all directions. Photons emitted perpendicular to the laser sheet passed downward into the cylinder. The bottom of the piston bowl had a sapphire window that allowed the fluorescence to continue downward, through the extended Bowdich style piston. An aluminum coated UV mirror reflected the light out of the engine and to the imaging system.

3.3 Imaging system

The resulting images were captured on a Roper Scientific PI-Max-512-T intensified CCD camera using short gate times (~90 ns). For collection of 3-pentanone fluorescence, a f/2.8 visible lens with glass substrates was utilized. Since glass elements

do not transmit light in the UV range, filtering of the pumping wavelength was not necessary. When imaging OH, a f/4.5 UV Nikkor lens, with a long wave pass filter (Schott glass, 305 nm cutoff) and a short wave pass filter (360 nm cutoff) to remove scattered laser light as well as the visible 3-pentanone fluorescence, was used.

Figure 3.3 shows the camera field of view relative to the piston bowl and cylinder liner, along with the area illuminated by the laser sheet and the direction of swirl. The sheet entered the cylinder on the injector side of the bowl and traversed the chamber. The magnifications were slightly different for the two lenses, although the fields of view were adjusted to be nearly the same, consisting of the sheet area between the injector and spark plug. Figure 3.3 represents the field of view using the visible lens.

The images collected with the camera were corrected for dark noise, background noise and spatial variations in the laser sheet intensity. The dark noise and background noise correction consisted of subtracting an average background signal from the

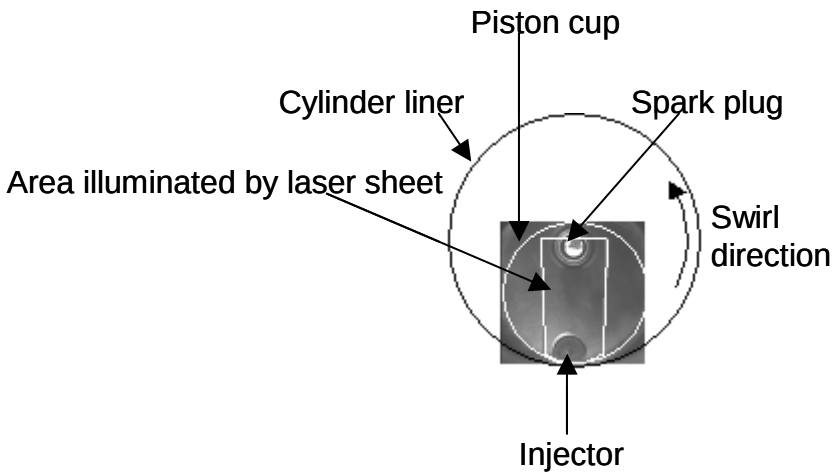

Figure 3.3. Orientation of the laser sheet relative to the cylinder liner, piston cup, spark plug, and injector. The counter-clockwise swirl direction is illustrated by the arrow.

individual data images, obtained by imaging the laser sheet with no fuel or combustion products present. This removed laser flare caused by reflection of the laser sheet off the spark plug, piston bowl, and cylinder liner. The images were then calibrated and corrected for spatial variations in the laser sheet by performing a pixel-by-pixel ratio of the background-corrected image to a background-corrected flatfield image of a known equivalence ratio mixture. These ratios were then used to determine the local equivalence ratio, as described in the following.

3.4 Image correction procedure

The rate at which fluorescence photons strike the detector, $\dot{S}$ [photon/s] can be obtained from the light scattering equation [13]

$$\dot{S} = \left[\frac{INV\left(\sigma_{abs}/4\pi\right)\phi\Omega\eta_{opt}}{h\nu} \right] \tag{1}$$

where I is the laser intensity [J/m^2-s], N is the fluorescing species number density [m^{-3}], V is the volume being illuminated [m^3], $\sigma_{abs}/4\pi$ is the differential absorption cross-section of the fluorescing species [m^2], ϕ is the fluorescence efficiency, Ω is the collection solid angle [sr], η_{opt} is the collection efficiency of the optical system including filters, h is Planck's constant [J-s], and υ is the frequency of the fluorescence photons [s^{-1}]. Integrating over the laser pulse duration and assuming a square pixel of length l, one gets the following relation for the measured fluorescence signal, S

$$S = \left[\frac{E(x,y)N(x,y)l\left(\sigma_{abs}(x,y)/4\pi\right)\phi(x,y)\Omega\eta_{opt}}{h\nu} \right]\eta_{\text{det}} \tag{2}$$

where E is the laser pulse energy [J], η_{det} is the detector efficiency and the spatial dependences have been added to the appropriate terms. The absorption cross-section and fluorescence efficiency terms have a spatial dependence due to their dependence on temperature and pressure, where the former need not be uniform under direct injection.

Performing a ratio of a background-corrected raw image, S_{im}, to a background-corrected calibration image, S_{cal}, results in

$$\frac{S_{im}}{S_{cal}} = \frac{\left\{E(x,y)N(x,y)\sigma_{abs}(x,y)\phi(x,y)\right\}_{im}}{\left\{E(x,y)N(x,y)\sigma_{abs}(x,y)\phi(x,y)\right\}_{cal}}. \tag{3}$$

By choosing to obtain our calibration image at the same (only possible for pre-combustion images), or nearly the same crank-angle as the raw image, large changes due to temperature and pressure effects on the absorption cross-section and fluorescence efficiency can be obviated. Further, at the chosen pumping wavelength the product of $\sigma_{\text{abs}}\phi$ has been found to be nearly independent of temperature, so small temperature differences within the field will only mildly impact the results. If shot-to-shot variations in the laser energy are neglected, the ratio of equation 3 can be seen to revert to the ratio of the fluorescing species number density in the raw image to that of the calibration image

$$\frac{S_{im}}{S_{cal}} \approx \frac{N_{im}(x,y)}{N_{cal}(x,y)}. \tag{4}$$

For hydrocarbon-air mixtures the fuel-air equivalence ratio, Φ, can be written as

$$\Phi \equiv \frac{\left(m_f / m_a \right)_{actual}}{\left(m_f / m_a \right)_{stoich}} = \frac{\left(N_f / \left(N_t - N_f \right) \right)_{actual}}{\left(N_f / \left(N_t - N_f \right) \right)_{stoich}} \tag{5}$$

where m is mass, N is number density and the subscripts f , a and t refer to fuel and air and total respectively. Since the fluorescence signal is directly proportional to the fuel number density, the ratio of the fuel-air equivalence ratios between the raw image and the calibration image can be written as

$$\frac{\Phi_{im}}{\Phi_{cal}} = \frac{\left(N_f / \left(N_t - N_f \right) \right)_{im}}{\left(N_f / \left(N_t - N_f \right) \right)_{cal}} = \frac{N_{im}}{N_{cal}} \left[\frac{N_t - N_{cal}}{N_t - N_{im}} \right] . \tag{6}$$

Because the typical fuel-air ratio is 1:15, and the molecular weights of fuel and air differ by a factor of approximately 4 for an iso-octane – air mixture, the ratio of number densities in the square brackets is close to unity (differing by about 1 part in 60) and the term can be neglected. The error associated with this is less than 2.5% for a range of $0.1 < \Phi_{im} < 2.5$ with a calibration image acquired at $\Phi_{cal} = 1$. Thus, using equation (4) it can be seen that performing the pixel-by-pixel ratio of background-corrected images to a calibration image provides a direct calibration for equivalence ratio (with errors as noted above)

$$\frac{S_{im}}{S_{cal}} \approx \frac{N_{im}(x,y)}{N_{cal}(x,y)} \approx \frac{\Phi_{im}}{\Phi_{cal}} . \tag{7}$$

For cases where combustion has commenced in the raw image but the calibration image was taken under motored, or pre-combustion conditions, the assumption regarding the

absorption cross-section and fluorescence efficiency remains valid, but the compression of the end gas from the pressure rise of combustion must be accounted for in the calibration procedure.

Assuming polytropic compression, it is straightforward to show that

$$\alpha = \frac{P_{comb}}{P_{cal}} = \left(\frac{N_{cal}}{N_{comb}}\right)^{\gamma} \tag{8}$$

where the value of the polytropic exponent γ =1.2 was determined from the experimentally obtained *P*-*V* diagram, P_{cal} is the cylinder pressure of the calibration image (taken without combustion at the same crank-angle as the data image), and P_{im} is the cylinder pressure of the data image at the crank-angle of the image. Then for $N_{\mathrm{im}} = N_{\mathrm{cal}}\alpha\text{^}(1/\gamma)$ as in (8), the local equivalence ratio calculated by the method described in Section 2 must be modified as

$$\Phi_{comb} = \Phi_{im}\alpha^{-1/\gamma} \tag{9}$$

The equivalence ratio scaling of all post-ignition figures reflects this correction.

The 3-pentanone images shown in the results were calibrated by the method described above with the flatfield image of known composition acquired under motoring conditions. The lack of combustion in the calibration image may give rise to a slight bias in the results due to the residual fraction in the cylinder under fired conditions. This does not affect the number density calibration, but it will impact the equivalence ratio (causing an underestimation).

In order to eliminate noise in regions outside of the laser sheet, a lower threshold was applied to the data, so signals that corresponded to an equivalence ratio of

approximately 0.05 to 0.1 were set to zero, depending on the noise characteristics of the data set. No spatial filtering was performed on the 3-pentanone images. The OH images were spatially filtered with a long pass filter to eliminate some of the noise associated with the relatively high intensifier gain. The integrity of the flame location was not affected by this filtering. Also, the gray level assignment chosen for the display of the images enhanced the contrast and minimized the impact of the beam absorption in the burned gases.

The series of images in Figure 3.4 demonstrate the progression of the image correction process for 3-pentanone images (Figure 3.4a) and for OH images (Figure 3.4b). Figure 3.4a shows a raw 3-pentanone image, followed by the calibrated (background and flatfield corrected) image. Figure 3.4b shows a raw OH image followed by the filtered, corrected image.

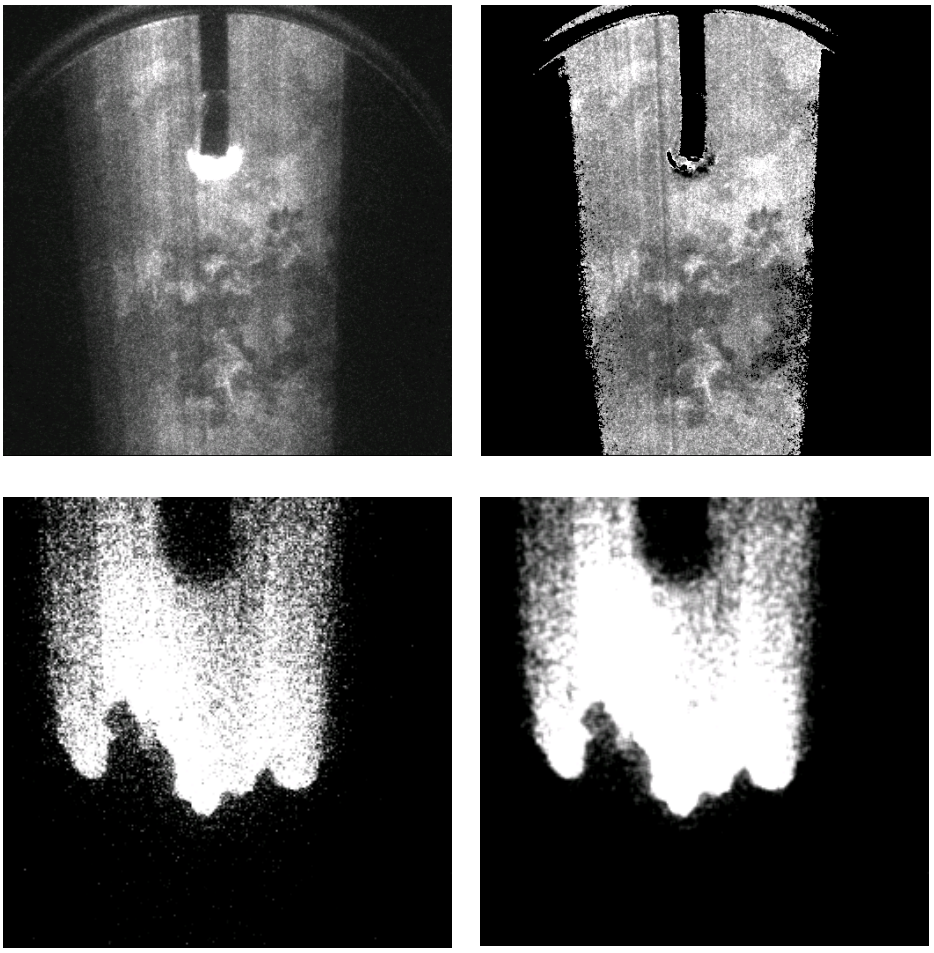

Figure 3.4. Illustration of the image correction process: Top row, 3-pentanone correction: raw image (left) followed by the background and flatfield corrected image, bottom row, OH correction: raw image (left) followed by the filtered image.

4 Flame structure visualization

4.1 Introduction

The focus of this chapter is to provide visualization results of the charge generation and combustion under the two basic operating modes of the DISI engine, the stratified mode and the homogeneous mode. Several operating conditions were studied for each case to both observe influences on the combustion process and demonstrate the capabilities of the PLIF system and the correction/calibration method used in this study.

The reasons for presenting flame structure visualization results are threefold. First, these experiments allow investigation and evaluation of the image correction and calibration procedure using conditions of known fluorescence species location and concentration. Second, they provide visualization of the effect of varying engine operating parameters such as injection timing, injection duration, and ignition timing on the charge development and the progression of combustion. Finally, imaging throughout the combustion process allowed identification of extraneous phenomena (e.g. flame luminosity) and patterns in the development and consumption of the fuel cloud and the flame propagation.

4.2 Conditions

Experiments were performed at two engine speeds, 600 rpm and 1200 rpm, and two loads, 450 kPa and 130 kPa IMEP (corresponding to fuel-air equivalence ratios of 0.7 and 0.3 respectively). The manifold pressure was atmospheric in both cases. The

light load results present, for the first time, a direct measure of the local fuel-air ratio during combustion for stratified-charge combustion.

Above a certain load, which depends on the engine design, a DISI engine must be operated in a nearly homogeneous mode to avoid excessive soot production that accompanies overly rich mixtures. The high load conditions examined in this study had a fixed injected fuel mass providing an equivalence ratio Φ=0.7 for both engine speeds. Homogeneous operation requires early injection of the fuel spray to allow for complete mixing of the fuel and air. An EOI of 180 degrees BTDC was used. In order to assess the effect of inhomogeneity resulting from direct in-cylinder injection of the fuel, tests were also performed using a fully premixed charge. The premixed charge was prepared by using an air-assisted injector mounted approximately 1 m upstream of the intake valve. The fuel system used was the same, so the fuel-doping rate was invariant.

The light load condition investigated in this study utilized a fixed fuel mass corresponding to an equivalence ratio of Φ=0.3 for both engine speeds. The IMEP and coefficient of variation (COV) of the IMEP as functions of injection (EOI) and ignition timing are illustrated in Figure 4.2. Based upon these data, baseline running conditions were chosen. At 1200 rpm the baseline EOI was 58° BTDC and ignition occurred at 22° BTDC. At 600 rpm the EOI timing was 48° BTDC with an ignition timing of 8° BTDC.

In order to examine the effects of varying the ignition and EOI timing on the fuel distribution at the time of ignition, several other running conditions were also examined. These conditions are listed in Table 4.1, and are identified in Figure 4.1. For each engine speed three additional conditions were investigated. In the ‘Advanced’ case both the

ignition and EOI were advanced nearly the same amount, leaving the dwell time between the two events unchanged. In the 'Retarded' case both injection and ignition were retarded the same amount from the baseline condition. In the "Advanced Injection' case the ignition time was unaltered, but the injection timing was advanced relative to the baseline, causing an increase in the allowable mixing time.

	Baseline		Advanced		Retarded		Advanced Injection	
speed	EOI	ign	EOI	ign	EOI	ign	EOI	ign
600 rpm	48	8	55	13	41	1	58	8
1200 rpm	58	22	65	27	51	15	68	22

Table 4.1. Stratified running conditions examined for Φ=0.3: End of injection (EOI) and ignition (ign) timing in crank angle degrees BTDC.

4.3 Flame structure visualization

4.3.1 High load flame structure

Figure 4.2 shows the results obtained for homogeneous mode operation by both direct injection of the fuel (right) and using the premixed charge (left) for engine speeds of 600 rpm and 1200 rpm. The progression of images depicts the development of

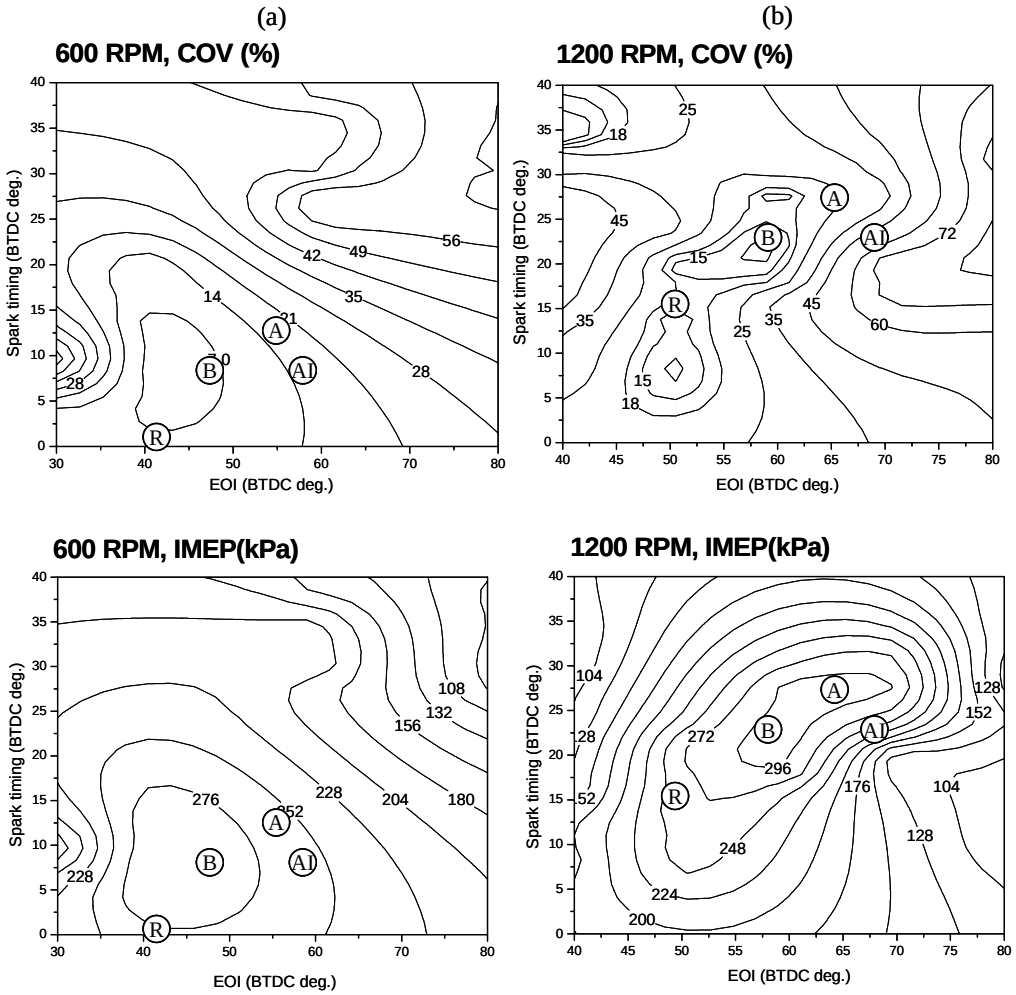

Figure 4.1. Engine map test results illustrating the IMEP and COV as functions of injection timing and spark timing for 600 rpm and 1200 rpm at an equivalence ratio of ϕ=0.3. The locations of the cases in Table 1 are represented by the circle: the Baseline (B), Advanced (A), Advanced Injection (AI), and Retarded (R) cases.

combustion, starting with the fuel distribution at the time of ignition (upper), and showing the flame propagation across the bowl through both the 3-pentanone and the OH LIF images at two later times (lower). The individual images shown were chosen to be

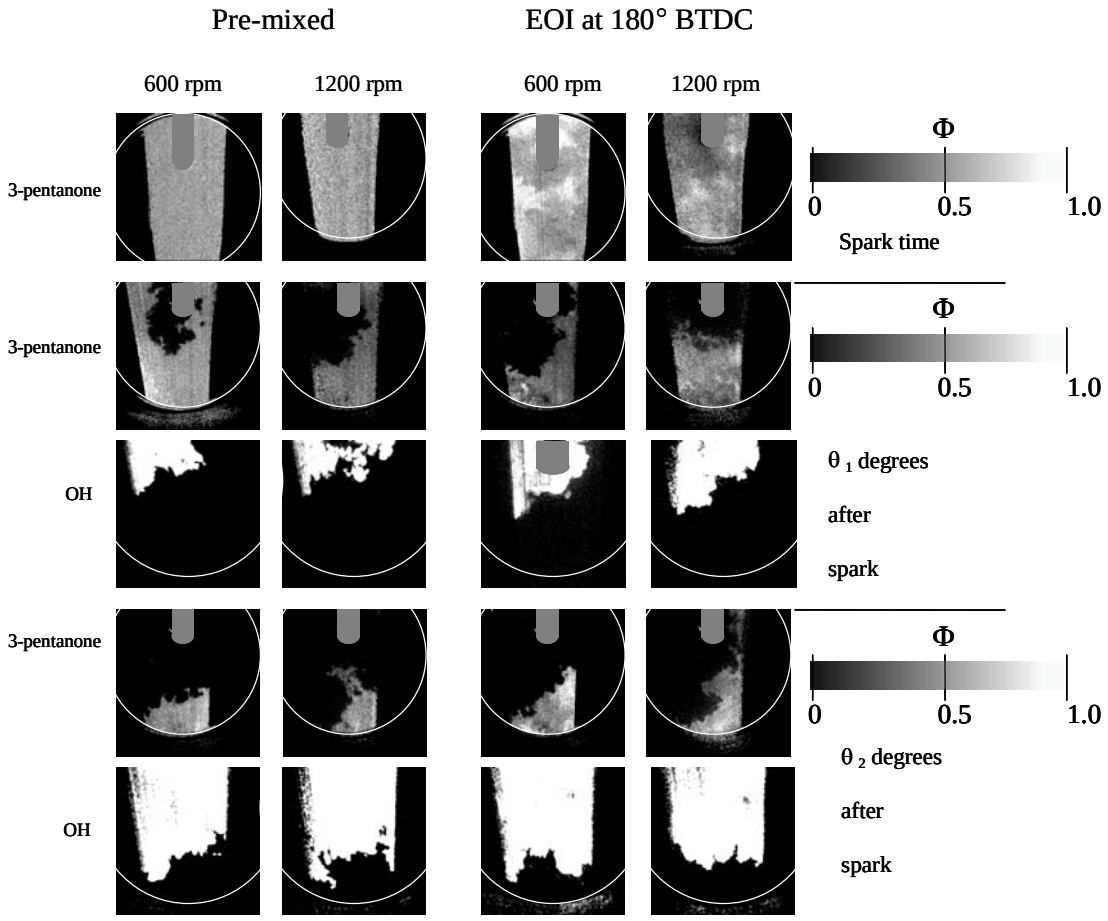

Figure 4.2. Representative single-shot PLIF images for Φ=0.7 operating at 600 rpm and 1200 rpm. θ_1 = 25°, θ_2 = 35°. All images were taken on different engine cycles, within five CA degrees of the reported angle.

representative of the dataset (100 images at each condition). The 3-pentanone images have been calibrated, and the gray scale depicting the equivalence ratio correspondence is shown. No attempt was made to calibrate the OH images, and the contrast was adjusted to best represent the flame front. All of the images were taken on different engine cycles. In addition, slightly different fields of view were used in the images, and the outline of

the piston bowl and shadow from the spark plug are shown in each image for convenience.

The top row of frames shows the fuel distribution at the time of spark. For the premixed system the fuel distribution was completely uniform, as expected. The small-scale variations observed are the result of camera noise. The standard deviation of the spatial equivalence ratio distribution for the premixed case was 15% of the mean signal at 600 rpm and 17%of the mean at 1200 rpm. For the direct-injection case (EOI at 180° BTDC) the fuel was reasonably well mixed, but still showed evidence of large-scale heterogeneity. The standard deviations increased to 21% of the mean signal at 600 rpm and 29% of the mean at 1200 rpm. As demonstrated by the above standard deviations, the extent of heterogeneity was very similar at both 600 rpm and 1200 rpm, reflecting the competing effects of the reduced mixing time available and the increased in-cylinder turbulence at the higher engine speed.

The next two rows of frames show the 3-pentanone and OH fluorescence images shortly after ignition. Large variability in the extent of the combustion zone within the field of view was observed from cycle-to-cycle. The crank angles reported in Figure 3 are averages, and all images were taken within 5 degrees of this value. The fluorescence of 3-pentanone clearly demonstrated the consumption of the fuel as the flame front propagates away from the spark. The OH, however, is an equilibrium product of combustion and thus shows the inverse image of the 3-pentanone. Note the small red-shift of the OH fluorescence often resulted in interference from the spark plug, so the image position and magnification were sometimes adjusted to avoid this effect.

The final two rows show the later stages of combustion, where the flame front had nearly traversed the piston bowl. Again, the position of the flame front is clearly demonstrated in both the OH and 3-pentanone fluorescence signals. As the front sweeps across the bowl and towards the wall, the complete consumption of fuel as it passes can be observed in the 3-pentanone images. OH strongly attenuated the laser sheet, resulting in decreasing signal intensities as the sheet moved toward the top of the image.

The effect of the counter-clockwise swirl was clearly evident in almost all of the images, and is especially pronounced shortly after ignition. Qualitative observation of the flame front as the in-cylinder turbulence increased was consistent with previous studies, which reported an increase in the roughness of the front with engine speed [14,15].

4.3.2 Light load pre-combustion mixture distribution

Figure 4.3 shows individual realizations of the fuel distribution at the time of spark for the four conditions. Due to the protrusion of the spark gap into the bowl at TDC, the laser sheet was located 3 mm above the spark gap, closer to the head. The COV of the Advanced Injection case was an order of magnitude larger than for the other three cases. The reason for this is reflected in the images shown in Figure 4.3. The increased time between EOI and the ignition in the Advanced Injection case allows the fuel cloud to be convected past the spark plug by the counter-clockwise swirl. Additionally, the fuel distribution is seen to be more mixed, which given the lean overall equivalence ratio is not desirable. The Retarded case appeared to have the most ideal

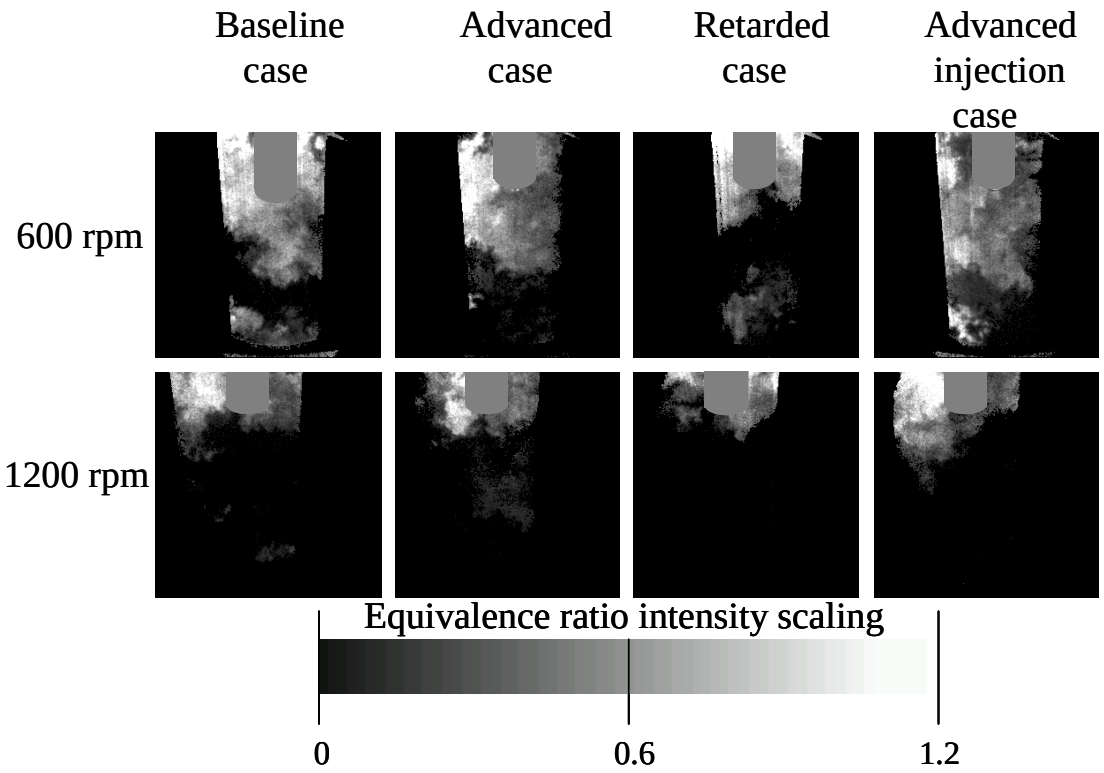

Figure 4.3. Representative 3-pentanone fluorescence images taken at spark time for the cases listed in Table 4.1.

distribution of fuel at the ignition timing, but the late spark time delayed the peak pressure sufficiently so as to reduce the efficiency of the engine. At 600 rpm, the fuel had approximately 11 ms (baseline case) for mixing in the cylinder before the spark event.

At 1200 rpm the time available for mixing in the baseline case is only 5 ms, and based on the data in Figure 4.3 the effects of a decreased mixing time were only partially offset by the increased turbulence intensity associated with the higher engine speed. The

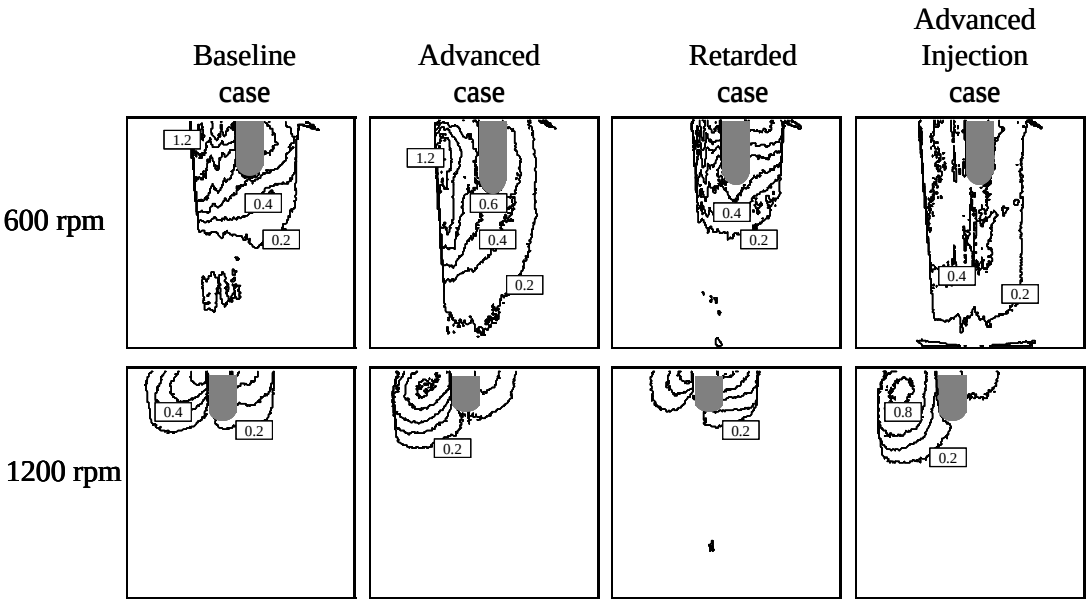

Figure 4.4. Contour plots of equivalence ratios for ϕ=0.3 (a) 600 rpm (top) and (b) 1200 rpm (bottom).

earlier injection timing at 1200 rpm (as compared to 600 rpm) resulted in lower cylinder densities and therefore more rapid penetration of the spray. Even though the spray penetrated more quickly, however, the increased turbulence intensity associated with the higher engine speed was not sufficient to promote mixing to the same extent as observed at 600 rpm. As illustrated in the images, significantly less mixing was observed at 1200 rpm than at 600 rpm. The small size of the fuel cloud is likely a result of the spatial location of the plume (e.g. deeper within the bowl) relative to the laser sheet.

Figure 4.4 shows contour plots of the local equivalence ratio averaged over 100 images for the four cases at 600 rpm (top) and 1200 rpm (bottom). The averaged contours provide more quantitative representations of the previous observations of the

fuel distribution at the time of spark, although the mean image does not represent any particular cycle accurately. At 600 rpm the Baseline, Advanced and Retarded cases, which all combusted repeatably, show regions near the spark plug that approach a stoichiometric mixture. However, the Advanced Injection case had a mean equivalence ratio near the spark plug that was at most $\Phi = 0.6$. Although $\Phi = 0.6$ is within the flamability limits for iso-octane at these pressures and temperatures, the fuel distribution of any particular image can differ significantly from the mean distributions of Figure 4.4 due to the effects of cycle-to-cycle variations in the location and mixedness of the fuel cloud, leading to unreliable ignition. It is important to reiterate that the laser sheet location was 3 mm above the spark gap for these measurements.

At 1200 rpm the extent of the mixture is reduced, but the mean images shown in Figure 6 indicate that near the spark gap for the Baseline, Advanced and Retarded cases the mean mixture was between 0.6 – 1.0 in equivalence ratio. The Advanced Injection case showed that the mean mixture had convected past the spark plug, and was more mixed than the other cases. The combustion in all cases was considered to be consistent with these observations.

4.3.3 Light-load flame structure

Figure 4.5 shows images of OH and 3-pentanone fluorescence obtained during combustion of the baseline cases for both engine speeds. Three imaging times progressing through the combustion event are shown for each speed at the light load condition. Again, the images were all acquired on different cycles so representative

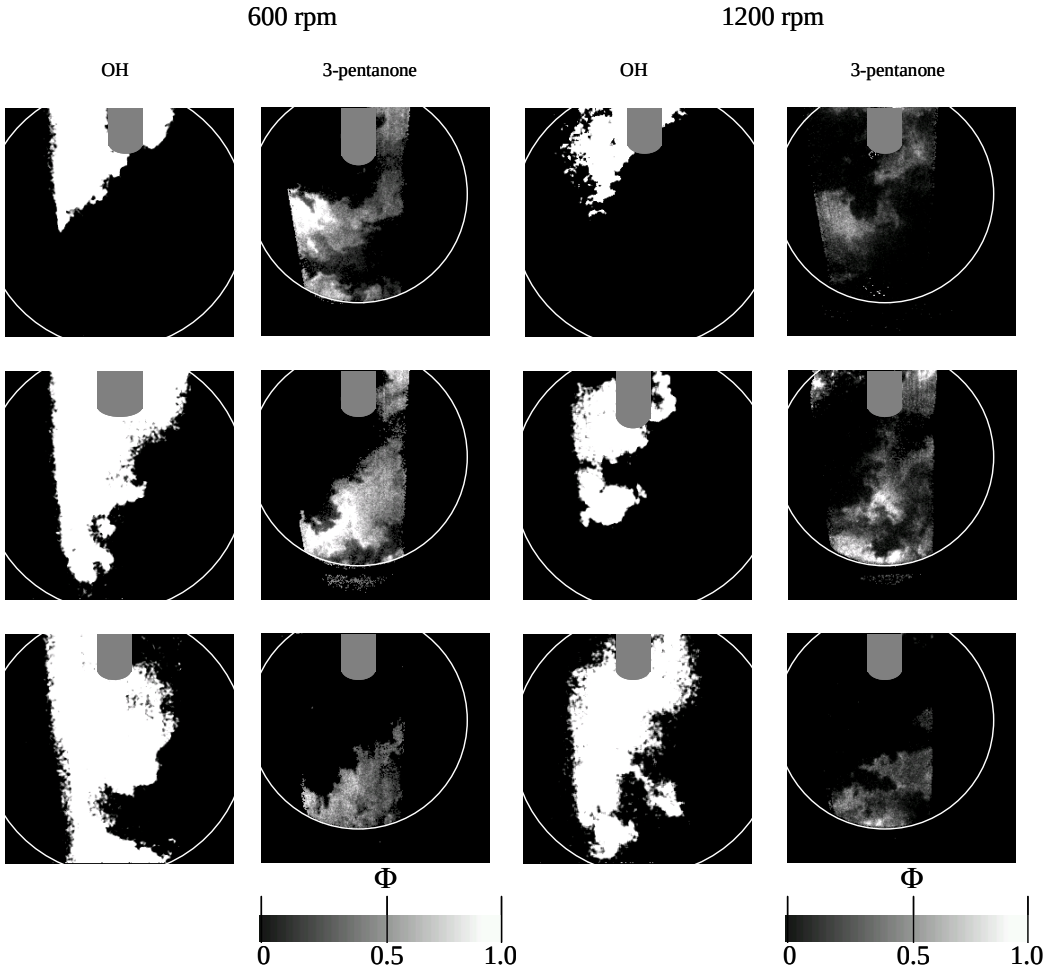

Figure 4.5. Representative single-shot PLIF images for stratified combustion at engine speeds of 600 rpm and 1200 rpm at Φ=0.3. Pictures were taken at 18° after ignition for the top row, 25° after ignition for the second row, and 35° after ignition for the bottom row. All images were taken on different engine cycles.

images are shown at nearly the same flame propagation extent. The OH fluorescence images clearly show the location of the flame front, and extent of combustion. At both speeds, the flame is seen to be convected by the swirl. In the burned gas, the 3-pentanone images are seen to be devoid of signal. However, the fuel distribution at both speeds for this light load is highly stratified and there are significant regions within the field of view for which there is a very low fuel concentration but it is believed that the combustion wave has not reached that point in the chamber. One example of this is the 3-pentanone image at 600 rpm (Figure 4.5, top). At the bottom of the bowl, toward the right side, there is no signal, but based on the OH images, and what appears to be a burned gas region to the left of the spark plug, it does not seem likely that the lack of fuel is the result of combustion. The existence of a 3-pentanone fluorescence signal in the end gas at the end of combustion may be an indication of lean flame quenching. This will be discussed more fully later.

4.4 Discussion

As demonstrated, the PLIF technique provide a powerful diagnostic tool for examining the operation of a DISI engine. The ability to track the location of the flame front, the combustion products, and the local fuel concentrations, is useful not only for optimization of fuel placement and ignition timing but also for investigation of emission related issues. Figures 4.6-4.9 show intensity profiles for data images from several of the running conditions described previously. An intensity profile depicts the spatial variation of the fluorescence signal intensity along a path, and is useful for locating and analyzing the flame front. Profiles are shown for both 3-pentanone and OH images. For the OH

images, quenching of the fluorescence signal and attenuation of the laser sheet prohibit quantification of local concentrations. The 3-pentanone images have been quantified in terms of local equivalence ratios as described in the Experimental Setup section. Figure 4.6 shows the image and profile location depicted with an arrow (left) and the obtained intensity profile along this direction (right) for the premixed high load condition at 600 rpm. The location of the flame front is distinct at about 13 mm from the origin of the profile. The equivalence ratio was between 0.5 and 0.6 at the flame front, increasing rapidly to Φ=0.65 and remaining constant as the fuel region was traversed. Variations from the mean (Φ=0.65) observed in Figure 8 resulted from camera noise. The mean value of Φ=0.65 was slightly lower than the expected value of Φ=0.7. This is an effect of the residual gas. Because the calibration flatfield image was obtained under motoring conditions, the residual gases of the flatfield contained more fuel than during the combusting data images, leading to an underestimate of the equivalence ratio. In Figure 4.7, the intensity profile for direct injection with EOI at 180 BTDC for the high load

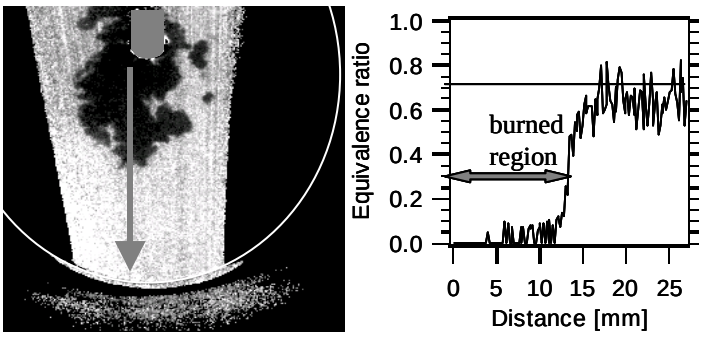

Figure 4.6. 3-pentanone intensity profile for premixed injection (Φ=0.7), 15 degrees after spark, operating at 1200 rpm.

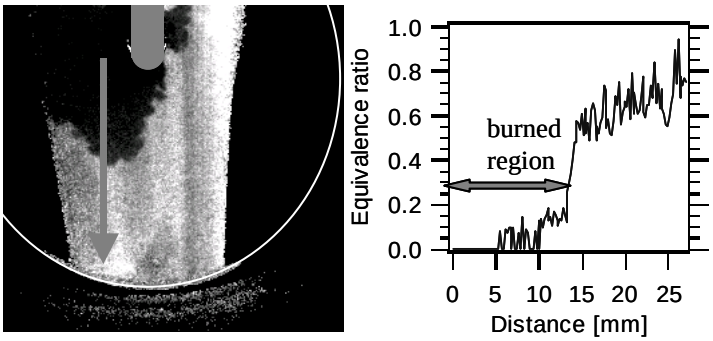

Figure 4.7. 3-pentanone intensity profile for direct injection (Φ=0.7), EOI at 180° BTDC, 15 degrees after spark, operating at 1200 rpm.

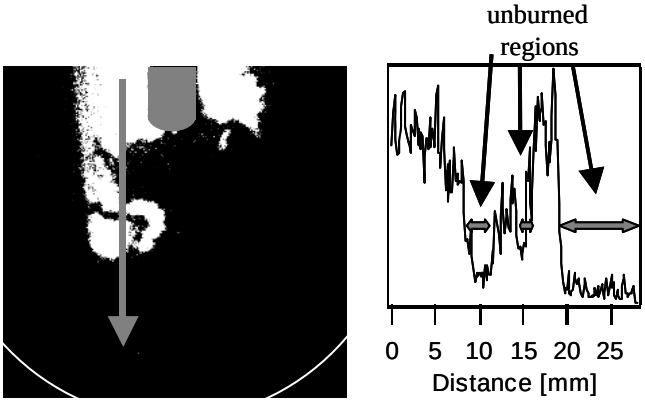

Figure 4.8. OH intensity profile for sratified combustion (Φ=0.3), 20 degrees after spark, operating at 1200 rpm.

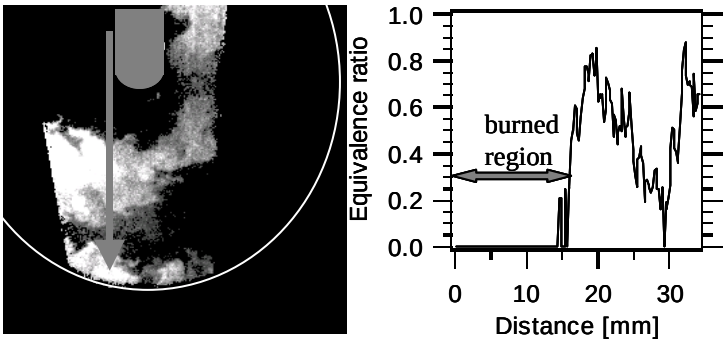

Figure 4.9. 3-pentanone intensity profile for stratified combustion (Φ=0.3) of the baseline case in Table 1, image taken 20 degrees after spark, operating at 600 rpm.

condition and 600 rpm is shown, and can be compared directly with Figure 4.6. The effects of a heterogeneous fuel distribution are clearly seen. Again, a well defined flame front can be observed at 14 mm from the profile origin, burning at an equivalence ratio of about 0.5. As the fuel cloud was traversed, however, the equivalence ratio did not reach a constant value, but slowly increased to about Φ=0.8 near the edge of the bowl. Large scale heterogeneity was commonly observed under these injection conditions, although steep gradients in the equivalence ratio were not present.

Figure 4.8 shows the profile location for an OH image (left) obtained at the premixed high load condition for 1200. The corresponding intensity profile is shown at the right. The laser sheet entered the cylinder at the bottom of the image. Along the line of the profile, the sheet first crossed the flame front at 19 mm, with subsequent traversals at about 16, 14, 12, and 8 mm from the origin of the profile. Local OH concentrations were not directly proportion to the collected fluorescence signals for the reason previously described. The intensity axis (y-axis) is therefore unlabeled, and the (OH) images and profiles are used for location of the flame front and for visualizing the distribution of burned gases during combustion.

In Figure 4.9, the fuel concentration near the flame front under light load conditions is examined, for the baseline case at 600 rpm (Table 4.1). The flame front was crossed at about 16 mm from the profile origin, and the equivalence ratio at the front was about Φ=0.6. This equivalence ratio at the flame front is comparable with the values observed at the high load case where the overall equivalence ratio was more than twice that at the light load. Within 15 mm, the equivalence ratio increases to a nearly

stoichiometric value and then falls back to nearly undetectable fuel concentrations (Φ = 0.05 to 0.1), indicating the presence of steep gradients in fuel concentration. The very low equivalence ratios at 29 mm from the profile origin are not an indication of combustion in this region. This area was commonly very lean (see Figure 4.5), due to the interaction between the generated swirl and the wall of the piston bowl, convecting the fuel around the edge of the bowl and leaving a lean region at the center of the vortex.

In order to investigate the extent and influence of cycle-to-cycle variations in the fuel distribution at the spark time near the spark gap, a statistical analysis of 100 data images acquired for each of the eight conditions in Table 2 has been performed. The local equivalence ratios were examined in two rectangular regions (5.4 × 8.6 mm at 600 rpm, and 5.4 × 5.4 mm at 1200 rpm) located immediately upstream (to the right) and downstream (to the left) of the spark plug as shown in Figure 4.10. Slightly different box

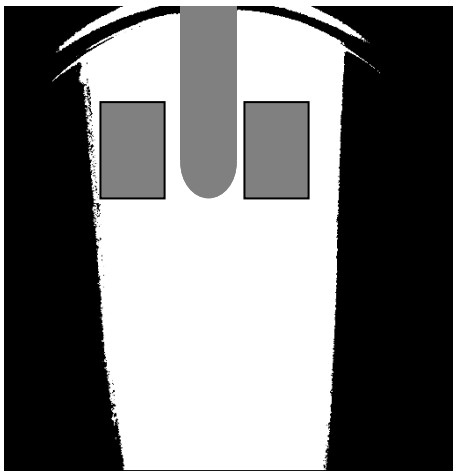

Figure 4.10. Location of the test boxes for the statistical analysis of the fuel distribution.

sizes were used at the two engine speed due to variations in the mean size and location of the fuel cloud between 600 rpm and 1200 rpm. For each data image, the average equivalence ratio and standard deviation were calculated within each of the two boxes.

Histograms of the average equivalence ratio within the test regions for 100 data images are shown in Figure 4.11, where the solid line represents the downstream (left) box and the dashed line represents the upstream (right) box. In general, the upstream box demonstrated lower average equivalence ratios than the downstream box (except for the Retarded case). This result can be explained simply by the general flow pattern. The injector is directed toward the right at the lower edge of the field of view, and the piston bowl redirects the flow in the counter-clockwise direction. Thus, the stratified fuel cloud convects past the spark plug from right to left. At the spark time for which the images were acquired, the main cloud has passed the spark gap and the trailing edge, with a leaner equivalence ratio, is present at the upstream location whereas the downstream location is still within the main portion of the fuel cloud. In many cases the mixture upstream of the spark plug appears too lean to ignite, however ignition was achieved. It is likely that a significant component of vertical flow, resulting from the re-entrant piston bowl design, convected fuel from below the plane of the laser sheet into the spark region. Also, as previously mentioned, the laser sheet was positioned approximately 3 mm above the spark gap due to geometric constraints imposed by protrusion of the spark plug into the piston bowl. Further relations between the fuel distribution and combustion performance will be discussed later.

Both the extent of cycle-to-cycle variability and its dependance on engine speed can be observed from Figure 4.11. Large fluctuations in equivalence ratio were evident

at both engine speeds, although the variability was about twice as large at 1200 rpm. Standard deviations of the average equivalence ratio calculated based on the phase-averaged mean were about twice as large at 1200 rpm as at 600 rpm, as can be observed by the width of the distributions in Figure 4.11.

Figure 4.12 shows histograms of the (spatial) standard deviations calculated within each box for each data image with the upstream box again represented by the dashed line. Overall, the standard deviations were quite large, indicating the presence of significant gradients inequivalence ratio within the boxes. These results agree with the qualitative observations from Figure 4.3. Steeper gradients and higher standard deviations were observed at 600 rpm than at 1200 rpm. The steepest gradients and highest standard deviations were observed in the downstream box for the Retarded injetion case at 600 rpm. The lowest standard deviations were observed in the upstream box at 1200 rpm for all except the Retarded injection case, because the fuel distributions were generally very lean and did not exibit steep gradients.

The equivalence ratio statistics from the stratified cases above, as well as from the high load ($\Phi = 0.7$) cases were compared to engine pressure data for the same cycle as the image, allowing a direct comparison of the observed fuel distribution to the performance of the engine. The high load, premixed condition provided a homogeneous fuel distribution at the time of ignition, with intensity variations attributable to camera noise alone. The images with EOI at 180° BTDC showed a small level of stratification as expected at this injection case since the time allowed for mixing to occur is short (relative

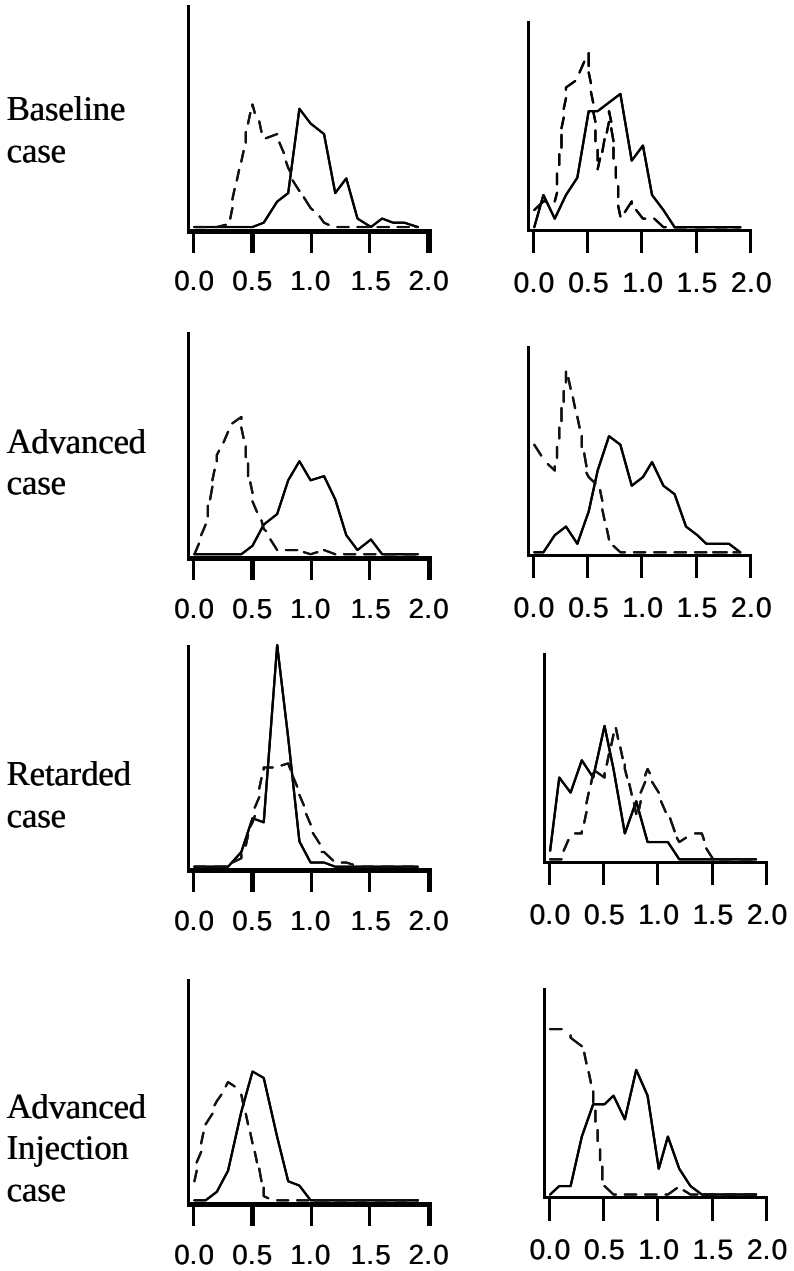

Figure 4.11. Histograms of box averages. Solid line = downstream box, dashed line = upstream box, for 600 rpm (left) and 1200 rpm (right).

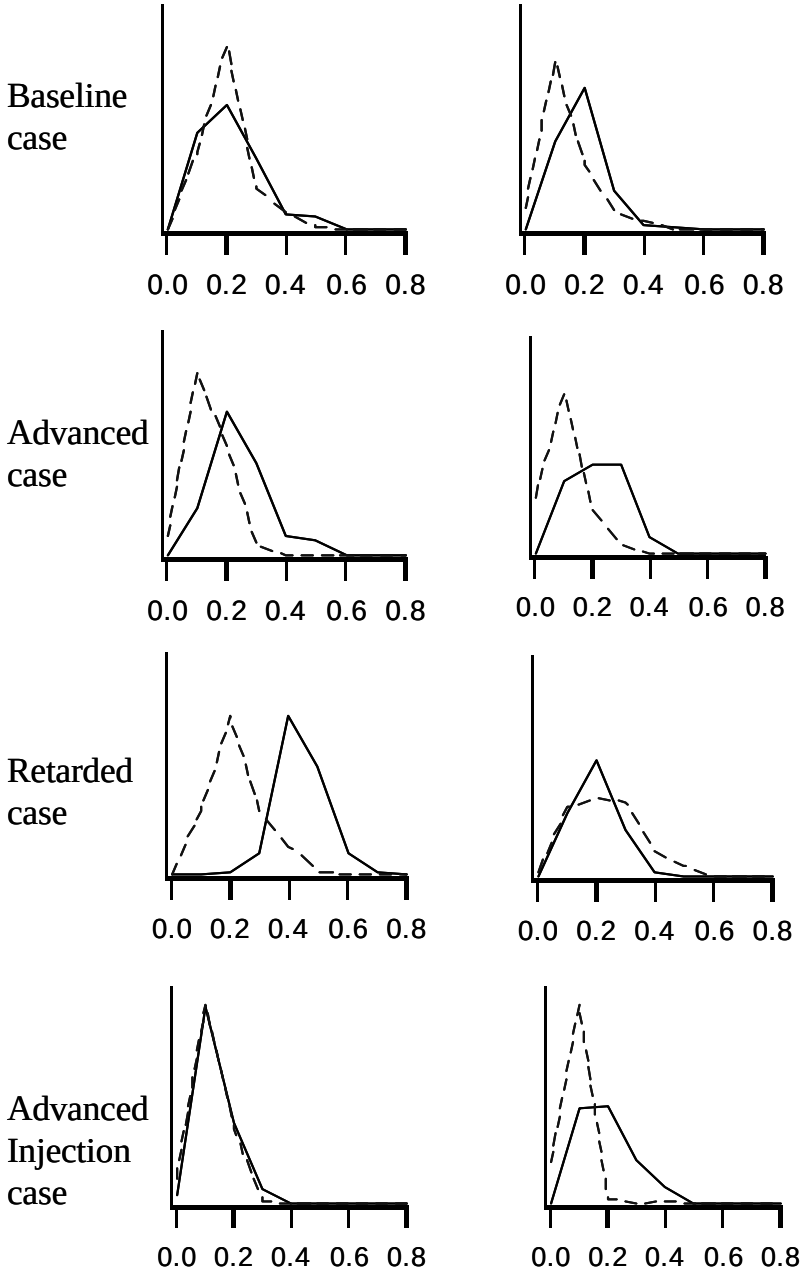

Figure 4.12. Histograms of box standard deviations. Solid line = downstream box, dashed line = upstream box, for 600 rpm (left) and 1200 rpm (right).

to a typical homogeneous DISI operating condition), and the cylinder flowfield is relatively quiescent as compared to intake stroke injection timings.

The slight stratification of the fuel increased the cycle-to-cycle variability of the combustion. The COV of IMEP for the premixed case ranged from 2-5%, whereas the COV of IMEP for the 180° EOI was between 21-27%. Although the cycle-to-cycle variability increased in the 180° EOI case, on average the mixture ignited significantly faster than the premixed condition. In order to investigate whether the more rapid ignition was the result of the local stratification near the spark gap, a direct cycle-by-cycle comparison was performed between the box statistics described above and the cylinder pressure. Figure 4.13 shows the delay, from spark time, for a 0.7 bar pressure rise above the motored pressure versus the average equivalence ratio within the boxes identified in Figure 4.10. The choice of 0.7 bar was chosen to be above noise level fluctuations in the cylinder pressure prior to combustion. Results were not sensitive to the specific value, provided that it was high enough to assure that combustion had commenced. Both the left and right boxes show a very slight correlation between the pressure rise delay and the average box intensity for the particular cycle. The weak correlation is, in part, believed to be the result of the laser sheet being on a slightly different plane than the spark gap, although other factors are also considered to be important as discussed below. Interestingly, the correlation for the upstream and downstream locations is qualitatively very similar. Also marked in the plots is the region that represents the range of the premixed data (±2 standard deviations along both the equivalence ratio axis and the delay axis). Clearly, the cycle-to-cycle variability in both

quantities was lower in the premixed case, although the pressure rise delay is significantly longer.

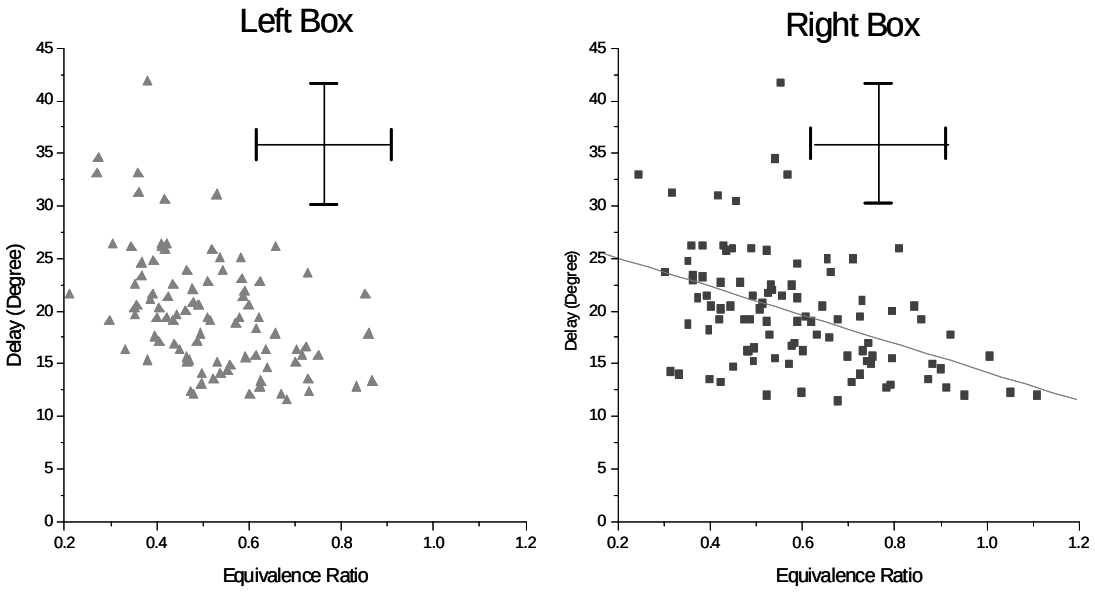

Figure 4.13. Comparison of crank angle delay between ignition and 0.7 bar cylinder pressure against the average equivalence ratio within the box for Φ=0.7, EOI at 180° BTDC. The inset in the Right Box plot indicates the region where the premixed combustion occurred.

For the stratified injection conditions of Table 4.1, significantly less correlation was observed between the local equivalence ratio near the spark plug and engine combustion data. The IMEP, peak pressure, location of peak pressure and the pressure rise delay were compared to the fuel distribution statistics for the same engine cycle with no discernable correlation. The lack of correlation under the stratified condition suggests the importance of the cylinder flow on the injection event as has been seen before [1]. There are vastly differing time scales between the PLIF event, which takes place in less

than 10 ns, and the ignition event, which takes place during the ~1 ms spark discharge. A flow with a moderate velocity of 5 m/s will convect 5 mm in the time of the spark discharge. Thus, the conditions at, or near the spark gap as determined by a PLIF image may not correspond to the mixture that is present at the spark gap during the actual ignition event, defined as the development of a self-sustaining flame kernel.

4.5 Conclusions

PLIF methods provide a powerful diagnostic tool for investigating combustion in a DISI engine. Hydroxyl radical (OH) images showing the location of burned gas, and 3-pentanone images showing the location of unburned fuel were presented for several operating conditions. The calibration method described provides quantification of local equivalence ratios both before and during combustion from the 3-pentanone fluorescence images. High load conditions with an equivalence ratio of $\Phi = 0.7$ using premixed and early (EOI at 180 degrees BTDC) injection conditions were investigated. For early direct injection significant heterogeneity of the fuel distribution was observed, as compared to the premixed case. The effects of this heterogeneity on engine performance were reflected in the increase of the COV of IMEP from about 4% in the premixed case to 25% for direct injection. However, there was only a slight correlation between the fuel concentration near the spark gap at the time of ignition and the ignition delay (as

measured by the time to achieve a 0.7 bar pressure rise). No significant differences were observed between the two engine speeds.

Stratified operating conditions for an overall equivalence ratio of 0.3 were examined at both 600 and 1200 rpm. Several conditions were examined at each engine speed to investigate the effects of varying the injection timing, ignition timing, and the dwell between the two events on the distribution of fuel at the spark gap location at the time of ignition. In all cases no correlation was observed between the fuel distribution at the ignition time and metrics associated with the combustion performance. The cause for this behavior is believed to be mixture motion on the timescale of the spark discharge, which is considerably longer than the time scale associated with the LIF image. Detailed investigation of the 3-pentanone and OH images during the combustion showed, for the first time under such conditions, that the combustion was occurring in a highly stratified mixture. Further, the equivalence ratio near the flame front were between 0.5 and 0.8 in the engine at the optimized combustion conditions. The impact of this off-stoichiometric combustion in the overall lean mixture has profound implications on the formation of pollutants. Finally, images obtained during the expansion stroke long after the major heat release show the presence of 3-pentanone in the end gas, suggesting that lean flame quenching is being directly observed.

5 Bulk quenching of the flame

5.1 Introduction

This chapter presents PLIF results that demonstrate the occurrence of bulk flame quenching during light-load, stratified operation of a DISI engine. Although flame quenching is often cited as a possible hydrocarbon emission mechanism and several studies have used indirect methods (such as exhaust gas sampling under controlled conditions and computational methods) to argue that quenching occurs (see Sections 2.1.5 and 2.1.6), the results presented here represent the first direct observation and measurement of the quenching phenomena. As mentioned in Section 1.2, the goals of this study are largely qualitative, to observe the presence (or absence) of bulk quenching, to observe and understand the influence of engine operating conditions (EOI, Φ, ignition time) and in-cylinder conditions (temperature, pressure) on the quenching process, and finally to attempt to quantify the equivalence ratio of the unburned fuel.

5.2 Conditions

The light load operating conditions used to examine bulk flame quenching utilized an equivalence ratio of Φ = 0.3 (corresponding to a load of 130 kPa IMEP). As described in Chapter 4, such operation yields a highly stratified fuel cloud in an excellent spatial location for observation of the late stages of combustion relative to the field of view. A baseline running condition of EOI at 48° BTDC and ignition at 15° BTDC was

used. Other conditions were examined and will be discussed in the appropriate sections of this chapter. For all cases, the engine was operated at 600 rpm.

Observation of bulk flame quenching requires obtaining PLIF images after the main heat release event, well after top dead center and into the expansion stroke. This introduces several difficulties into the PLIF imaging as well as the interpretation and quantification of these images. Two examples of these difficulties are the low 3-pentanone number densities due to expansion of the cylinder gases, which leads to problems measuring small equivalence ratios, and the presence of significant flame luminosity, which complicates the interpretation of the PLIF images.

The flame luminosity is thought to result from pool fires on the piston top. These pool fires are caused by the impingement of the spray on the piston. Figure 5.1 shows observations of the flame luminosity over a wide range of crank angles. The left column shows 3-pentanone fluorescence images (with luminosity) captured at the indicated CA. Immediately after these images were taken, the laser was turned off and another series of images was captured. These images are shown in the right column. Since there is no laser-induced fluorescence, Figure 5.1b shows only the flame luminosity.

The flame luminosity signals were generally of much higher intensities than the 3-pentanone fluorescence. The spatial location of the luminosity was also constrained to specific areas, which conveniently were generally separated from the location of 3-pentanone and often outside of the area illuminated by the laser sheet. These factors, combined with the insight gained from examining hundreds of images such as those in Figure 5.1, allowed for identification and/or removal of flame luminosity. It should be

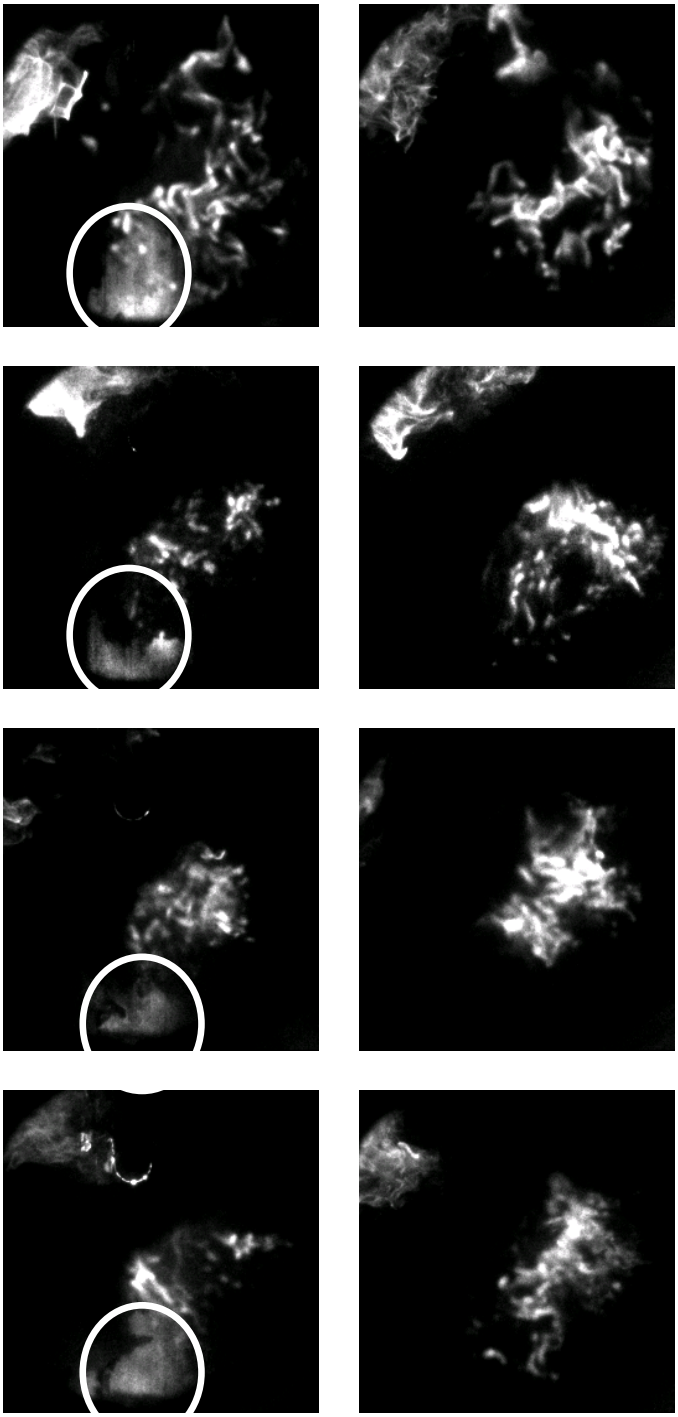

Figure 5.1. Images of flame luminosity at various crank angles. 3-pentanone fluorescence shown in solid circles, flame luminosity is uncircled. At left, Images obtained with laser operating, showing both 3-pentanone fluorescence and flame luminosity, at right, images obtained without the laser operating, showing only flame luminosity.

mentioned that in some images this distinction could not be made with certainty, but the data sets were sufficiently large that good examples were abundant.

5.3 Bulk flame quenching

5.3.1 Bulk flame quenching – Existence

The mean pressure trace for the baseline running condition of EOI at 48° BTDC and ignition at 15° BTDC is shown in Figure 5.2a. Figure 5.2b shows the log(P) vs log(V) plot. Indicated on Figure 5.2b are the times for start of injection, end of injection, ignition, and the picture timing. The approximate time of the quenching event (about 10° ATDC to 20° ATDC), and arguably the end of the main heat release event, is indicated by the shaded gray band (Figure 5.2b).

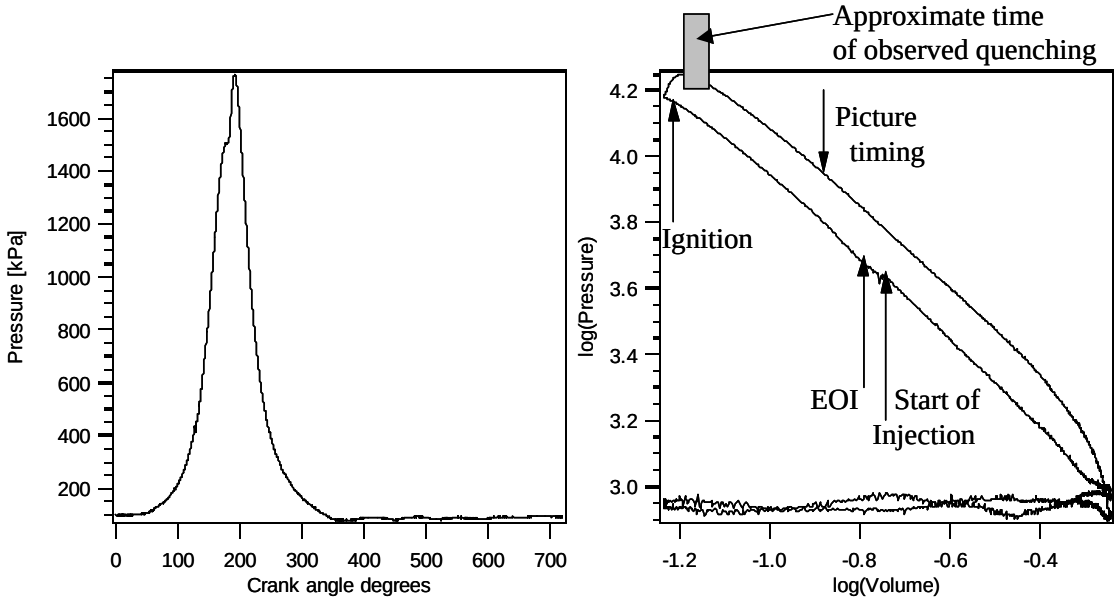

Figure 5.2. Left, mean experimental pressure trace of the baseline operating condition EOI at 48° BTDC and ignition at 15° BTDC. Right, log(P) vs log(v) plot of the same pressure data.

PLIF images of 3-pentanone and OH at the baseline running condition are shown in Figure 5.3 and 5.4 respectively. Figure 5.4 shows four OH fluorescence images captured at progressively increasing crank angles. Between ignition time (15° BTDC) and about 5° ATDC, combustion proceeded as the flame front traversed the fuel cloud and moved across the piston bowl. This is demonstrated in the advance of the OH signal front between Figures 5.4a and 5.4b, demarcating the progress of the flame. By the time of Figure 5.4c (10° ATDC), however, the progression of the flame front had essentially ceased. At 15° ATDC (Figure 5.4d) the flame front remained in essentially the same position as Figure 5.4c, and the OH signal near the spark plug showed visible signs of degradation.

Degradation of the OH fluorescence signal was caused by both attenuation of the laser sheet and decreasing gas densities during the expansion stroke. OH is expected to be present in the highest concentrations near the location of the spark plug as an equilibrium product of combustion. Since combustion is initiated at the spark plug, the fuel in this area reacts early, and the resulting product zone is compressed by the expanding gases associated with the surrounding combustion. Attenuation of the laser sheet by OH caused a reduction of the fluorescence signal as the product zone was traversed (by the laser sheet) toward the spark plug, causing reduced signals toward the top of the OH images (see Figure 3.4, bottom, for example).

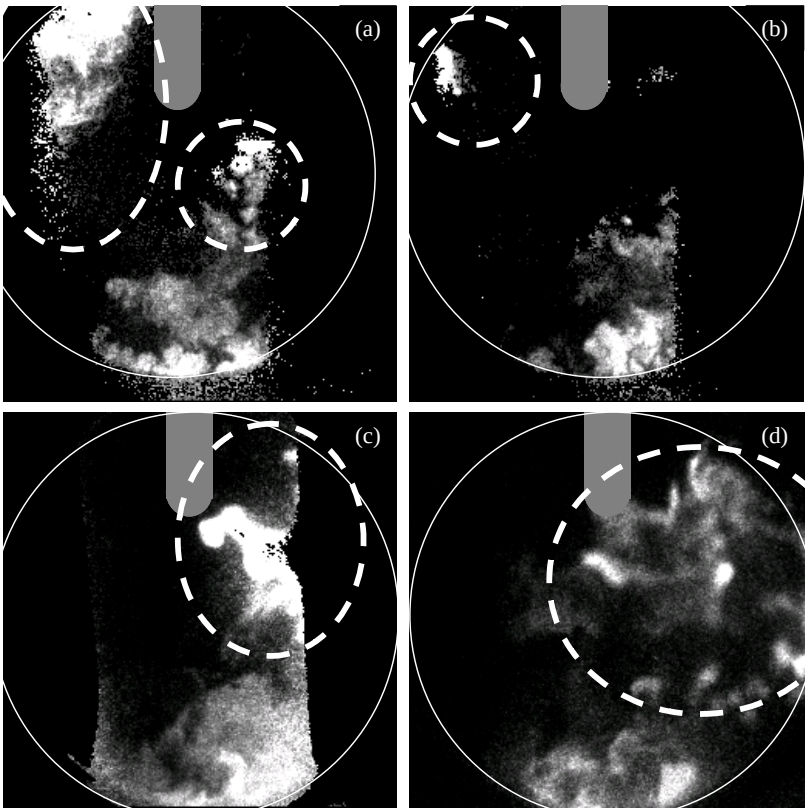

Figure 5.3. 3-pentanone images at various crank angles for P_{in} = 14.3 psi, operating at 600 rpm and Φ=0.3, EOI at 48° BTDC, ignition at 15° BTDC. (a) Picure at 5° ATDC, (b) Picure at 10° ATDC, , (c) Picure at 40° ATDC, (d) Picure at 60° ATDC.

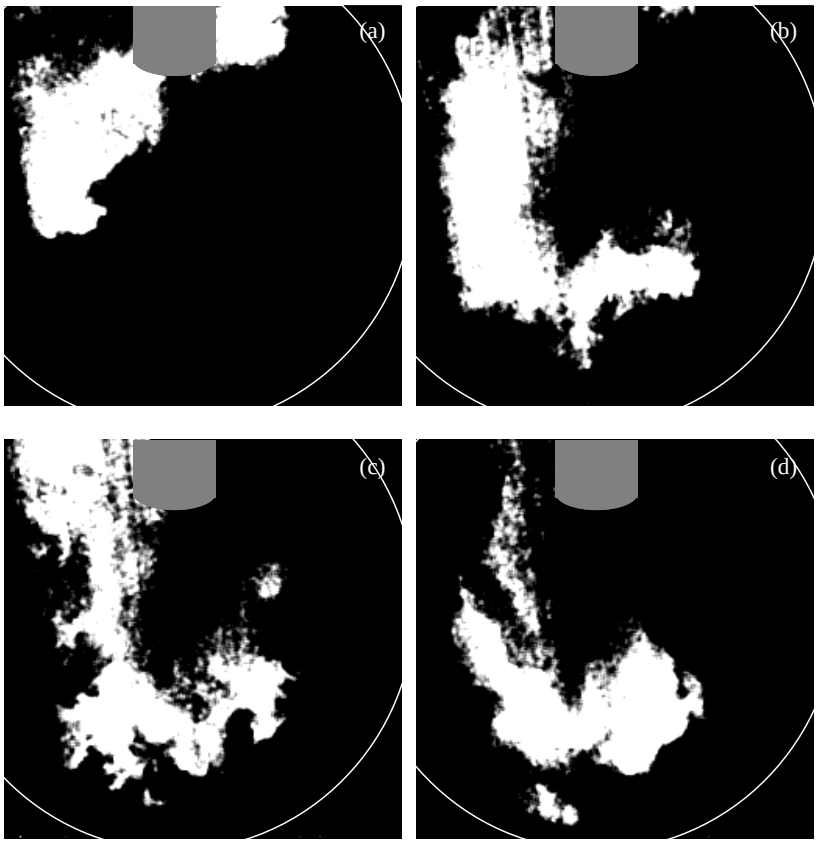

Figure 5.4. OH images at various crank angles for P_{in} = 14.3 psi, operating at 600 rpm and Φ=0.3, EOI at 48° BTDC, ignition at 15° BTDC. (a) Picure at 5° BTDC, (b) Picure at 5° ATDC, (c) Picure at 10° ATDC, (d) Picure at 15° ATDC.

It is important to recall that all images were taken on different engine cycles, and that each image presented was chosen as representative of the data set from which it was taken. It was clear from the data sets of the images from Figure 5.4 that the flame front advanced until about 5° ATDC to 10° ATDC and then stalled before reaching the edge of the piston bowl.

Similar observations can be derived from the 3-pentanone images of Figure 5.3. Between 5° ATDC (Figure 5.3a) and 10° ATDC (Figure 5.3b) the propagation of the flame front slowed and very little fuel consumption was observed. After 10° ATDC, no further consumption of the fuel was observed. The fuel at the bottom of the images in Figure 5.3a and 5.3b continued to mix with gases in the cylinder. No further oxidation was observed, and the unburned fuel periphery was imaged well into the expansion stoke until reduced cylinder pressures and increased mixing led to fluorescence signals too weak to detect with a suitable signal to noise ratio.

Figure 5.3c was taken at 40° ATDC, clearly after the flame propagation and associated heat release had ended. The image correction procedure of Section 3.4 was applied to Figures 5.3 a,b, and c. Flame luminosity within the area of the laser sheet was not removed in the correction and is shown in the dashed white circles. The fluorescence signal outside the circles is due to unburned 3-pentanone. Figure 5.3d was not corrected, which is why flame luminosity outside of the laser sheet was not removed. The very late picture timing (60° ATDC) resulted in very low image intensities. This led to problems differentiating between the fluorescence signal and the background noise in the image

correction code. The flame luminosity is shown in Figure 5.3d in the white circle, and 3-pentanone can still be observed at the bottom of the laser sheet.

Figure 5.5 (right) shows a single 3-pentanone fluorescence image taken at 40° ATDC for the operating conditions on Figure 5.3. The flame luminosity is enclosed in the dashed circle, and the remaining fluorescence signal indicates the presence of unburned fuel. Also shown in Figure 5.5 is the location of an intensity profile. The intensity profile is shown at the right of Figure 5.5. Traversing the quenched fuel cloud in the horizontal direction shown by the arrow, the equivalence ratio of the unburned fuel varied between 0.2 and 0.4

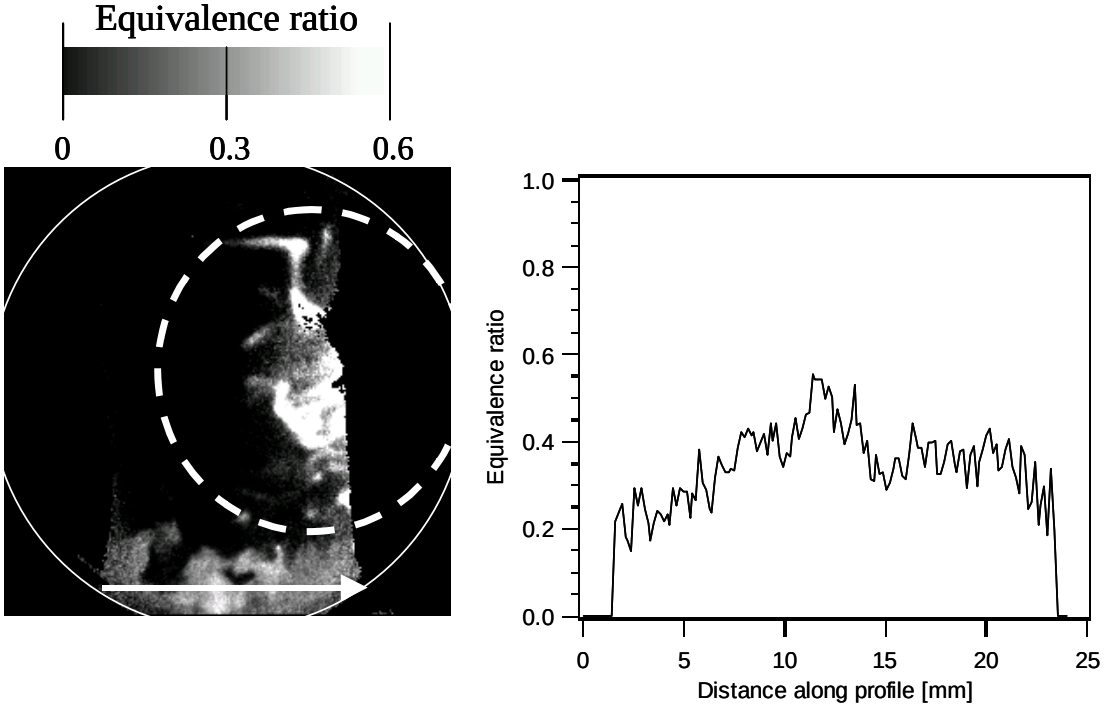

Figure 5.5. 3-pentanone fluorescence showing the unburned fuel region after the quenching event. The image was taken at 40° ATDC. The solid white circle shows the outline of the piston bowl. The signal in the dashed white circle is flame luminosity that was not removed in the correction process. The arrow indicates the location of the intensity profile shown at left. The equivalence ratio of the unburned periphery is between 0.2 and 0.4.

It is clear from these images that bulk quenching of the fuel cloud occurs and can contribute to unburned hydrocarbon emissions. For the baseline light-load operating condition examined, the flame front was observed to progress across the imaging area and then stop, as demonstrated by both OH (Figure 5.4) and 3-pentanone (Figure 5.3) images. This occurred at about 5° ATDC to 10° ATDC. The unburned fuel beyond the extent of the flame progression was observed up to crank angles of 60° ATDC, well into the expansion stroke and long after any post-combustion oxidation would be possible.

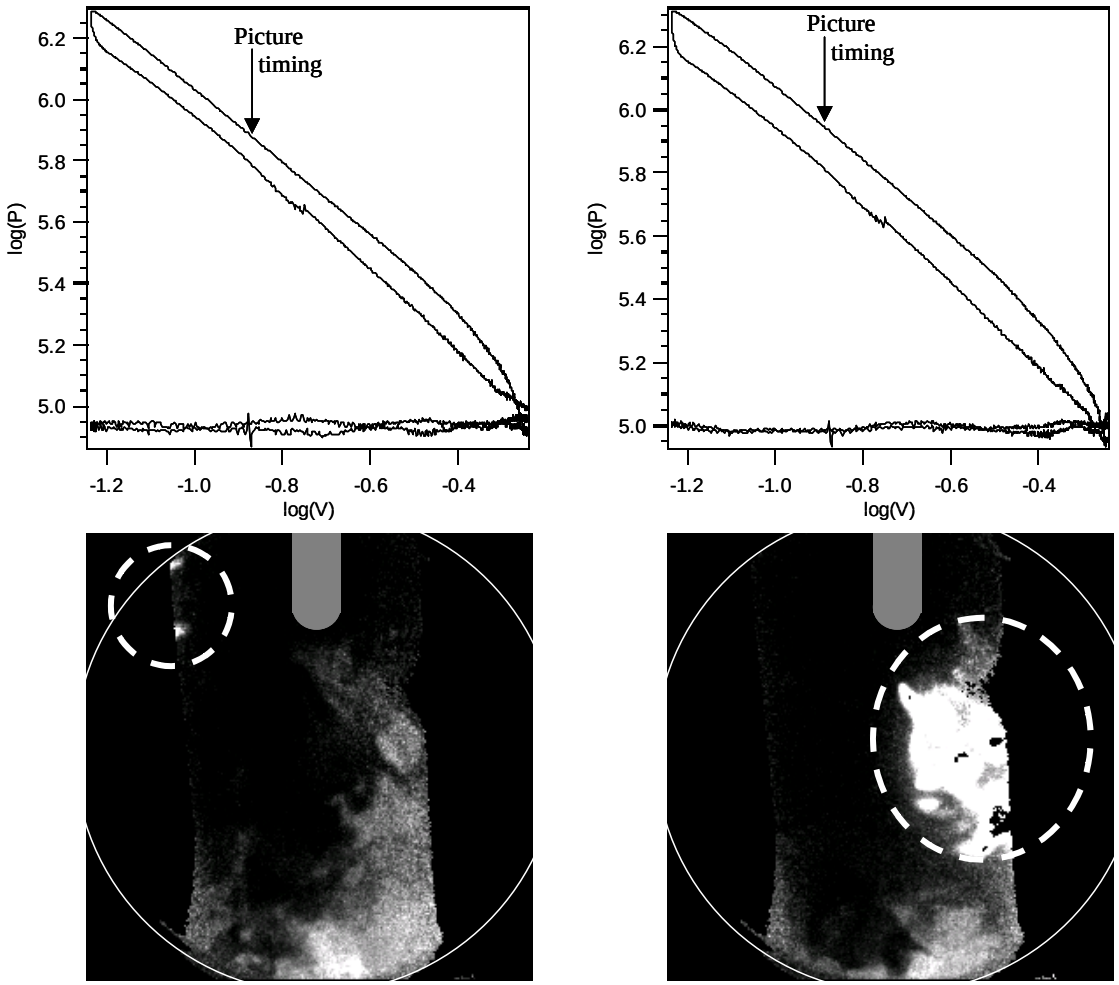

Figure 5.6. Log(P)-log(V) plots and the associated images showing the unburned fuel. The picture timing (40° ATDC) is shown by the line across the expansion stroke.

Figure 5.6 shows two images of the unburned fuel periphery at 40° ATDC (bottom row) and the log(P) – log(V) plot of the measured cylinder pressure for the same engine cycle as the image was taken (top row). The picture timing is indicated by the line across the expansion stroke. Clearly, by this time the heat release event has ended. The left image shows a much larger region of trapped fuel and very little flame luminosity in the area of the laser sheet, while the right image demonstrates a much smaller region of fuel near the wall of the piston bowl. It is interesting to note that this is reflected in the pressure data for the two cycles. It could be argued that, due to the increased amount of trapped fuel in the left image, the work output of that cycle is significantly smaller than the cycle of the right image, as indicated by the reduction of the enclosed area in the pressure curve. In general, however, one must be careful in drawing general conclusions about the influence of the amount of observed fuel since the 2-dimensional imaging area is not necessarily representative of the 3-dimensional distribution.

5.3.2 Bulk flame quenching – Effect of combustion phasing

Having demonstrated the existence of bulk flame quenching, experiments have also been performed to determine whether quenching can be alleviated by altering the in-cylinder conditions. In particular, these experiments were designed to promote an increased temperature of the end gas. The method investigated in this section is to advance the combustion phasing. Advancing the combustion event within a limited window of acceptable operation increases the peak pressure and leads to increased end gas compression and thus temperature. In addition to the baseline condition (EOI at 48°

BTDC and ignition at 15° BTDC), the following three conditions were examined: EOI at 60° BTDC and ignition at 20° BTDC, EOI at 48° BTDC and ignition at 20° BTDC , and EOI at 48° BTDC and ignition at 25° BTDC. The results for these conditions are shown in Figure 5.7. Even though the EOI and ignition times were varied, all of the images were taken at 25° ATDC, well after the main heat release event in all four cases. There was unburned fuel observed at this late time in all four cases.

In the 60° ATDC EOI case (Figure 5.7a), both the injection and ignition times were advanced relative to the baseline, and the mixing time of the fuel was increased by 7 crank angle degrees (1.94 ms). The fuel was overly mixed, and large amounts of unburned fuel were consistently observed. The other three cases were very similar in terms of the amount of unburned fuel observed in the PLIF images. All three had the same injection timing (EOI at 48° BTDC). The baseline case used an ignition time of 15° BTDC. The ignition times of the other two cases were progressively advanced to 20° BTDC and 25° BTDC, respectively. This was done in an attempt to increase the cylinder pressures and temperatures by moving the peak pressure location toward top dead center. For the baseline case, the mean maximum cylinder pressure was 1.82 MPa, which occurred at 4.9° ATDC. For ignition at 20° BTDC, the pressure increased to 2.02 MPa at 2.04° ATDC, and for ignition at 25° BTDC the maximum pressure was 2.29 MPa at 1.97° ATDC.

The images for these three cases (baseline, 20° ignition, 25° ignition) are shown in Figure 5.7 b, c, and d. The amount of remaining fuel observed for these three cases was on average about the same. The variation in the amounts of fuel in the figures

resulted from cycle-to-cycle variations. The amount of flame luminosity increased significantly as the spark timing was advanced. This was caused by richer combustion leading to higher soot production, since the fuel had less time to mix as the spark was advanced. Although the peak pressures and temperatures were advanced toward top dead center and increased, it was insufficient to alleviate quenching. Unburned fuel was observed for all cases examined within a window of acceptable combustion.

5.3.3 Bulk flame quenching – Effect of intake throttling

An alternative method of increasing the temperature of the end gas is by reducing the intake manifold pressure while maintaining a constant mass of injected fuel. Figure 5.8 shows images obtained at 10° ATDC (just after the approximate time quenching was typically observed) for four different air intake pressures, 69 kPa (10 psi), 83 kPa (12 psi), 99 kPa (14.3 psi), and110 kPa (16 psi). Adjusting the air intake pressure while maintaining a constant injected mass of fuel influenced the light-load operation in several ways. Lower air intake pressures resulted in lower gas densities in the cylinder at the time of injection, which led to more rapid penetration and mixing of the fuel spray. Also, since the fuel mass was held constant, the overall equivalence ratio increased as P_{intake} was reduced. At P_{intake} = 69 kPa the overall equivalence ratio was $\Phi = 0.47$, while at P_{intake} = 110 kPa, the overall equivalence ratio was $\Phi = 0.24$. Lower air intake pressures also increased the maximum combustion temperatures achieved by decreasing the amount of diluent (air that did not react with the fuel). In addition, at lower intake manifold pressures, the hot residual gases represent a larger percent mass fraction of the

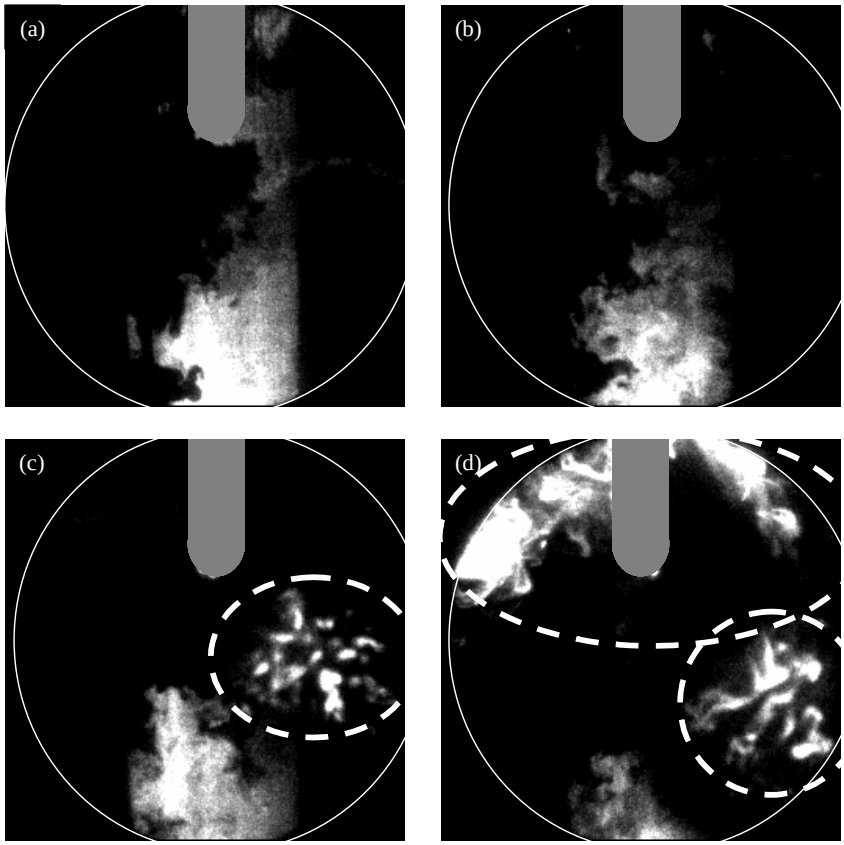

Figure 5.7. Effect of varying injection conditions on lean quenching operating at 600 rpm and Φ=0.3. All images were taken at 25° ATDC. (a) end of injection (EOI) at 60° BTDC, ignition at 20° BTDC, (b) EOI at 48° BTDC, ignition at 15° BTDC, (c) EOI at 48° BTDC, ignition at 20° BTDC, (d) EOI at 48° BTDC, ignition at 25° BTDC.

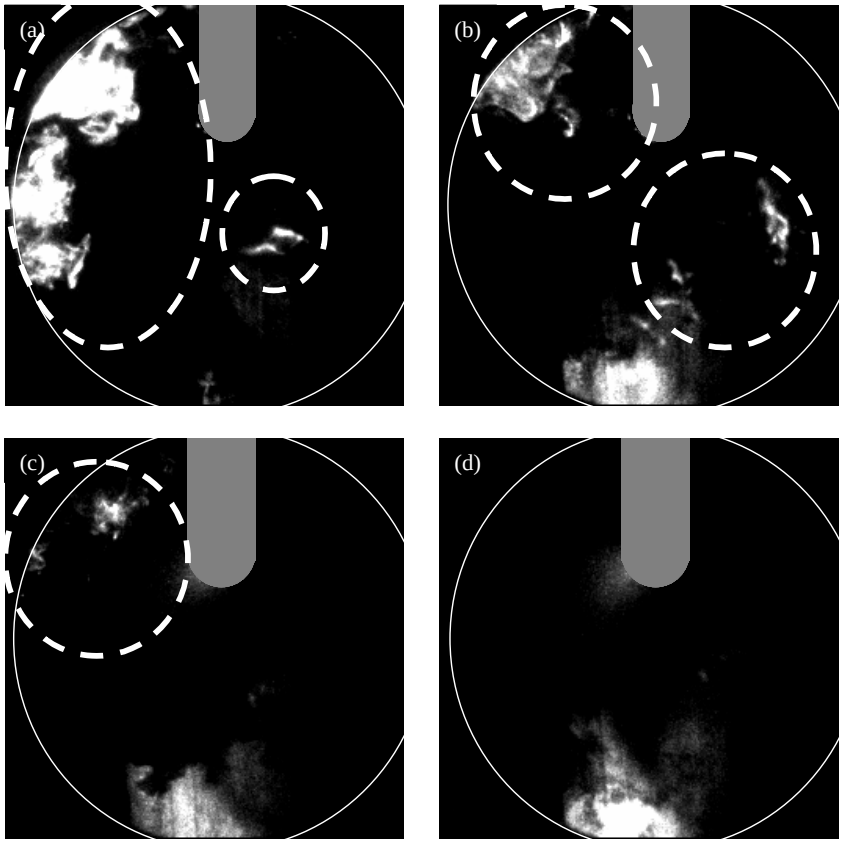

Figure 5.8. Effect of varying intake pressure, P_{in}, on lean quenching, operating at 600 rpm and Φ=0.3, EOI at 48° BTDC, ignition at 15° BTDC. All images were taken at 10° ATDC. (a) P_{in}=69 kPa, (b) P_{in}=83 kPa, (c) P_{in}= 99 kPa, (d) P_{in}= 110 kPa.

total cylinder contents than for higher intake pressures, thus causing higher temperatures. The combination of these effects led to increased cylinder temperatures, increased mixing of the fuel cloud, and higher overall equivalence ratios, with a decrease in the air intake pressure (i.e. throttling the engine).

Quenching of the flame in the lean periphery of the fuel cloud was observed for air intake pressures of 83 kPa and higher, as shown in Figure 5.8 b, c, and d. At P_{intake} = 69 kPa, however, quenching was not observed and the fuel was completely oxidized (Figure 5.8d), at least on the plane of the laser sheet. Of the above-mentioned effects of reducing P_{intake}, it is the increase in temperature in the cylinder that is expected to most significantly influence the flame quenching process. Although the overall equivalence ratio was increased, the mass of fuel and therefore the total energy released during combustion remained essentially unchanged. It was therefore expected that the IMEP of the four cases would be close to the same value. Measured values, however, were 96.6 kPa, 118 kPa, 160 kPa, and 154 kPa for the intake manifold pressures of 110 kPa, 99 kPa, 83 kPa, and 69 kPa respectively.

There are several possible factors that likely contributed to this. First, blowby of cylinder gases past the piston rings was observed, which led to increasing loss of mass with increasing intake manifold pressure. This was unlikely to have resulted in sufficient mass loss to affect the IMEPs to the extent observed. Another possible contributor is the quenching event, which reduces the IMEP by reducing the amount of reacting fuel. Again, this is unlikely to have produced the observed changes in IMEP, since alleviation of quenching was not observed until the intake pressure was reduced to 69 kPa and the mass of unburned fuel alone does not seem sufficient to produce such large changes in

the work output. A more likely explanation is that at the throttled case, the combustion was more efficient due to variations in the fuel distribution and the cylinder conditions (temperature and pressure).

Figures 5.9 and 5.10 show the progression of combustion for the baseline condition at an air intake pressure of 69 kPa via 3-pentanone and OH fluorescence images, respectively. In Figure 5.9, 3-pentanone fluorescence images are shown at 5° BTDC (Figure 5.9a), 5° ATDC (Figure 5.9b), 10° ATDC (Figure 5.9c), and 25° ATDC (Figure 5.9d). Up until about 5° ATDC, the flame front propagates away from the spark plug location, consuming the fuel as it moves. At about 5° ATDC, the flame front reached the lean periphery of the fuel cloud. By 10° ATDC, however, no fuel was observed within the field of view. Images were obtained up to 60° ATDC and fluorescence of 3-pentanone was not seen.

A similar description of the combustion process is reflected in the OH images of Figure 5.10, captured at crank angles of 5° BTDC, 0° BTDC, 7° ATDC, and 20° ATDC. Initiation of the flame kernel was generally slow, often showing little progression at 5° BTDC. By 7° ATDC, however, the flame front had traversed the field of view and reached the edge of the piston bowl. The apparent continued combustion in Figure 5.10d is the result of cycle-to-cycle variations in the location of the OH region (all images were taken on different engine cycles). Very little formation of OH was observed between 7° ATDC and 20° ATDC, and it was determined that by 7° ATDC the front had reached the edge of the bowl and all of the fuel had been burned.

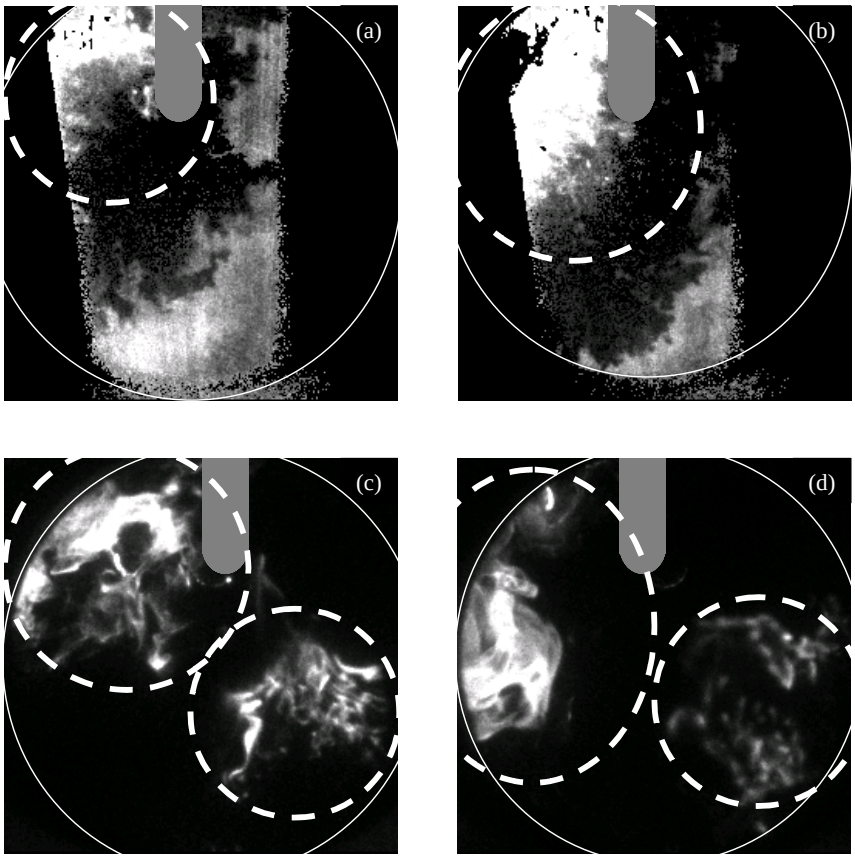

Figure 5.9. 3-pentanone images at various crank angles for P_{in} = 10 psi, operating at 600 rpm and Φ=0.3, EOI at 48° BTDC, ignition at 15° BTDC. (a) Picure at 5° BTDC, (b) Picure at 5° ATDC, , (c) Picure at 10° ATDC, (d) Picure at 25° ATDC.

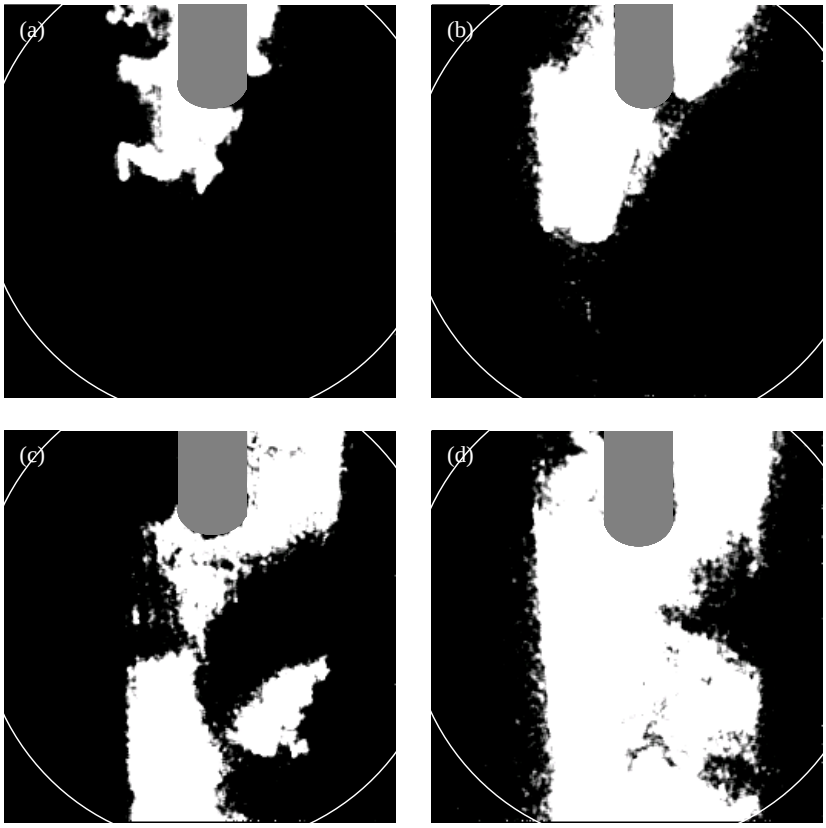

Figure 5.10. OH images at various crank angles for P_{in} = 10 psi, operating at 600 rpm and Φ=0.3, EOI at 48° BTDC, ignition at 15° BTDC. (a) Picure at 5° BTDC, (b) Picure at top dead center, (c) Picure at 7° ATDC, (d) Picure at 20° ATDC.

Due to cycle-to-cycle variations in the extent of combustion and an inability to obtain a progression of images from a single engine cycle, it could not be determined whether the flame front quenched at the lean periphery of the fuel cloud and post-combustion oxidation consumed the remaining fuel, or whether the flame burned all the way to the wall, consuming all of the fuel without post-combustion oxidation. This will be discussed in greater detail in Section 5.4.

5.4 Discussion

As previously mentioned, the primary question posed by the results is what are the mechanisms by which quenching was alleviated when the air intake pressure was reduced to 69 kPa. The two most likely of these are an increase in the end gas temperature, or an increase in the homogeneity of the fuel cloud, which allows the flame front to burn to the wall and consume all of the fuel. An increase in the temperature of the end gas can influence the quenching event in several ways. At sufficiently high end gas temperatures, the unburned hydrocarbon periphery could undergo secondary oxidation, thus consuming all remaining fuel and alleviating quenching. Also, an increase in the peak temperature (and pressure) leads to a reduction of the lean flammability limit of the fuel, thereby allowing a given mixture to burn more completely before quenching occurs. The combination of increased homogeneity of the fuel cloud and decreased lean flammability limit is likely to be the cause for alleviation of quenching when peak temperatures are insufficient to induce secondary oxidation.

A lower estimate of the end gas temperatures can be obtained by assuming a polytropic compression of the end gas. Using the experimental log(P) – log(V) diagram

for atmospheric and 69 kPa intake pressures, the polytropic exponent was assessed based on the pre-injection period of the compression stroke, and was k = 1.326 for the 99 kPa case and 1.333 for the 69 kPa case. The temperature was estimated using

$$\frac{T_0}{T} = \left(\frac{P_0}{P}\right)^{k-1/k} \qquad (5.1)$$

where T_0 and P_0 are the bottom dead center temperatures and pressures and k is the polytropic exponent. The value of T_0 was assumed to be the coolant temperature, 80° C. The pressures P and P_0 were obtained from the measured pressure history, and using Equation 5.1 provided an approximate history of the end gas temperature. Figure 5.11 shows the estimated end gas temperature as a function of crank angle for both the atmospheric and 69 kPa air intake pressure cases. The peak temperature was 707 K for the atmospheric case and 775 K for the 69 kPa case. Although the temperature was elevated at the lower air intake pressure, it was not sufficiently large to induce secondary oxidation of the unburned fuel periphery. As mentioned, this is a lower estimate of the temperature of the end gas, since the bottom dead center temperature ($T_0 \approx$ coolant temperature) does not include the residual effect. The residual gases constitute nearly 10% of the mass in the cylinder and cause an increase in T_0. These hot residual gases result in a higher uniform mixture temperature at bottom dead center as the residual gases and fuel and air equilibrate. In addition, the percent mass of the residual gases to the total

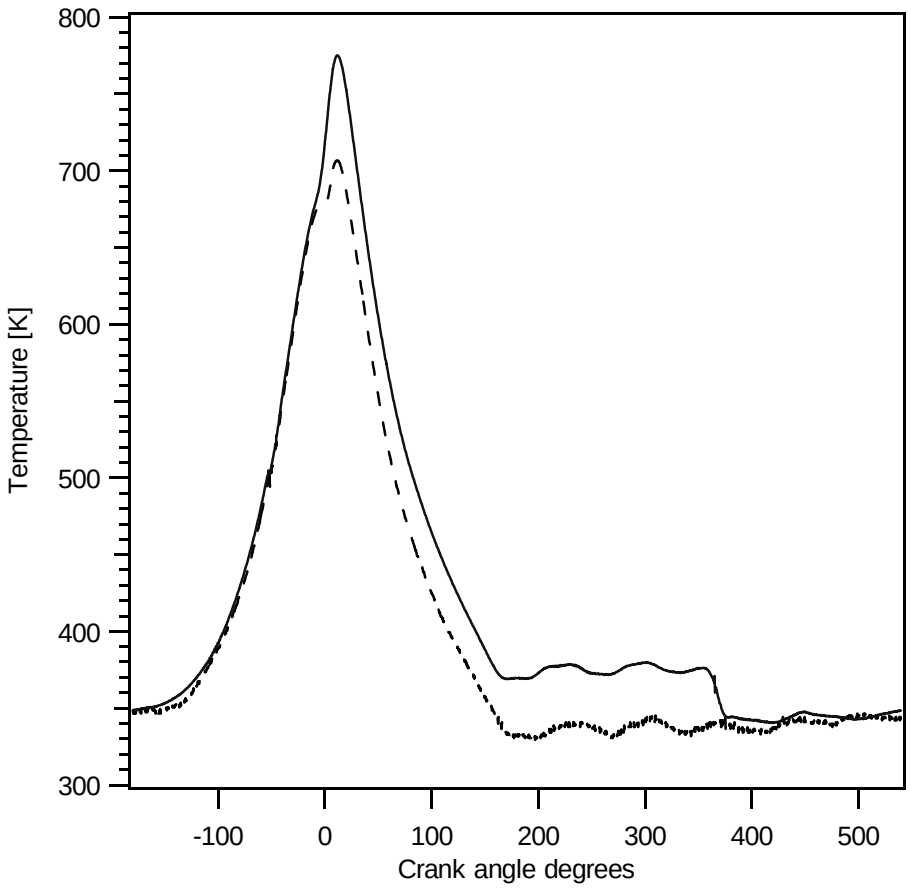

Figure 5.11. Temperature history calculated assuming isentropic compression using the experimentally obtained pressure trace for intake pressures of 99 kPa (dashed) and 69 kPa (solid).

cylinder gases increases with decreasing intake manifold pressure, thus leading to even higher temperatures in the throttled cases.

5.5 Conclusions

This chapter has demonstrated the existence of bulk flame quenching in the lean periphery of a stratified fuel cloud under light-load operation of a DISI engine. OH fluorescence was used to monitor the growth of the product region and the advance of the

flame front, while 3-pentanone fluorescence demarcated the remaining fuel as well as the progression of the flame front.

Images were taken for a baseline operating condition of EOI at 48° BTDC and ignition at 15° BTDC using an atmospheric intake manifold pressure. These images show the flame front progress across the piston bowl and then stop, leaving a region of unburned fuel. This unburned fuel remained visible very late into the expansion stroke (70° ATDC), long after the heat release event. Conclusions about the total mass of unburned fuel could not be drawn, since the 2-dimensional imaging area is not necessarily representative of the 3-dimensional distribution in the cylinder.

Quantification of the local equivalence ratios of the post-quench fuel region shows that the unburned periphery had an equivalence ratio of $\Phi \approx 0.3$. Adjusting combustion parameters (ignition timing, injection timing) within a window of acceptable combustion was not sufficient to alleviate quenching. When the air intake was throttled to 69 kPa while maintaining a constant mass of injected fuel, quenching was not observed. This is likely influenced both by increased homogeneity of the fuel cloud as well as increased end gas temperatures, which extend the lean flammability limit. Based on the end gas temperature estimates, post-oxidation is not considered to be important.

It is important to mention that the results presented here were performed on an optically accessible DISI engine and do not necessarily relate directly to actual DISI engines. Specifically, no claims are made as to the extent of quenching or its contribution to total unburned hydrocarbon emissions. The primary goal of these experiments was to provide direct experimental observation of the bulk flame quenching

event, which has long been cited in the literature as an important source of hydrocarbon emissions but until now had not been directly observed.

6 Conclusions

This study has used planar laser-induced fluorescence of 3-pentanone doped into the fuel and OH present in the combustion products to examine combustion in an optically accessible DISI engine. A method was presented that allowed calculation of the local equivalence ratios from the intensity of the 3-pentanone fluorescence. In addition, 3-pentanone fluorescence was used to visualize the consumption of fuel and the progression of the flame front. Fluorescence of OH provided an independent observation of the progression of the flame front. The image collection process and quantification method were evaluated by examining the flame structure and fuel distribution for several homogeneous and stratified operating conditions (Chapter 4).

Experiments of the high load case (Section 4.3.1) compared premixed operation to EOI at 180° BTDC and found that the heterogeneity (spatial rms value) of the fuel cloud was 6% at 600 rpm and 11% at 1200 rpm greater for direct-injection operation as compared to the premixed case. No correlation was observed between the equivalence ratio near the spark plug and the time required for a 70 kPa pressure rise. The expected reason for this lack of correlation is the vastly differing time scales between the LIF event and the ignition event.

Flame structure and fuel distribution visualization experiments of light load operation (Section 4.3.2) have provided for the first time measurement of the local equivalence ratio of the stratified fuel cloud during combustion. At the time of ignition, the stratified fuel cloud consisted of a relatively rich core of equivalence ratio Φ = 1.0 – 1.4 grading into a lean periphery at the edge of the cloud. After ignition, the flame front swept quickly through the richer core, reaching the lean periphery about 20° to 25° after

ignition. Equivalence ratios close to the advancing flame front decreased from $\Phi = 1.0 – 1.4$ in the core to $\Phi = 0.4 – 0.6$ as the front approached the lean periphery.

The visualization of bulk flame quenching (Chapter 5) under stratified operating conditions represents the first direct experimental observation of the bulk flame quenching phenomena. Observation of the flame front at progressively later crank angles using both OH and 3-pentanone fluorescence showed the front sweep across the piston bowl (consuming fuel and producing OH), reaching the lean periphery of the fuel cloud at about 5° ATDC (for the baseline operating condition of Chapter 5). Further progression of the flame front was not observed beyond about 10° ATDC. The OH signal began to degrade due to decreasing number densities, but did not expand any further. The 3-pentanone fluorescence images showed a region of unburned fuel that was observed as late as 70° ATDC, long after the end of heat release. The equivalence ratio of the unburned periphery was $\Phi \approx 0.3$ at the maximum, grading to zero away from the region of fuel. Advancing the combustion to increase the end gas temperatures by moving the peak pressure toward top dead center was not sufficient to alleviate quenching. When the intake manifold pressure was reduced to 69 kPa quenching was alleviated, at least on the plane of the laser sheet.

Based upon the results of this study, the following recommendations are made to guide subsequent investigation of bulk flame quenching in DISI engines. A key question that should be thoroughly reviewed is: What is the mechanism by which quenching was

alleviated when the engine was throttled to 69 kPa? To this end, continued PLIF experiments should be pursued to study the effects of throttling the engine on the fuel distribution. Also, a more complete understanding of the influence of throttling on important combustion parameters such as the end gas temperature, pressure, IMEP, COV of IMEP, and the rate of the early flame kernel growth (i.e. time from ignition to a given pressure rise). The effects of varying the air intake temperature should also be examined.

Future work is also recommended to determine the mass of unburned fuel in the lean (quenched) periphery and the contribution of quenching to total hydrocarbon emissions. It will also be important to assess the relative contribution of quenching to hydrocarbon emissions in going from an optically accessible DISI engine to an actual DISI engine.

Appendix A Fractal concepts

A.1 Introduction

This appendix describes a fractal-based approach to characterizing and describing the structure of the flame front. Due to limitations in maximum attainable speed on the experimental DISI engine used in this study, a thorough examination of the relationship between the fractal parameters and the turbulence intensity could not be performed. The limited results obtained, however, provide significant insight into a current debate in combustion literature and thus warrant documentation.

The organization of this appendix is as follows. First, the necessary background in fractal geometry will be developed, followed by a survey of literature on the subject. Several methods, and the differences between them, for calculating the fractal dimension D will be discussed. Following validation of the utilized method for calculating D, results of flame structure analysis are presented and discussed.

A.2 Background

A.2.1 Fractal fundamentals

Fractal concepts are suitable for describing several aspects of turbulent flows. Many researchers have illustrated the fractal character of scalar isosurfaces and premixed flame fronts under turbulent conditions. Although it is widely accepted that the premixed turbulent flame front is a fractal within the appropriate inner and outer cutoff lengths, there is recent debate in the literature as to whether there is a relationship between the

fractal dimension D and u'/S_l (the turbulent intensity divided by the laminar flame speed). Early studies ([15] [58]) indicate that the fractal dimension D_2 increases from 1.2 to 1.37 as u'/S_l is increased. Recent studies ([59] [60]) however, do not observe such a relationship, and report a fractal dimension of about $D_2 = 1.2$ for all cases of turbulent intensity examined. To explain this discrepancy, Gulder *et al*. [59] propose that the difference lies in the method of calculating the fractal dimension.

We take the time now to define what a fractal is, and what is meant by a fractal dimension. For an arbitrary object O define the set $\mathbf{A} = \{ \mathbf{x} : \mathbf{x} \in O \}$ as the set of all points which the object occupies, where $\mathbf{x} \in \Re^n$. If the object has volume, then $n = 3$ and if it is a curve in a plane $n = 2$, where n is the Euclidian dimension in which the object is embedded. Another important dimension in describing the set A is the topological dimension D_{top}. The topological dimension of a curve is one, and D_{top} of a surface is two. For standard Euclidian objects, the dimension of the object equals D_{top}. Mandelbrot, 1983 [61] defines a fractal as an object for which the Hausdorff-Besicovitch (HB) dimension exceeds the topological dimension, although he is careful not to equate the HB dimension to the fractal dimension. Before quantifying the fractal dimension, it is helpful to qualitatively examine the concept. Working with the definition of Mandelbrot and the above discussion, we see that the fractal dimension D satisfies

$$D_{top} < D < D_{emb} \qquad (1)$$

so for a fractal 'curve' $1 < D_2 < 2$, and for a fractal 'surface' $2 < D_3 < 3$. In order to avoid confusion, D refers to a general fractal dimension, and D_2 and D_3 as indicated to a 'curve' or 'surface' respectively. Other fractal dimensions introduced will receive a subscript. In

general, the fractal dimension is not an integer. In a physical sense, this can be described as follows. The measured size of a fractal object depends upon the scale of resolution over which that measurement is made. An example illustrates this point well.

Consider the problem of measuring the length of a coastline such as that of Norway shown in Figure A.1. Let one measure this length (on a very calm day) by letting many 'walkers' of various stride length carefully walk the coast and count the number of steps taken. It would be found at the finish line that the measured length of the coastline depends upon the stride length of the walker. Very small stride lengths lead to a very large measurement for the length of the coast, and a plot of all walkers would show that the relationship is exponential, so that in the limit of very small strides the length of the coast goes toward infinity.

There are two dimensions commonly referred to as the fractal dimensions of an object. These are the Hausdorff-Besicovitch (HB) dimension D_H and the similarity dimension D_S, and they are defined as follows. In the ideal case, the similarity dimension is given by

$$D_S = \lim_{\varepsilon \to 0} \frac{\log N(\varepsilon, A)}{\log(\frac{1}{\varepsilon})} \qquad (2)$$

where N is the number of coverings of size ε required to cover the object. More realistically, there is often either an inner cutoff length below which the object is no longer fractal or a minimum scale of observation. Many physical systems also exhibit an upper cutoff length. It is helpful to rearrange (2) as

$$\log(N) \propto D_s \log(1/\varepsilon) \qquad (3)$$

or

$$N \propto (1/\varepsilon)\text{^}D_s \quad (4)$$

Defining the normalized length, *S*, of a fractal curve as $S = N\varepsilon$ we get

$$S \propto \varepsilon\text{^}(1-D_s) \quad (5)$$

The fractal dimension D_s can be obtained by determining the slope of the log-log plot of either *S* or *N* against ε. Shepherd *et al*., 1992 [57] suggest that log(*S*) vs. log(ε) provides clearer results. Measurement of D_s will be described in greater detail presently.

The HB dimension D_H is more difficult to define. Begin by defining the quantity

$$H_\delta^S(A) = \inf\{\sum_{i=1}^{\infty} |U_i|^s : \{U_i\} \in \{\delta - \mathrm{cover}(A)\}\} \quad (6)$$

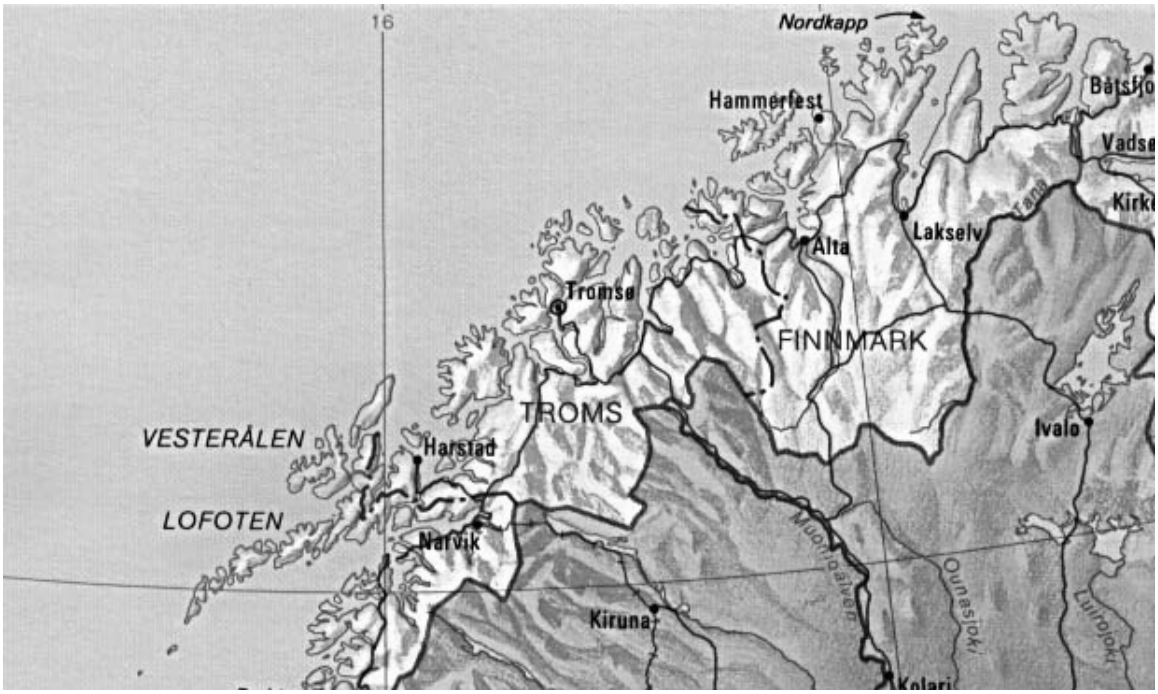

Figure A.1. Map of the northern coast of Norway. Notice the roughness of the coastline, making an estimate of its length difficult.

The infimum (inf) of a set is the largest number which is smaller than all values in the set. Essentially we want to minimize the sum of the s^{th} powers of every δ-cover of **A**. A δ-cover of a set is a collection of balls of radius less than or equal to δ that completely covers the set. Each set {*U*i} is a δ-cover of the fractal set **A**. We take δ < 1 so that H_δ^S decreases with increasing *s*. The *s*-dimensional Hausdorff measure of a set is

$$H^S(A) = \lim_{\delta \to 0} H_\delta^S(A) \qquad (7)$$

In taking the limit, $H^S(A)$ can assume three possible values, zero, infinity, or a positive finite number. More specifically, a plot of $H^S(A)$ against *s* (Figure A.2) shows that there exists a value for *s* above which $H^S(A)$ is zero and below which $H^S(A)$ is infinity. This value of *s* is D_H, and is given by

$$D_H = \inf\{s : H^S(A) = 0\} \qquad (8)$$

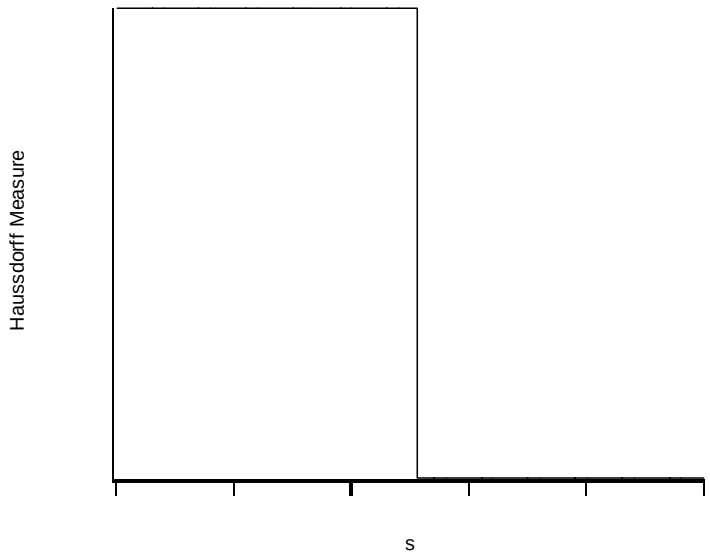

Figure A.2. Graph of $H^s(A)$ vs s. The location at which $H^s(A)$ jumps from infinity to zero is at $s = D_H$.

The fundamental difference between D_H and D_s is subtle. Both involve covering the fractal set **A** with coverings of limited size, and then letting the (maximum) size of the coverings shrink toward zero and observing variations in quantities such as length or number of coverings. Notice in the definition of a δ-cover that the set **A** is covered by balls of radius less than or equal to δ, and the infimum of the sum of the *s*th powers assures that $H^S(A)$ is defined by the best δ-cover. During calculation of D_s, however, coverings are restricted to be equal to ε in size. Coverings of various shape and methods of placement have been used to calculate D_s, and there is current debate as to what method is appropriate.

In the general case, one can always say that

$$0 <= D_{top} <= D_H <= D_s <= D_{emb} \qquad (9)$$

and in certain circumstances we can see that it is possible for D_s to equal D_H. There are several classifications for fractal objects. Two of the most important that we will encounter are self-similar fractals and self-affine fractals. A self-similar fractal is a fractal set **A** that is invariant (excepting a possible translation and rotation) under the ratio *r*. In other words, if one were to 'zoom in' on a small portion of a self-similar fractal image, things would basically look exactly the same. For self-similar fractals, it can be shown [61] that $D_H = D_s$. Self-affine fractals are fractals which are similarly invariant under the ratio vector $\boldsymbol{r} = \{r_1, \ldots, r_n\}$ where *n* is the dimension in which the fractal is embedded. Self-affine fractals, then, differ from self-similar fractals in that the scaling factor is not spatially invariant.

A.2.2 Literature Review

The first study to use fractal concepts to examine turbulent premixed engine flames was Mantzaras *et al*., 1989 [58]. Planar imaging of the reacting flow field was achieved by seeding with TiO_2 and then collecting scattered laser light. The fractal dimension was calculated using the circle method. Around each pixel on the image, a circle of diameter ε is drawn, and each circle that encloses part of the reactant-product interface is 'filled'. The area of filled circles represents a strip of length L and width 2ε, and is a measure of the length of the flame front at a scale of ε. Varying ε and plotting $\log(N_A(\varepsilon))$ against $\log(\varepsilon)$ gives the fractal dimension by

$$N_A(\varepsilon) \propto \varepsilon^{2-D_s} \tag{10}$$

analogous to (5) where N_A represents a normalized area. The turbulent intensity u' was varied by adjusting the operating speed of the engine, and D_s was examined for various cases of u'/S_l at two equivalence ratios, $\phi = 1.0$ and $\phi = 0.59$. The obtained images for these conditions are shown in Figure A.3. It was found that when $\phi = 1.0$, D_s went from 1.12 to 1.37 as u'/S_l increased, where D_s=1.37 was very close to the value measured for the fractal dimension of scalar isosurfaces in nonreacting flows. For the $\phi = 0.59$ case, however, D_s remained essentially constant near 1.35 for all cases of u'/S_l.

More recently, Gulder *et al*. [59] and Smallwood *et al*. [60], were unable to reproduce the variation of the fractal dimension with u'/S_l in turbulent premixed jet flames. They deduced that the difference lied in the method of measuring the fractal dimension. PLIF and MIE scattering images were used to examine flames of various

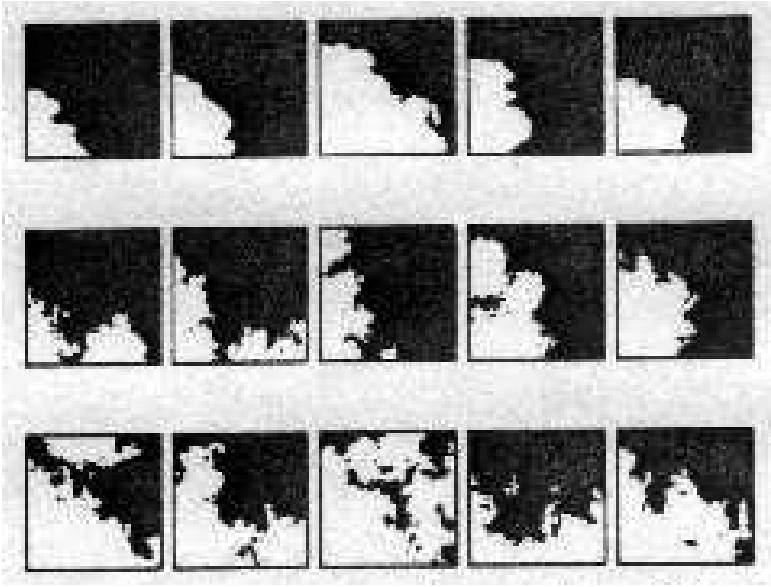

Figure A.3. From Mantzaras, 1989 [58]. Images of engine flames taken at $\Phi = 1.0$, engine speed increases from the top to the bottom of the figure.

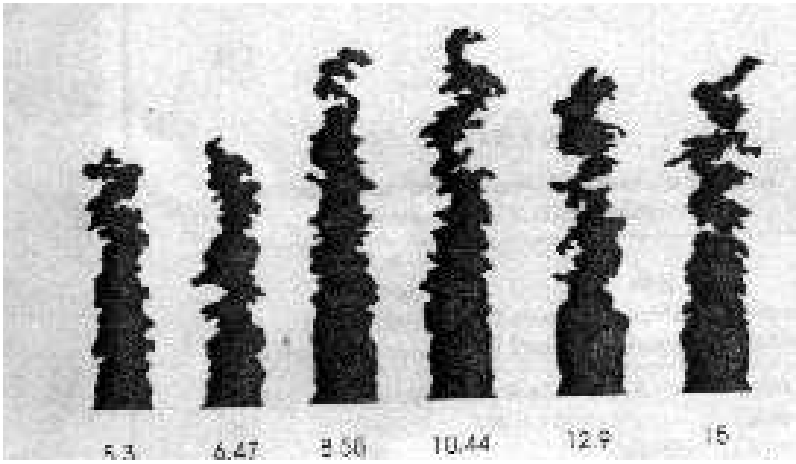

Figure A.4. From Gulder, 2000 [59]. Images of turbulent jet flames, the turbulence intensity increases from left to right.

turbulent intensity. The fractal dimension was measured using the caliper method, described as the yardstick method by Mandelbrot [61], and was measured around the perimeter of the entire flame as shown in Figure A.4. Flame parts separated from the main body were not included in the calculation of D. The yardstick method is analogous to our conceptual example of the walker on the coastline of Norway. Taking a start point on the fractal ($1<D<2$) object, a yardstick of length ε is pinned at one end at the start point and is allowed to pivot around until the other end lands on the object. The process is repeated until the curve is approximated as N yardsticks of length ε placed end to end. Using relation (4) or (5), the fractal dimension D is obtained. They estimated a fractal dimension of approximately 1.2 for all cases studied. In order to identify the discrepancy, they examined the circle method and the caliper method for determining the fractal dimension of several classic self-similar fractals known as Quadric Koch Curves (QKC) for which the fractal dimensions $D_s = D_H$ are known exactly. Their results for the 18-segment ($D_H = D_s = 1.613$, $1 - D \approx -0.61$) QKC and for the 8-segment ($D_H = D_s = 1.5$, $1 - D = -0.5$) QKC are shown in Figure A.5. They used the differences to illustrate the lack of robustness of the circle method and claim that D does not vary with u'/S_l.

A.3 Fractal analysis

A.3.1 Validation of the method of calculating D

The purpose of this subsection is to evaluate the arguments of [59] with respect to [58]. Mandelbrot [61] describes three apparently equivalent methods of calculating the fractal dimension D. Two of these are the circle method and the caliper method already

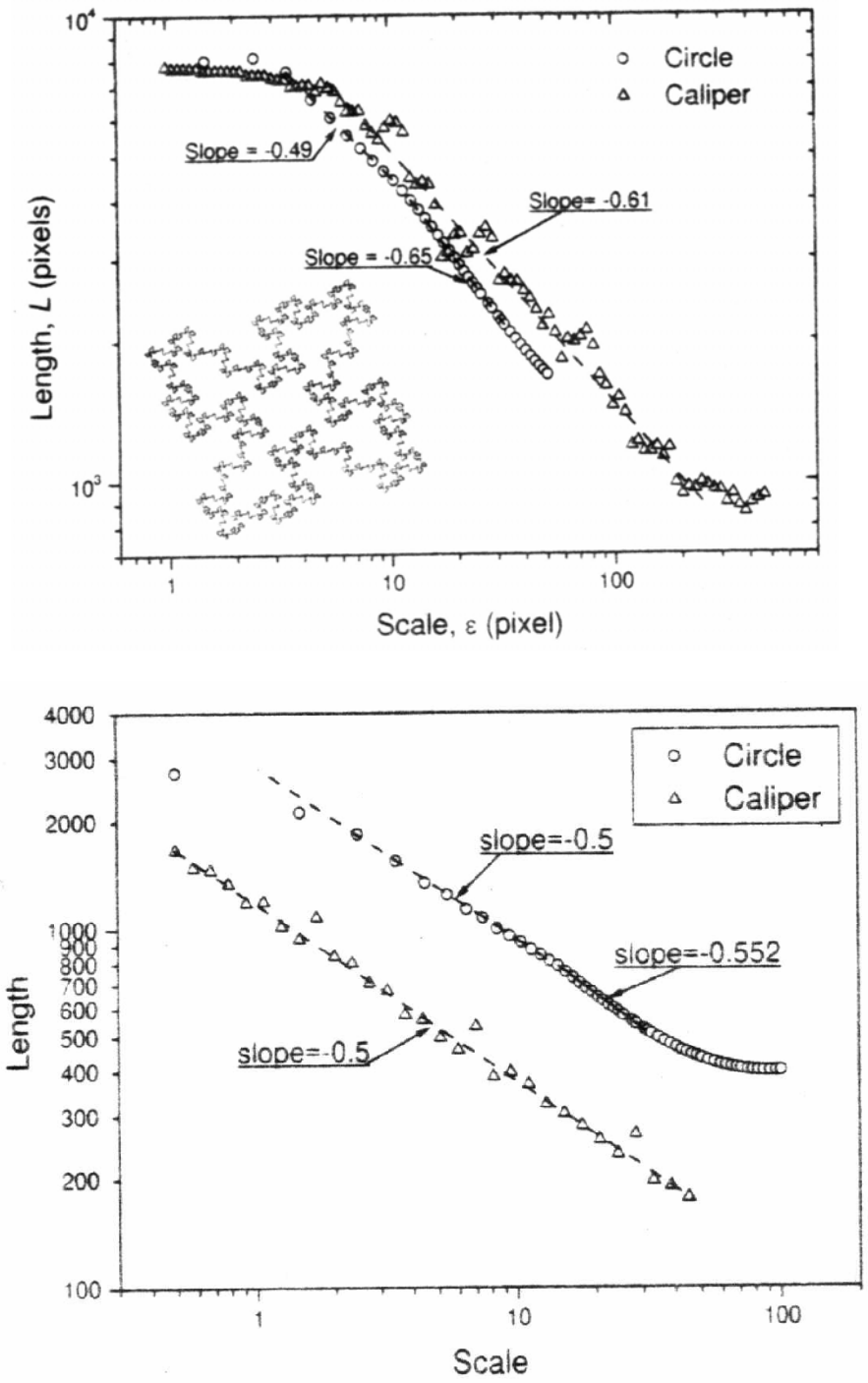

Figure A.5. The results of Gulder et al. showing the calculated fractal dimension of objects of known properties using the circle method and the caliper (yardstick) method. The predicted fractal dimension of the slope of the log(length) vs log(scale) plot is $m = 1 - D_s$. (top) The 18 segment Quadric Koch Curve with $D_s = 1.613$, (bottom) The 8 segment QKC (shown in Figure A.6) with $D_s = 1.5$.

described. The third method is often called the box-counting method. It involves covering a fractal object with a grid of spacing ε, and the number N of grid sites that intersect the object are counted for varying ε. The slope of the log-log plot gives the fractal dimension. Mandelbrot [61] does not indicate whether these methods yield D_s or D_H. Barnsley, 1988 [62] has shown that the box-counting and the circle methods are equivalent and give D_s. No rigorous proof has been found which shows the caliper method is equivalent to the others in calculating D_s. It is maintained here that since the caliper method uses yardsticks of length equal to ε, and since the optimum covering at each ε cannot be assured, that the caliper method calculates D_s.

Gulder *et al*. [59] state that D_H is the appropriate dimension for characterizing length-, area-, and volume-related measurements of fractal objects. References cited therein to support this include Mandelbrot, 1977 [63] and Falconer, 1997 [64]. Mandelbrot ([61], page362) notes in his later work in reference to his definition of the fractal dimension using D_H " . . . I set the border in such a way as to achieve a short definition. If and when a good reason arises, this definition ought to be changed." Mandelbrot [61] also cites instances where D_s is a more appropriate measure than D_H. The comments of Falconer [64] do support D_H as the appropriate dimension, but D_s is described as a useful and well-defined tool. The primary difficulty with D_s is that it lacks certain mathematical properties that restrict its validity. D_s it not appropriate for characterizing open sets and countable sets. Although this may be significant from a purely mathematical standpoint, D_s is an appropriate measure for the fractal objects considered here.

Gulder *et al*. [59] also mention that the caliper technique is the most appropriate method for estimating D_H of self-affine fractals. We have already shown that the caliper method cannot calculate D_H since the coverings are all of the same size ε. We must then interpret these words to mean that the caliper method is the most reliable means of calculating D_s, which therefore provides the best estimate of D_H. It is not contended that the caliper method may provide a clearer estimate of D_s than the circle method, or that the caliper method may in fact be a lower bound to D_s and the circle method an upper bound. Given a sufficient length over which to observe scaling behavior, however, both methods should converge to the same value. The circle method may only be suitable when ensemble averaging over many realizations, in order to smooth out the linear region of the log-log plot, is possible.

Gulder *et al*. [59] then make the following, stronger comment: "These observations indicate that the caliper technique is the appropriate method, and thus that the correct fractal dimension, i.e. Hausdorff-Besicovitch dimension, of the flame front surfaces in the wrinkled flamelet regime is that reported here, about 2.2". The value of $D_H = 2.2$ refers to the surface of the flame, and is obtained by adding one to the value of D_2 determined from the slope of the linear segment of the log-log plot. This is common in the literature though only strictly valid for self-similar fractals. Having addressed the validity of D_s, and shown that the caliper method calculates D_s, the implied claim that the increasing value of D_s with u'/S_l reported by Mantzaras *et al*. [58] is an artifact of the measurement technique will be evaluated.

The differences between the circle method and caliper method as exhibited in Figure A.5 will be described briefly. It is known that differing methods of calculating D_s (as well as different algorithms) can give varying results, and this is taken to be the reason that Shepherd *et al*. [57] recommend ensemble averaging of the results. The self-similar fractals do not allow for any type of ensemble averaging for the circle method, while the caliper method is averaged over many different start positions. Box and circle counting methods often result in sinusoidal-type waves in the scaling part of the log-log plot, while the caliper method often shows a repeated hook like pattern (especially for self-similar fractals). Referring to Figure A.5 of [59], the 'hook' can be seen in the plots of the caliper method, and it is suggested that the multiple slopes pointed out for the circle method result from looking at restricted parts of the data.

Referring to Figure A.3 of [58] for $\Phi = 1.0$, it is clear from a visual inspection alone that D_s in increasing with the engine speed (and therefore u'/S_l). Although the fractal dimension is not synonymous with roughness, it can be seen in moving from the top row to the bottom that the flame front develops structures of increasing size at all length scales. There can be little doubt that even the caliper method would show a marked increase in D_s given these images. Along the same lines, note the character of the flames in Figure A.4 of [59]. There is in fact no clear visual indication that D_s is increasing with turbulent intensity, just as they report. It is noted that the inclusion of the base of the flame, where the front appears flat, may result in low values for D_s, and that the caliper method employed did not consider portions of the flame disconnected from

the main structure, which also reduces D_s. These differences alone would lead to a systematically low value but does not explain the observed discrepancies.

Based upon the preceding discussion, it is therefore suggested that the differences in the two studies do not result from the measurement method alone, and that possible physical explanations based upon differing flow field conditions between the engine flame and the burner flame be examined.

An alternative method of calculating D_s is common in percolation theory and lattice models. The digitized images that we investigate are essentially lattices. Take each pixel of the image as being a cover of size εpix, and take L_{max} to be the size of the image (lattice) in units of ε_{pix}. If a pixel on the fractal object is taken as the center of a box side length L, and L is allowed to grow from ε_{pix} (one) to L_{max}, the length of the curve, $S(\varepsilon)$, and the number of enclosed pixels on the object, $N(\varepsilon)$, scale as

$$N(\varepsilon) \propto L^{D} \tag{11}$$

$$S(\varepsilon) \propto L^{D-1} \tag{12}$$

analogous to (4) and (5), except L replaces $1/\varepsilon$. This replacement is justified here heuristically by noting $L = L'/\varepsilon_{pix}$, where L' is the length (physical units, Euclidian) of the region of measurement. Then if we take L' constant and let ε_{pix} shrink we obtain relations (4) and (5), and if we take ε_{pix} = const. and let L' grow we obtain (11) and (12).

The fractal dimension, D_s, can be calculated by choosing a point on the object and letting a box grow about it. The slope of the log-log plot of N against L gives D_s. A distinct advantage of this method is that it allows for extensive averaging over many

points on the fractal. This allows one to smooth the linear region of the log-log plot and more confidently ascertain D_s.

We have tested this method on several familiar self-similar fractals to validate its robustness. The first test fractal is the 8-segment Quadric Koch Curve (QKC) shown in Figure A.6, which has known fractal dimension $D_H = D_s = 1.5$. Figure A.6 also shows the results obtained from the described method, the line of slope 1.5 offset from the data is meant as a guide for the eye. The least squares fit to the data was within 1% in this case and is generally within 3% after only little averaging. The second study fractal is a variant of the QKC with known dimension $D_H = D_s = 1.465$, and is shown in Figure A.7, along with the obtained results. Again, the slope is to within 3% of the correct value after little averaging, and continued averaging leads to improved results (within 1% for d=140, where d refers to the side length of a box centered on the object within which the averaging is done).

It is interesting to note that as the number of points taken into the ensemble average increases, this method of calculating D_s becomes equivalent to a method described by Lenormand and Zarcone, 1985 [65]. This method is common in the physics of disordered media and involves the density-density correlation function $C(r)$

$$C(r) = \sum_{r'} \rho(r')\rho(r'+r) \tag{13}$$

where $\rho(r) = 1$ for an occupied pixel (i.e. a pixel on the fractal object) and $\rho(r) = 0$ otherwise. For a very large object, $C(r)$ is regarded as an accurate method for calculating D_s. For smaller lattice objects as observed here it is helpful to continue the analysis of [65] and define

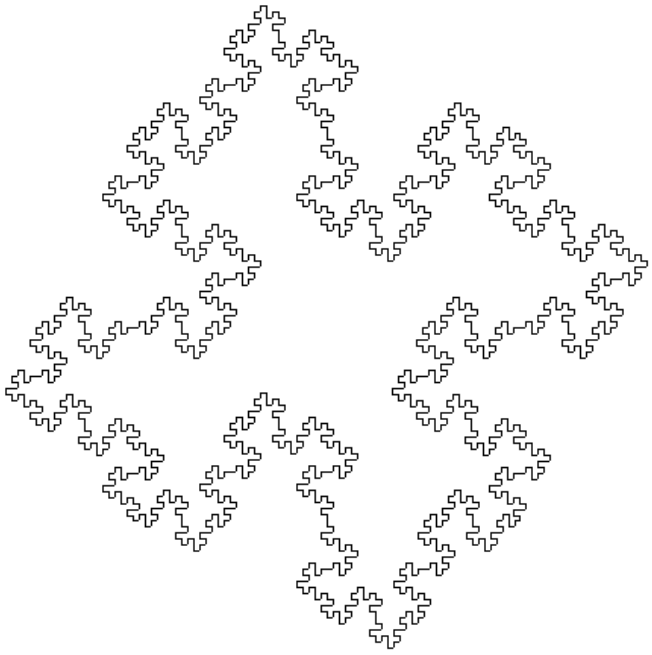

Figure A.6a 8-segment Quadric Koch Curve, which has known fractal dimension $D_s = D_H = 1.5$.

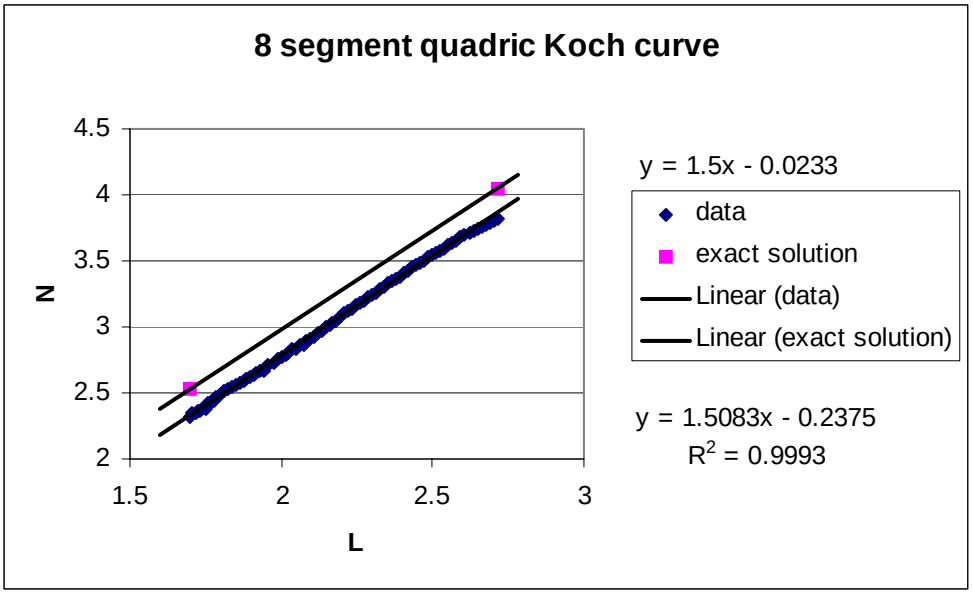

Figure A.6b. Results for the calculated fractal dimension Ds using the box method. The upper line is the exact solution with a slope of 1.5, the lower line is a best fit to the data.

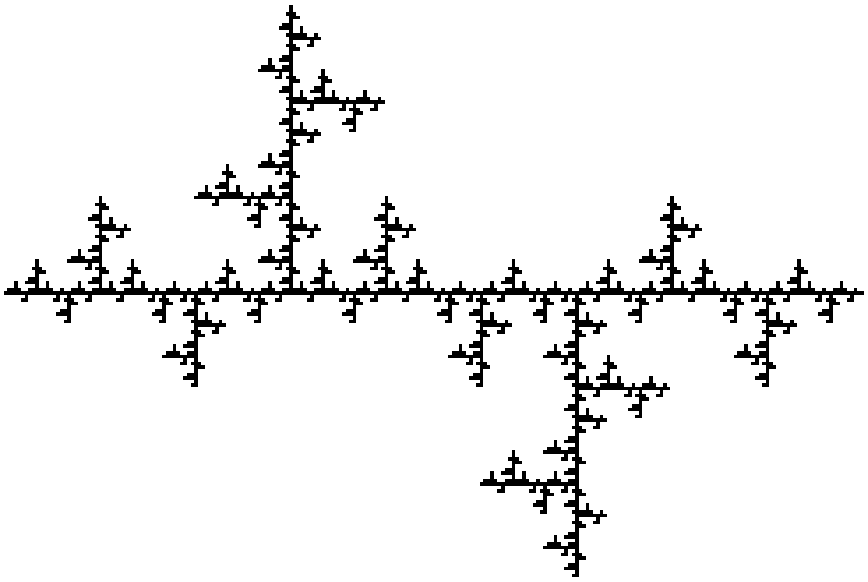

Figure A.7a. Variation of the Quadric Koch Curve having known fractal dimension $D_s = D_H = 1.465$.

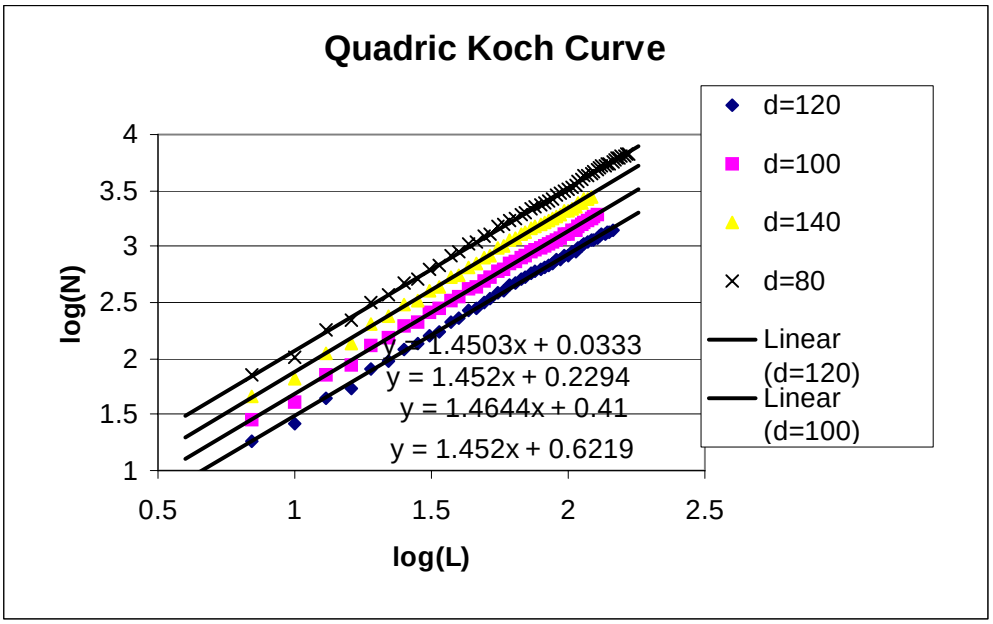

Figure A.7b. Results of the calculation of the fractal dimension Ds using various window sizes on the flame front. An increased widow size increases the number of start points on each image, and therefore results in a larger averaging population.

$$N(R) = \frac{1}{b}\sum_{i=1}^{b}\int_{0}^{R}\rho(i)\rho(r)d^{2}r \qquad (14)$$

which is equivalent to the growing box method described when the average is taken over all points on the fractal object.

A.3.2 Flame structure analysis

The box method from the previous section was used to evaluate the fractal dimension D_s of the flame front using PLIF images of OH taken during homogeneous operation. The correction procedure for the data images is shown in Figure A.8. A raw OH image (Figure A.8a) was first modified by setting each pixel intensity above some threshold value to the maximum 65535 and by setting each pixel intensity below the threshold to zero (Figure A.8b). Various threshold values were investigated but the calculation of D_s was insensitive to these changes. The flame surface was then defined as

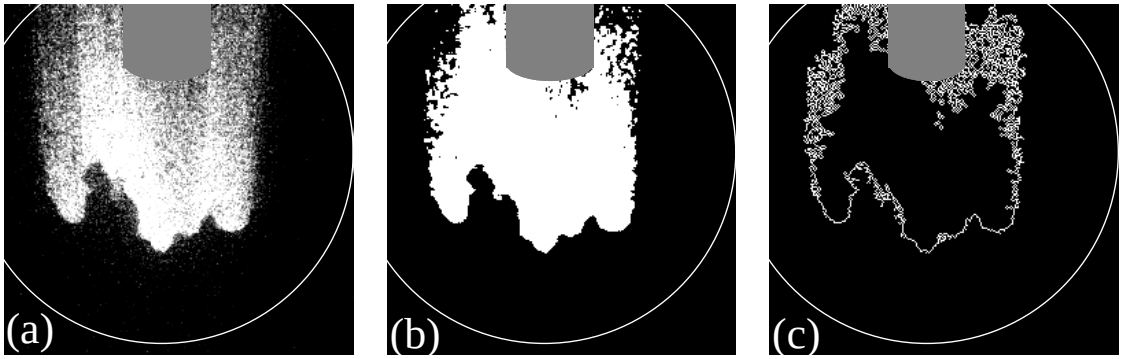

Figure A.8. Demonstration of the OH image processing for the calculation of the fractal dimension. (a) The raw data image, (b) the scaled image, and (c) the outline of the flame front.

all pixels of zero intensity that were neighbored by a pixel of maximum intensity (Figure A.8c). The fractal dimension was then calculated using the box method, averaging over numerous origin points on the flame front (typically 20 to 50 points on each image). The reported fractal dimensions were averaged over about 150 data images. Some images were rejected either because the flame surface was not spatially large enough or in the correct position to employ the calculation method, or because of misfired or poorly burned cycles.

The OH images were obtained under homogeneous operating conditions, using a premixed charge with overall equivalence ratio Φ=0.9. The engine was operated at 600 rpm and 1200 rpm using an ignition time of 20° btdc. Pre-mixed injection was used to ensure a homogeneous mixture so that stratification did not influence the geometry of the flame surface, and any variation in the fractal dimension with engine speed could therefore be attributed to increased turbulence intensity.

Figures A.9 and A.10 show the results for the calculated fractal dimension of the flame front at 600 rpm and 1200 rpm, respectively. At 600 rpm, the calculated (similarity) fractal dimension was D_s = 1.25. At 1200 rpm, the fractal dimension increased to D_s = 1.27. These results are in good agreement with the observations of Mantzaras et al. [58], which demonstrate an increase in D_s from 1.2 to 1.32 as the engine speed (turbulence intensity) increased. Due to speed restrictions in the DISI engine used in this study,however, a wider range of engine speeds and turbulence intensities could not be examined.

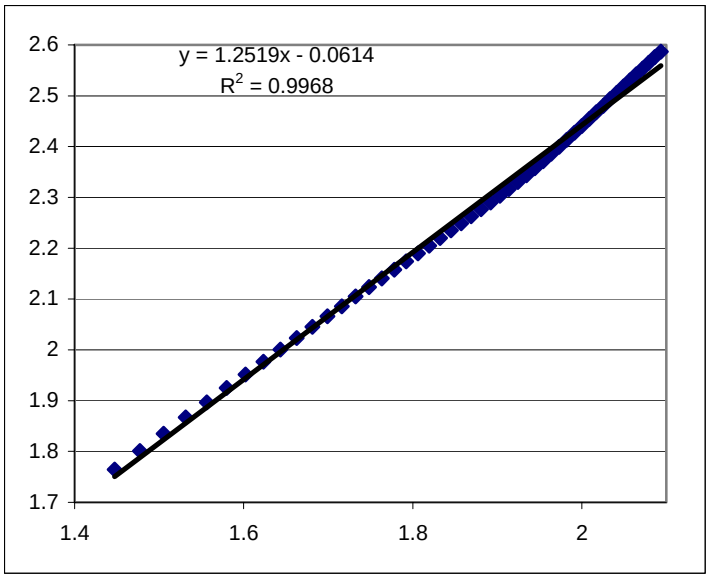

Figure A.9. Calculation of the (similarity) fractal dimension D_s for a premixed engine flame operating at 600 rpm. The result of the log-log plot shows a value of $D_s = 1.25$.

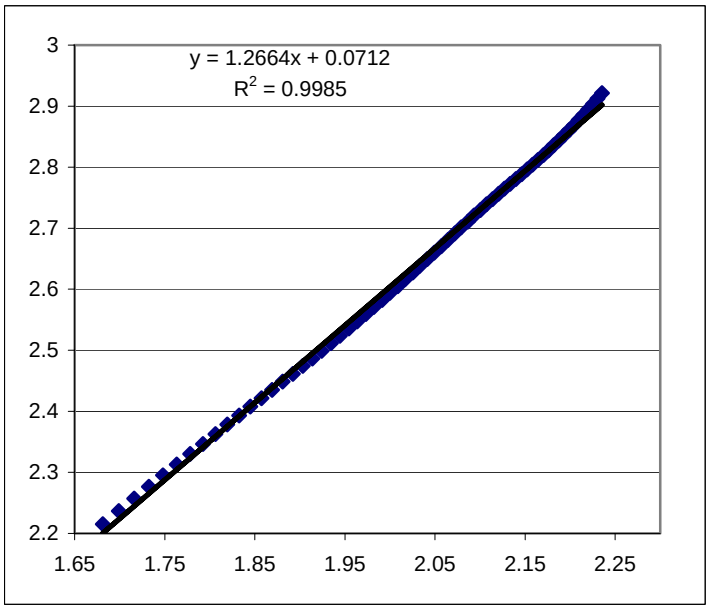

Figure A.10. Calculation of the (similarity) fractal dimension D_s for a premixed engine flame operating at 1200 rpm. The result of the log-log plot shows a value of $D_s = 1.27$.

A.4 Conclusions

This appendix has investigated the application of fractal concepts to examine the geometry of the premixed flame front in an engine. Following a description of some of the fundamentals of fractal analysis, a review of a recent debate in the combustion science literature was presented. It was concluded that the comments of Gulder et al. [59], with regards to the observations of [58], were not justified. The use of a turbulent premixed jet [59], i.e. a reacting shear layer, was not appropriate to drawing conclusions about the fractal geometry of an engine flame. A visual examination of the images of [58] (Figure A.3) is sufficient to conclude that D_s increases with engine speed, regardless of the method used to calculate the fractal dimension. Due to speed limitations of the DISI engine used in this study, the full relationship between the fractal dimension and the turbulence intensity could not be assessed. The limited data obtained are in agreement with the increase in D_s from 1.2 to 1.32 with increasing engine speed reported in [58].

References:

1. Zhao, F.Q. Lai, M-C and Harrington, D.L., “A Review of Mixture Preparation and Combustion Control Strategies for Spark-Ignited Direct-Injection Gasoline Engines,” SAE Paper 970627, 1997.

2. Giovanetti, A.J., Ekchian, J.A., Heywood, J.B. and Fort, E.F., “Analysis of Hydrocarbon Emissions Mechanisms in a Direct-Injection Spark-Ignition Engine,” SAE Paper 830587, 1983.

3. Lancaster, D.R., "Diagnostic Investigation of Hydrocarbon Emissions from a Direct Injection Stratified Charge Engine with Early Injection," Paper C397/80, I. Mech. E. Conference on Stratified Charge Automotive Engines, 1980.

4. Ingham, M.C., Myers, P.S. and Uyehara, O.A., "In-Cylinder Sampling of Hydrocarbons in a Texaco L-141 TCP Engine," SAE Paper 820361, 1982.

5. Hudak, E.B. and Ghandhi, J.B., "Time-Resolved Emission Sampling in a Direct-Injection Engine," *SAE Journal of Engines*, Vol. 108, Sec. 3, pp.1960-1972, 1999. Also published as SAE Paper 1999-01-3309.

6. Koltsakis, G. C. and Stamatelos, A. M., “Catalytic automotive exhaust aftertreatment”, *Prog. Energy Combust. Sci.*, 23, pp. 1-39, 1997.

7. Glaspie, C et al., “Application of design and development techniques for direct injection spark-ignition engines”, SAE Paper 1999-01-0506.

8. Ghandhi, J. B. and Felton, P. G., “On the Fluorescent Behavior of Ketones at High Temperatures,” *Experiments in Fluids*, vol. 21, pp. 143-144, 1996.

9. Thurber, M.C., Grisch, F. and Hanson, R.K., “Temperature Imaging with Single- and Dual-Wavelength Acetone Planar Laser-Induced Fluorescence,” *Optics Letters*, **22**(4), pp. 251-253, 1997.

10. Dieke, G. H. and Crosswhite, H. M., “The ultraviolet bands of OH: Fundamental data”, *J. Quant. Spectrosc. Radiat. Transfer*, 2, pp. 97-199, 1961.

11. Quagliori, T.M., Laufer, G., Krauss, R.H. and McDaniel, J.C., “Laser Selection Criteria for OH Fluorescence Measurements in Supersonic Combustion Test Facilities,” *AIAA Journal*, **31**(3), pp. 520-527, 1993.

12. Seitzman, J. M. and Hanson, R. K., “Comparison of excitation techniques for quantitative fluorescence imaging of reacting flows”, *AIAA Journal*, 31(3), pp. 513-519, 1993.

13. Eckbreth, A.C., Laser diagnostics for combustion temperature and species, Gordon and Breach Publishers, 1996.

14. Abraham, J., *et al*., "A Discussion of Turbulent Flame Structure in Premixed Charge Engines," SAE Paper 850345, 1985.
15. Mantzaras, J., "Geometric Properties of Turbulent Premixed Flames: Comparison Between Computed and Measured Quantities", Combus. Sci. and Tech., 86, pp. 135, 1992.

16. Frank, R.M., Heywood, J.B., "The Effect of Fuel Characteristics on Combustion in a Spark-Ignited Direct-Injection Engine", SAE Paper 902063, 1990.

17. Anderson, R.W., *et al*., "Challenges of Stratified Charge Combustion", 1997

18. Frank, R. M., and Heywood, J.B. "The Effect of Piston Temperature on Hydrocarbon Emissions from a Spark Ignited Direct-Injection Engine", SAE Paper 910558, 1991.

19. Balles, E.N., Ekchian, J.A., and Heywood, J.B., "Fuel Injection Characteristics and Combustion Behavior of a Direct-Injection Stratified-Charge Engine", SAE paper 841379, 1985.

20. Casarella, M.V., and Ghandhi, J.B., "Emission Formation Mechanisms in a Two-Stroke Direct-Injection Engine", SAE Paper 982697, 1998.

21. Drake, M.C., French, D.T., and Fansler, T.D., "Advanced Diagnostics for Minimizing Hydrocarbon Emissions from a Direct-Injection Gasoline Engine", *TwentySixth Symposium on Combustion/The Combustion Institute*, 1996.

22. Abata, D., "A Review of the Stratified Charge Engine Concept", .

23. Ghandhi, J.B., and Bracco, F.V., "Fuel Distribution Effects on the Combustion of a Direct-Injection Stratified-Charge Engine", SAE Paper 950460, 1995.

24. Stanglmaier, R.H., Li, J., and Matthews, D., "The Effect of In-Cylinder Wall Wetting Location on the HC Emissions from SI Engines", SAE Paper 1999-01-0502.

25. Wagner, V., Ipp, W., Wensing, M., and Leipertz, A., "Fuel Distribution and Mixture Formation Inside a Direct Injection SI Engine Investigated by 2D Mie and LIEF Techniques", SAE Paper 1999-01-3659.

26. Frank, R.M., and Heywood, J.B., "The Importance of Injection System Characteristics on Hydrocarbon Emissions from a Direct-Injection Stratified-Charge Engine", SAE Paper 900609, 1990?.

27. Fansler, T.D., French, D.T., and Drake, M.C., "Individual-Cycle Measurements of Exhaust-Hydrocarbon Mass form a Direct-Injection Two-Stroke Engine", SAE Paper 980758, 1998.

28. Fujikawa, T., Hattori, Y., Akihama, K., Koike, M., Kobayashi, T., and Matsushita, S., "Quantitative 2-D Fuel Distribution Measurements in a Direct-Injection Gasoline Engine Using Laser-Induced Fluorescence Technique", *The fourth*

international symposium on Diagnostics and Modeling of Combustion in Internal Combustion Engines, 1998.

29. Fansler, T.D., French, D.T., and Drake, M.C., "Fuel Distribution in a Firing Direct-Ignition Spark-Ignition Engine using Laser-Induced Fluorescence Imaging", SAE Paper 950110, 1995.

30. Chan, C. and Daily, J.W., "Measurement of temperature in flames using laser induced fluorescence spectroscopy of OH", *Applied Optics*, **V19**, No12, 1980.

31. Thurber, M.C., *et al*., "Measurements and modeling of acetone laser-induced fluorescence with implications for temperature-imaging diagnostics", *Applied Optics*, **V37**, No21, 1998.

32. Hanson, R.K., Seitzman, J.M., and Paul, P.H., "Planar Laser-Fluorescence Imaging of Combustion Gases", *Applied Physics B* **50**, pp. 441-454, 1990.

33. Azzazy, M., and Daily, J.W., "Fluorescence Measurements of OH in a Turbulent Flame", *AIAA Journal* **V21**, No 8, 1982.

34. Seitzman, J.M., and Hanson, R.K., "Comparison of Excitation Techniques for Quantitative Fluorescence Imaging of Reacting Flows", *AIAA Journal* **V31**, No 3, 1993.

35. Suntz, R., *et al*., "Two-Dimensional Visualization of the Flame Front in an Internal Combustion Engine by Laser-Induced Fluorescence of OH Radicals", *Applied Physics B* **47**, pp. 287-293, 1988.

36. Thurber, M.C., and Hanson, R.K., "Simultaneous imaging of temperature and mole fraction using acetone planar laser-induced fluorescence", *Experiments in Fluids* **30**, pp. 93-101, 2001.

37. Lozano, A. Yip, B, and Hanson, R.K., "Acetone: a tracer for concentration measurements in gaseous flows by planar laser-induced fluorescence", *Experiments in Fluids* **13**, pp. 369-376, 1992.

38. Thurber, M.C., Grisch, F., and Hanson, R.K., "Temperature imaging with single- and dual-wavelength acetone planar laser-induced fluorescence", *Optics Letters* **V22**, No 4, 1997.

39. Yuen, L.S., Peters, J.E., and Lucht, R.P., "Pressure dependence of laser-induced fluorescence from acetone", *Applied Optics* **V36**, No 15, 1997.

40. Kychakoff, G., Howe, R.D., and Hanson, R.K., "Quantitative flow visualization technique for measurements in combustion gases", *Applied Optics* **V23**, No 5, 1984.

41. Quagliaroli, T.M., Laufer, G., Krauss, R.H., and McDaniel Jr., J.C., "Laser Selection Criteria for OH Fluorescence Measurements in Supersonic Combustion Test Facilities", *AIAA Journal* **V31**, No 3, 1993.

42. Graskow, B.R., et al., “Exhaust Particulate Emissions from a Direct Injection Spark Ignition Engine”, SAE Paper 1999-01-1145.

43. Kakuhou, A., et al., “Characteristics of Mixture Formation in a Direct Injection SI Engine with Optimized In-cylinder Swirl Air Motion”, SAE Paper 1999-01-0505.

44. Spiegel, L, and Spicher, U., “Mixture Formation and Combustion in a Spark-Ignition Engine with Direct Fuel Injection”, SAE Paper 920521, 19??.

45. Tomoda, T., et al., “Development of Direct Injection Gasoline Engine - Study of Stratified Mixture Formation”, SAE Paper 970539, 19??.

46. Anderson, R.W., et al., “Understanding the Thermodynamics of Direct Injection Spark-Ignition (DISI) Combustion Systems: An Analytical and Experimental Investigation”, SAE Paper 962018, 19??.

47. Ghandhi, J.B. and Bracco, F.V., “Mixture Preparation Effects on Ignition and Combustion in a Direct-Injection Spark-Ignition Engine”, SAE Paper 962013, 1996.

48. Cathcart, G. and Zavier, C., “Fundamental Characteristics of an Air-Assisted Direct Injection Combustion System as Applied to 4 Stroke Automotive Gasoline Engines”, SAE Paper 2000-01-0256.

49. Arnold, A., *et al*., “Simultaneous Imaging of Fuel and Hydroxyl Radicals in an In-Line Four Cylinder SI Engine”, SAE Paper 932696, 1993.

50. Tabata, M., *et al*., “Measurement of Fuel Distribution in the Piston Cavity of Direct Injection SI Engine by Using LIF”, SAE Paper 2000-01-0240.

51. Lancaster, D.R., Krieger, R.B., and Lieneach, J.H., “Measurement and Analysis of Engine Pressure Data”, SAE Paper 750026, 1975.

52. Paul, P.H., *et al*., “High resolution digital flowfield imaging of jets”, *Experiments in Fluids* **9**, pp. 241-251, 1990.

53. Ellenberger, U., Glinz, A. and Balmer, J.E., “A comparative study of the gain characteristics of image intensifiers”, 1993.

54. Janesick, J.R., *et al*., “Scientific charge-coupled devices”, *Optical Engineering* **V26** No. 8, 1987.

55. Sandel, B.R. and Broadfoot, A.L., “Statistical performance of the intensified charge-coupled device”, *Applied Optics* **V25** No. 22, 1986.

56. Gouldin, F.C., “An Application of Fractals to Modeling Premixed Turbulent Flames”, *Combustion and Flame* **68**, pp. 249-266, 1987.

57. Shepherd, I.G., Cheng, R.K., and Talbot, L., “Experimental criteria for the determination of fractal parameters of premixed turbulent flames”, *Experiments in Fluids* **13**, pp. 386-392, 1992.

58. Mantzaras, J., Felton, P.G., and Bracco, F.V., “Fractals and Turbulent Premixed Engine Flames”, *Combustion and Flame* **77**, pp. 295-310, 1989.

59. Gulder, O.L., *et al*., “Flame Front Surface Characteristics in Turbulent Premixed Propane/Air Combustion”, *Combustion and Flame* **120**, pp. 407-416, 2000.

60. Smallwood, G.J., *et al*., “Characterization of Flame Front Surfaces in Turbulent Premixed Methane/Air Combustion”, *Combustion and Flame* **101**, pp. 461-470, 1995.

61. Mandelbrot, B., The Fractal Geometry of Nature, publisher W.H. Freeman, San Francisco, 1982

62. Barnsley, M., Fractals Everywhere, publisher Academic Press, Inc., 1988.

63. Mandelbrot, 1977.

64. Falconer, K., Fractal Geometry: Mathematical Foundations and Applications, publisher John Wiley & Sons, Ltd., 1997.

65. Lenormand, R. & Zarcone, C., Capillary Fingering: Percolation and Fractal Dimension. *Transport in Porous Media* 4: 599-612, 1989.